UNIVERSIDADE DE SÃO PAULO
Instituto de Ciências Matemáticas e de Computação

Mean-field reduction in sparse networks

Hans Muller Junho de Mendonça

Tese de Doutorado do Programa de Pós-Graduação em Ciências de Computação e Matemática Computacional (PPG-CCMC)

ICMC USP SÃO CARLOS

Hans Muller Junho de Mendonça

Mean-field reduction in sparse networks

Doctoral dissertation submitted to the Instituto de Ciências Matemáticas e de Computação – ICMC-USP, in partial fulfillment of the requirements for the degree of the Doctorate Program in Computer Science and Computational Mathematics. *FINAL VERSION*

Concentration Area: Computer Science and Computational Mathematics

Advisor: Prof. Dr. Tiago Pereira da Silva

USP – São Carlos
November 2023

Ficha catalográfica elaborada pela Biblioteca Prof. Achille Bassi
e Seção Técnica de Informática, ICMC/USP,
com os dados inseridos pelo(a) autor(a)

M249m

Mendonça, Hans Muller Junho de
Mean-field reduction in sparse networks / Hans Muller Junho de Mendonça; orientador Tiago Pereira da Silva. -- São Carlos, 2023.
100 p.

Tese (Doutorado - Programa de Pós-Graduação em Ciências de Computação e Matemática Computacional) -- Instituto de Ciências Matemáticas e de Computação, Universidade de São Paulo, 2023.

1. sincronização. 2. redes densas. 3. redes esparsas. I. Silva, Tiago Pereira da, orient. II. Título.

Bibliotecários responsáveis pela estrutura de catalogação da publicação de acordo com a AACR2:
Gláucia Maria Saia Cristianini - CRB - 8/4938
Juliana de Souza Moraes - CRB - 8/6176

Hans Muller Junho de Mendonça

Redução de campo médio em redes esparsas

Tese apresentada ao Instituto de Ciências Matemáticas e de Computação – ICMC-USP, como parte dos requisitos para obtenção do título de Doutor em Ciências – Ciências de Computação e Matemática Computacional. *VERSÃO REVISADA*

Área de Concentração: Ciências de Computação e Matemática Computacional

Orientador: Prof. Dr. Tiago Pereira da Silva

USP – São Carlos
Novembro de 2023

RESUMO

MENDONCA, H. M. J. DE. **Redução de campo médio em redes esparsas**. 2023. 100 p. Tese (Doutorado em Ciências – Ciências de Computação e Matemática Computacional) – Instituto de Ciências Matemáticas e de Computação, Universidade de São Paulo, São Carlos – SP, 2023.

A sincronização é um fenômeno observado em diversos campos científicos, que vão desde sistemas mecânicos e biológicos até comportamentos sociais. O modelo de Kuramoto, desenvolvido nas décadas de 1970 e 1980, revolucionou a compreensão da sincronização espontânea em grandes sistemas de elementos interagentes. Nesse modelo, a sincronização é quantificada utilizando o parâmetro de ordem, que representa o centroide de pontos distribuídos na circunferência unitária. O modelo de Kuramoto revelou a existência de três estados distintos: assíncrono, parcialmente síncrono e completamente síncrono. Enquanto o modelo clássico de Kuramoto assume uma configuração de rede de todos para todos, a maioria das redes do mundo real são esparsas. Compreender a sincronização em redes esparsas e os efeitos do tamanho finito do sistema na sincronização é um problema de pesquisa desafiador.

Para abordar esse problema, adotamos uma estrutura de sistema dinâmico usando mapas de Möbius na circunferência unitária complexa. Investigamos a transição para a sincronização em redes complexas densas e esparsas, onde os sistemas evoluem por meio de mapas em vez de equações diferenciais ordinárias. Exploramos os efeitos do tamanho finito do sistema nos fenômenos de sincronização e examinamos o comportamento de escala do tempo médio para a sincronização. Surpreendentemente, descobrimos que o estado incoerente pode ser metaestável para determinados valores de acoplamento e densidades de links, desafiando suposições convencionais. Ao analisar as equações de campo médio, construímos um diagrama de bifurcação para redes infinitamente grandes e observamos a presença de transientes caóticos com tempos de escape distribuídos exponencialmente. Isso sugere que o sistema passa por períodos transitórios de assincronia antes de atingir um estado sincronizado. Nossa pesquisa proporciona uma compreensão abrangente da sincronização em redes complexas, lançando luz sobre o comportamento de sistemas do mundo real. Ela contribui com percepções valiosas sobre a dinâmica de redes de tamanho finito e desafia suposições existentes. Nossas descobertas têm implicações para a dinâmica de redes e aprimoram nossa compreensão dos fenômenos de sincronização em diversos sistemas.

Palavras-chave: sincronização, redes densas, redes esparsas.

ABSTRACT

MENDONCA, H. M. J. DE. **Mean-field reduction in sparse networks**. 2023. 100 p. Tese (Doutorado em Ciências – Ciências de Computação e Matemática Computacional) – Instituto de Ciências Matemáticas e de Computação, Universidade de São Paulo, São Carlos – SP, 2023.

Synchronization is a phenomenon observed in various scientific fields, ranging from mechanical and biological systems to social behavior. The Kuramoto model, developed in the 1970s and 1980s, revolutionized the understanding of spontaneous synchronization in large systems of interacting elements. In this model, synchronization is quantified using the order parameter, which represents the centroid of points distributed on the unit circle. The Kuramoto model revealed the existence of three distinct states: asynchronous, partially synchronous, and completely synchronous. While the classic Kuramoto model assumes an all-to-all network configuration, most real-world networks are sparse. Understanding synchronization in sparse networks and the effects of finite system sizes on synchronization is a challenging research problem.

To address this problem, we adopt a dynamical system framework using Moebius maps on the complex unit circle. We investigate the transition to synchronization in both dense and sparse complex networks, where systems evolve through maps instead of ordinary differential equations. We explore the effects of finite system sizes on synchronization phenomena and examine the scaling behavior of the mean time to synchronization. Surprisingly, we discover that the incoherent state can be meta-stable for certain coupling strengths and link densities, challenging conventional assumptions.

By analyzing mean-field equations, we construct a bifurcation diagram for infinitely large networks and observe the presence of chaotic transients with exponentially distributed escape times. This suggests that the system experiences transient periods of asynchrony before reaching a synchronized state. Our research provides a comprehensive understanding of synchronization in complex networks, shedding light on the behavior of real-world systems. It contributes valuable insights into the dynamics of finite-sized networks and challenges existing assumptions. Our findings have implications for network dynamics and enhance our understanding of synchronization phenomena in diverse systems.

Keywords: synchronization, dense networks, sparse networks.

LIST OF FIGURES

Figure 1 – Illustration of the observable r. In part (A), they are uniformly spread the circle with $r \approx 0$. In part (B), we have that all elements are moving on together, implying that $r \approx 1$ 18

Figure 2 – Transition in the globally coupled Kuramoto model. Note that for $\varepsilon < \varepsilon_c$ the value of the $r_\infty \approx 0$, implying that the system is not synchronized. Considering $\varepsilon > \varepsilon_c$, we have block (II), where the system is partially synchronized, and block (III), where the system is completely synchronized. 18

Figure 3 – The straight line represents the periodic phase θ. It parameterizes the motion of the point along the γ. The initial phase θ_0 (shown by a blue circle) can be chosen arbitrarily. 26

Figure 4 – Isochrons I_{x_0} and I_x inside the basin of attraction. The isochrons foliate the whole basin of attraction and the flow sends point on isochrons into isochrons. All the points on the same isochron have identical asymptotic phase values. . 28

Figure 5 – Illustration of the isochrons (dashed lines) of the system (2.46). Points on the same isochron have identical asymptotic phase values, e. g., B and C. The point B outside the limit cycle γ has asymptotic value (equals to C) greater than A, even A and B sharing the same θ value between the x-axis and the dashed yellow curve. 29

Figure 6 – Adapted from (ELDERING, 2013) where we show the transversal directions to the normally hyperbolic invariant manifold M, where the double arrows indicate a convergence rate greater than the single ones. 30

Figure 7 – (a) directed graph and its respective adjacency matrix A, and (b) a undirected graph. 34

Figure 8 – (a) the all-to-all graph, where all the nodes have the same degree, and (b) the star graph, where the node 9 has the highest degree in comparison with the other ones. 35

Figure 9 – Representation of the distance between two nodes in a graph. From this, we can conclude by eq. (3.9) that $L_{i,j} = 2$. 36

Figure 10 – Different topologies of the Edös-Rényi model with fixed nodes $N = 20$ and considering different values of p. 37

Figure 11 – The blue dots is the Edös-Rényi model considering an average of 100 realizations of $N = 1000$ nodes and probability $p = 0.05$. The dashed line is the expected distribution given by eq. (3.12) 38

Figure 12 – Barabási–Albert model considering $N = 20$ nodes. 39
Figure 13 – The blue dots is the Barabási–Albert model considering the complex network with $N = 1000$ nodes. The red dashed line is the expected distribution given by eq. (3.13). 39
Figure 14 – Different topologies of the Watts–Strogatz model with $N = 20$ fixed nodes, $k = 4$, and considering different values of p. 40
Figure 15 – $N = 500$, $k = 4$, $p = 0$ to 1 41
Figure 16 – (a) exhibits the growth of $|E|$ as function of N for the Newman-Watts-Strogatz model (NEWMAN; WATTS, 1999). The black circles are the simulation result, and the red dashed line is the linear fit with the coefficients $a \approx 1.1$ and $b \approx 0.18$. (b) is similar to (a), but represents the growth of a complete graph where the red dashed line is the quadratic fit with coefficients $a \approx 0.5$, $b \approx -0.5$, and $c \approx 0$. 42
Figure 17 – The order parameter behavior as a function of time where we consider two distinct situations during the simulations of the model eq. (4.2) and eq. (4.8). In both, we consider $N = 1000$ oscillators, and the ω_i are normally distributed. We take K different values as labeled in the figure. The blue line shows that the system after some time synchronizes ($r \approx 1$), however the red one, the system stays on an incoherence regime ($r \approx 0$) without synchronizing. . . . 45
Figure 18 – Bifurcation diagram of the Kuramoto model, considering the normal distribution with $N = 5000$ 46
Figure 19 – Global transition for the phase model eq. (6.8), considering the asymptotic behavior of the order parameter eq. (6.9). For this simulation, we consider $N = 800$ interacting units uniformly distributed between 0 to 2π, $\sigma = 1$ and after $n = 10^4$ iterations, we took the ϑ_i for $i = 1, \ldots, N$ to compute one of the 50 values of r_∞. Note that for $\alpha < \alpha_c$, the value of the $r_\infty \approx 1$, implying that the system is completely synchronized. However, for $\alpha > \alpha_c$, we have a discontinuous transition between the synchronous to asynchronous state. . . 47
Figure 20 – Shows for $k = 1$ and $k = 2$ the realizations of the stochastic process given by eq. (5.13). 54
Figure 21 – Shows some sample functions for $\omega_1 = 1$, $\omega_2 = 2$, $\omega_3 = 3$, and $\omega_4 = 4$ for all $t \in [-2\pi, 2\pi]$. 55
Figure 22 – (a) shows the stochastic process given by eq. (5.17) for some fixed values of t, and (b) shows the same stochastic process, but following eq. (5.18) for some fixed values of ω. 56
Figure 23 – (a) shows the eq. (5.34) for $\omega_0 = 1$ as function of time and (b) represents its respective Fourier transform considering just the positive part $\delta(\omega - \omega_0)$ of eq. (5.35) as a function of the natural frequency ω. 59

Figure 24 – (a) shows a sample function of the stochastic process given by eq. (5.13), (b) shows the autocovariance function of the process, where the blue points represent the "ACF white noise" and the red line fitting it is the Dirac delta represented by "$\delta(\tau)$". In (c), we have the power spectrum density, which is constant for this sort of stochastic process. 61

Figure 25 – Complex network structure where the black arrows are the connections of the ring, which has N fixed links and the brown ones are the shortcuts N_{sc}. The topology of the network could be encoded by the adjacency matrix A. . 64

Figure 26 – Histogram for the set $\{\vartheta_i(t)\}_{i=1}^{N}$ of phases in different times together with the cumulative histogram in the right-hand-side. For this simulation we consider $N = 7000$, $\sigma = 200$, and $\alpha = 1.57$. For each time unity labeled in the figure, we plot the histogram of the phases. Note that the cumulative histogram of the phases seems to converge to the uniform cdf represented by the dashed black line. 66

Figure 27 – Histogram for the set $\{\eta_i^N(0,t,\alpha')\}_{i=1}^{N}$ with $N = 7000$, $\sigma = 200$, and $\alpha = 1.57$. The phases started uniformly distributed in $(0,2\pi)$ and for different time unities labeled in the figure we compute the fluctuations from **??** 6.17. . 67

Figure 28 – Panel (a) shows a sample function of the process $\{\eta_i(t_j)\}_{j=1}^{n}$ for $i = 500$, in the panel (b) we have the autocovariance function of (a) running overtime τ, the panel (c) is the power spectrum density considering the autocovariance function in (b), and in the last panel (d), we plot the log-log scale of the red curve outlining the extremes of the autocovariance function. For all simulations of this figure, we consider $N = 7000$, $\sigma = 200$, $\alpha = 1.57$, and we take just the last 1000 units of time of the simulation. 68

Figure 29 – Dynamics of phases. $N = 30$ points on the complex unit circle colored by phase, and corresponding mean field (red dot inside the unit circle). From left to right : initial phase configuration at the points z_n with mean-field amplitude $R = 0.5$ and mean-field phase $\Theta = \pi/4$, after chaotic phase doubling z_n^2 with $R^2 = 0.25$ and $2\Theta = \pi/2$, and after subsequent contraction toward the angle $\pi/2$ with intensity $\tau = 0.5$. Figure from: Mendonca, Tönjes and Pereira () . 72

Figure 30 – Bifurcation diagram of the mean-field amplitude and a representation of the network interaction. In (**a**), the bifurcation diagram of the all-to-all coupling mean-field dynamics (7.12), i.e., on the Ott-Antonsen manifold. Dotted lines show linearly unstable fixed points and solid lines show linearly stable fixed points in the thermodynamic limit. (**b**) Venn diagram of a dense network with N vertices and connection probability p. The sets of neighbors of nodes m and n are of size pN and their overlap is of size p^2N, resulting in correlated local mean fields $Q_m = R_m \exp(i\Theta_m)$ and $Q_n = R_n \exp(i\Theta_n)$ acting on the states z_m and z_n. The ratio of the amplitudes of the local mean fields and the global mean field are independent of the network size N. Figure from: Mendonca, Tönjes and Pereira () 74

Figure 31 – Transient to synchronization for $N = 10{,}000$ coupled maps in (**a**,**b**), a fully connected network with coupling strength $\varepsilon = 1.81$ below the critical coupling $\varepsilon_0 = 2$, and (**c**,**d**), in a random network with connection probability $p = 0.1$ for a coupling strength of $\varepsilon = 2.3$ above the critical coupling. The upper panels (**a**,**c**) show the order parameter $R(t)$, and the lower panels (**b**,**d**), the real part of the ratio of the first two circular moments $\mathrm{Re}[Z_1^2/Z_2]$. This serves as a visual measure of the alignment of the system state with the Ott-Antonsen manifold, where the ratio is exactly equal to one. The dashed line in (**a**) marks the value of the unstable fixed point of the mean-field dynamics, $R_u = 0.098$. Above that value, the state of complete synchronization is attractive on the Ott-Antonsen manifold. In (**b**,**d**), the incoherent state $R = 0$ is unstable; however, finite size fluctuations do not grow exponentially. Instead, we observe a long chaotic transient. Figure from: Mendonca, Tönjes and Pereira () 77

Figure 32 – Statistics of transient times t_m to synchronization. (**a**–**c**) In the fully connected network; (**d**–**f**) in random networks of various link densities $p = k/N$. The upper panels show straight lines in semi-logarithmic plots of cumulative tail distributions of the transient times, demonstrating the rate character of the transition process. The middle panels show the estimated average transient times for various combinations of system sizes N, coupling strengths ε, and link densities p. The mean field critical coupling strength $\varepsilon_0 = 2.0$ and the maximum observation time T are marked by dashed lines. In the globally coupled system on the left-hand side, the transient time depends strongly on the system size N, whereas in dense networks and above ε_0, the transient time depends strongly on the link density $p = k/N$, but not on the system size. We demonstrate the scaling of the transition times in the lower panels. In the globally coupled system, the exponential divergence of the transient times below ε_0 appears to be a function of $(\varepsilon - \varepsilon_0)N^{\frac{1}{3}}$. In dense networks, the exponential divergence is roughly a function of $(\varepsilon - \varepsilon_0)p$. Figure from: Mendonca, Tönjes and Pereira () 78

CONTENTS

1 INTRODUCTION . . . 17

2 PHASE MODEL . . . 21
2.1 Initial value problem and flow . . . 21
2.2 Limit cycle and its stability . . . 23
2.2.1 Asymptotic stability of periodic orbits . . . *24*
2.3 Phase oscillators . . . 25
2.4 Perturbed phase system . . . 29

3 COMPLEX NETWORK EXAMPLES . . . 33
3.1 Graphs . . . 33
3.2 Erdös-Rényi model . . . 36
3.3 Barabási–Albert model . . . 38
3.4 Watts–Strogatz model . . . 39
3.5 Sparse networks . . . 41

4 SYNCHRONIZATION TRASITION IN COMPLEX NETWORKS . 43
4.1 Network dynamics . . . 43
4.2 Phase synchronization phenomena . . . 44
4.2.1 All-to-all Kuramoto model synchronization . . . *45*
4.3 Discontinuous transition . . . 46
4.3.1 Phase model . . . *46*

5 STOCHASTIC PROCESS AND SOME FEATURES . . . 49
5.1 Some definitions of probability theory . . . 49
5.2 Stochastic Process and some examples . . . 52
5.3 Autocovariance function, Fourier Transform and Power spectral density 57
5.3.1 Autocovariance function . . . *57*
5.3.2 Fourier transform . . . *58*
5.3.3 Power spectrum density . . . *59*

6 INTERNAL FLUCTUATIONS . . . 63
6.1 Problem description . . . 63
6.1.1 Network . . . *63*

6.1.2 *Phase model* *64*
6.1.3 *Mean-field approach* *65*
6.1.4 *Fluctuation approach* *65*
6.1.5 *Numerical observations about* α *65*
6.1.6 *Autocovariance function of the fluctuations for* $\alpha > \alpha_c$ *67*

7 SYNCHRONIZATION OF COUPLED CHAOTIC CIRCLE MAPS . 69
7.1 Model 69
7.2 Moebius map 70
7.3 Mean-field as Moebius map dynamics 71
7.3.1 *Mean-Field Analysis* *73*
7.4 Extension to Networks 74
7.5 Results and Conclusions 75
7.5.1 *Distributions of Transient Times* *75*
7.5.2 *During Coexistence: Escape over the Unstable Branch* *75*
7.5.3 *Above the Critical Coupling Strength: Long Chaotic Transient* . . . *76*
7.5.4 *Discussion of Finite Size Scaling* *78*
7.5.5 *Conclusions* *80*

BIBLIOGRAPHY 81

APPENDIX A PROOF OF THE THEOREM 2.3.1 85

ANNEX A ARTICLE: EXPONENTIALLY LONG TRANSIENT TIME TO SYNCHRONIZATION OF COUPLED CHAOTIC CIRCLE MAPS IN DENSE RANDOM NETWORKS 89

CHAPTER

1

INTRODUCTION

Synchronization refers to the adjustment of rhythms observed in various fields of science, such as mechanical, biological, physical systems, and social behavior (PIKOVSKY; ROSENBLUM; KURTHS, 2003; STROGATZ, 2003; WINFREE, 2001). One simple example of synchronization is the phenomenon of metronomes shaking side by side and eventually synchronizing their movements[1]. The earliest recorded observation of synchronization dates back to 1665 when the Dutch physicist Christiaan Huygens noticed that two pendulum clocks hanging on the wall swung in harmony, even though there was no apparent reason for it, while he was confined to his bed due to illness(PIKOVSKY; ROSENBLUM; KURTHS, 2003).

In the 1970s and 1980s, the work of Kuramoto had a significant impact on the scientific community, particularly in understanding spontaneous synchronization in systems with a large number of interacting elements (KURAMOTO, 1975; KURAMOTO, 1984). This model, often referred to as the Kuramoto model, provided insights into fundamental aspects of synchronization and led to numerous extensions and new approaches (WINFREE, 2001; STROGATZ, 2000).

Kuramoto quantified the overall synchrony using the order parameter given by

$$re^{i\Phi} = \frac{1}{N}\sum_{j=1}^{N} e^{i\phi_j}, \tag{1.1}$$

where r is the order parameter representing the centroid of N points distributed on the unit circle in the complex plane (see fig. 1).

Kuramoto observed that the behavior of the points changed as they moved around the unit circle. In one extreme, when the elements were not moving together, the value of the order parameter was approximately zero, indicating an asynchronous state (see fig. 1 (A)). In the opposite extreme, when the order parameter was close to one, the system was considered synchronous (fig. 1 (B)). Kuramoto referred to a state with intermediate values of r as partial synchronization.

[1] <https://www.youtube.com/watch?v=W1TMZASCR-I>

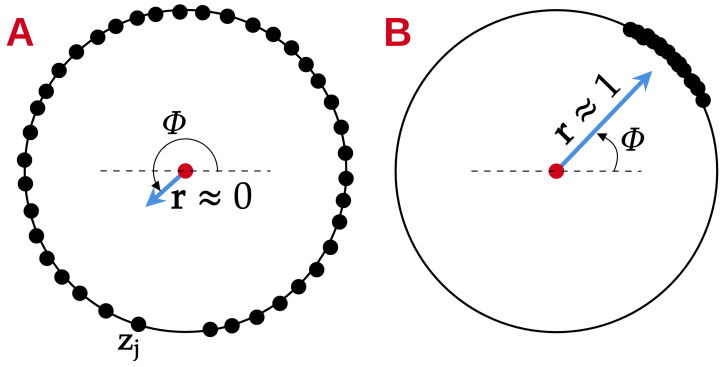

Figure 1 – Illustration of the observable r. In part (A), they are uniformly spread the circle with $r \approx 0$. In part (B), we have that all elements are moving on together, implying that $r \approx 1$

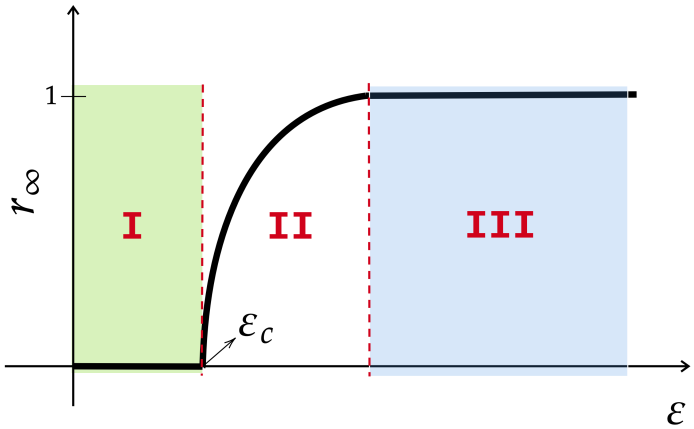

Figure 2 – Transition in the globally coupled Kuramoto model. Note that for $\varepsilon < \varepsilon_c$ the value of the $r_\infty \approx 0$, implying that the system is not synchronized. Considering $\varepsilon > \varepsilon_c$, we have block (II), where the system is partially synchronized, and block (III), where the system is completely synchronized.

In his work (KURAMOTO, 1984), Kuramoto discovered that the system exhibited three different behaviors depending on the values of a parameter ε: asynchronous, partially synchronous, and completely synchronous states (fig. 2, blocks I, II, and III, respectively).

The classic Kuramoto model is based on an all-to-all configuration, where all elements are connected to each other. This configuration can be represented by a fully connected network, which is the densest complex network possible, with a density (d) equal to 1. However, most natural networks are sparse, meaning that $d \ll 1$. The transition to collective behavior in such sparse networks is not well understood, and this motivates our research problem:

– we investigate the transition to synchronization in both dense and sparse complex networks, considering systems that evolve through maps rather than ordinary differential equations. We also aim to explore the effects of finite system sizes on synchronization phenomena.

To address this problem, we adopt a dynamical system framework using Moebius maps as in (GONG; TOENJES; PIKOVSKY,) on the complex unit circle, which act as phase dynamics

in Bernoulli maps

$$\varphi(t+1) = (2\varphi(t) \mod 2\pi). \tag{1.2}$$

The resulting dynamics can be described by

$$z(t+1) = M\left(z(t)^2, \Theta(t), \tau(t)\right) = \frac{e^{2i\Theta}\tau + z^2}{1 + e^{-2i\Theta}\tau z^2}, \tag{1.3}$$

where $z(t)$ represents the state of the system at time t, M denotes the Moebius map, and τ and Θ are parameters within specific ranges: $\tau \in (-1,1)$ and $\Theta \in (0,2\pi]$ respectively.

To summarize our findings, we used mean-field equations to construct a bifurcation diagram for $N \to \infty$. Our analysis revealed several interesting observations. First, we observed the presence of chaotic transients characterized by exponentially distributed escape times. This indicates that the system experiences transient periods of asynchrony behavior before reaching a synchronized state.

Furthermore, we investigated the scaling behavior of the mean time to synchronization. By examining the relationship between system size and the time required for synchronization to occur, we gained valuable insights into the dynamics of finite-sized networks. Surprisingly, we discovered that the incoherent state, where elements are not synchronized, can be meta-stable for coupling strengths exceeding the critical coupling in the mean-field model depending on the link density $p = \frac{\langle k \rangle}{N}$, where $\langle k \rangle$ is the mean node degree size of neighbors and N is the size of the network. This finding challenges conventional assumptions and sheds new light on the behavior of complex networks with finite sizes.

In conclusion, our research provides a comprehensive understanding of synchronization in complex networks. By employing mean-field equations and examining both dense and sparse network configurations, we uncovered the presence of chaotic transients, studied the scaling behavior of synchronization time, and identified the meta-stability of the incoherent state. These results contribute to the broader field of network dynamics and offer valuable insights into the behavior of real-world systems

Next, we present the text structure necessary to get to the problem. In chapter 2, We start studying some background about ordinary differential equations in $\mathbb{R}^n$ for a system with exponentially stable limit cycle denoted by γ. Thus, it allows us to reduce and analyze the behavior of this periodic orbit through a phase θ in $\mathbb{T}$.

Moving on, in chapter 3, we introduce some basics and necessary concepts about graphs. Moreover, from chapter 2 and chapter 3 we define the dynamics in complex networks in chapter 4. We also present some results and simulations using the all-to-all Kuramoto Model. In chapter 5, we present some concepts about probability theory, including stochastic process to help us describe the internal fluctuations.

CHAPTER

2

PHASE MODEL

In this chapter, we give some backgrounds about ordinary differential equations, and we aim to study the asymptotic behavior of periodic solutions for certain initial value problems (I.V.P). Furthermore, we analyze the comportment of the system, considering a perturbation on that.

2.1 Initial value problem and flow

Consider the following initial value problem

$$\begin{cases} \dot{x} &= f(x) \\ x(0) &= x_0 \end{cases} \tag{2.1}$$

where $x \in \mathbb{R}^n$, $f \in C^k(U, \mathbb{R}^n)$[1], $k \geq 1$, and U is an open subset of $\mathbb{R}^n$. Since f is a function of class C^k, using the Picard-Lindelöf theorem (see Theorem 2.2 in (TESCHL, 2012), p. 38), the eq. (2.1) has a unique local solution

$$u : J \to U \tag{2.2}$$

with $u \in C^k$ such that $u(0) = x_0$, and $J \subset \mathbb{R}$ is the interval where the solution is defined for $0 \in J$.

Remark. For the reason that the vector field in eq. (2.1) is time independent, we could ask for the solution starting at $x(t_0) = x_0$. By adjusting the domain J in such way that for a fixed t_0, $t \mapsto t + t_0$. Thus, we can define $v(t) = u(t + t_0)$ for t and t_0 in this new time-shifted domain.

Since eq. (2.1) has a unique solution at every point x defined on the time interval J_x, we introduce the set

$$M := \bigcup_{x \in U} J_x \times \{x\} \subset \big(\mathbb{R} \times U\big) \tag{2.3}$$

and we define the map

$$\mathscr{T} : M \to U \tag{2.4}$$

[1] $C^k(U, \mathbb{R}^n)$ denotes the set of functions $U \to \mathbb{R}^n$ having continuous derivatives up to order k.

such that

$$(t,x) \mapsto \mathscr{T}(t,x) \tag{2.5}$$

is called local flow of the differential equation. For the sake of simplicity, we sometimes can write $\mathscr{T}_t(x) \coloneqq \mathscr{T}(t,x)$.

The set

$$\Gamma_{x_0} = \{\mathscr{T}(t,x_0) : t \in J_{x_0}\} \tag{2.6}$$

is the orbit through $x_0 \in U$. Note that

$$\begin{aligned} u(t) &= \mathscr{T}(t,x_0), \quad \text{such that,} \\ u(0) &= \mathscr{T}(0,x_0), \end{aligned} \tag{2.7}$$

for 0 and all $t \in J_{x_0}$ and $x_0 \in U$. If $t+s \in J_{x_0}$ then $u(t+s)$ is also a solution at $y = u(s)$ and in particular $J_{x_0} = s + J_y$. Then, as consequence we note that for $x \in U$ and $s \in J_{x_0}$ we have

$$\mathscr{T}(t+s,x_0) = \mathscr{T}(t,\mathscr{T}(s,x_0)) \tag{2.8}$$

for all $t \in J_{\mathscr{T}(s,x_0)}$. Thus, the flow satisfies two properties on Γ_{x_0}

(a_1) $\mathscr{T}(0,x_0) = x_0$,

(a_2) $\mathscr{T}(t+s,x_0) = \mathscr{T}(t,\mathscr{T}(s,x_0))$, for all $x_0 \in U$ and $t,s \in J_x$.

The condition $(a1)$ implies that

$$\mathscr{T}(0,x) = x, \tag{2.9}$$

and the condition $(a2)$ is called group property of the flow. Note that if $s = -t$, we have

$$\mathscr{T}(t+s,x) = \mathscr{T}(s+t,x) = x. \tag{2.10}$$

Implying that for all $x \in U$, under the operation defined in $(a2)$, the sets Γ_x are an additive group. Morever, $\mathscr{T}_t$ is an invertible function of x for each $t \in J_x$, such that

$$[\mathscr{T}(t,x)]^{-1} = \mathscr{T}(-t,x) \tag{2.11}$$

for all $x \in U$. The set M is open and the flow is a diffeomorphism (see Theorem 6.1 in Teschl (2012), p. 189 for more information).

The solution u might not exists for all $t \in \mathbb{R}$, however, if the solution never leaves a compact set K or if f grows at most linearly with respect to x, we can extend the solution for all $t \in \mathbb{R}_+$, and likewise for negative time (see Corollary 2.15 in Teschl (2012), p. 52). Consequently, following eq. (2.7), we also can extend the definition of local flow, for all $t \in \mathbb{R}_+$.

2.2 Limit cycle and its stability

For now, we assume that eq. (2.1) has a periodic orbit $\gamma \subset \mathbb{R}^n$, i.e., there is a $T > 0$, such that $\gamma(t+T) = \gamma(t)$ for all $t \in \mathbb{R}$, where T is the period of the periodic orbit. Since f in eq. (2.1) is at least a C^1 function, we can linearize the system setting

$$x(t) = \gamma(t) + y(t) \tag{2.12}$$

and expanding f in a Taylor series around $\gamma(t)$ to obtain

$$f[x(t)] = f[\gamma(t)] + Df[\gamma(t)][x(t) - \gamma(t)] + R(x), \tag{2.13}$$

where R is the Lagrange remainder, and by eq. (2.12), it becomes

$$f[\gamma(t) + y(t)] = f[\gamma(t)] + Df[\gamma(t)]y(t) + R(y). \tag{2.14}$$

Moreover, note that $f[\gamma(t) + y(t)] = f[\gamma(t)] + \dot{y}(t)$ implying that

$$\dot{y}(t) = Df[\gamma(t)]y(t) + R(y). \tag{2.15}$$

where $Df[\gamma(t)]$ is jacobian of the system evaluated at the point $\gamma(t) \in \mathbb{R}^n$. Neglecting the remainder we have

$$\{\dot{y}(t) = A(t)y(t), y(t_0) = y_0, \tag{2.16}$$

where $A(t) = Df[\gamma(t)]$. Moreover, by the fact of γ to be periodic implies that

$$A(t+T) = A(t). \tag{2.17}$$

We have that linear combination of solutions are again solutions. In particular, the solution corresponding to the initial condition of eq. (2.16) can be written as

$$u(t, t_0, y_0) = \sum_{j=1}^{n} u(t, t_0, \delta_j) y_{0j}, \tag{2.18}$$

where $\delta_j \in \mathbb{R}^n$ represents the canonical basis with value one in the entry j, and y_{0j} is the $jth-$component of y_0.

Thereby, it is possible to define a linear map $y_0 \mapsto u(t, t_0, y_0)$ given by

$$u(t, t_0, y_0) = \mathscr{U}(t, t_0) y_0, \tag{2.19}$$

where

$$\mathscr{U}(t, t_0) = [u(t, t_0, \delta_1), \ldots, u(t, t_0, \delta_n)] \tag{2.20}$$

for each column vector $u(t, t_0, \delta_j) \in \mathbb{R}^n$.

Note that

$$A(t)\mathscr{U}(t, t_0) = [A(t)u(t, t_0, \delta_1), \ldots, A(t)u(t, t_0, \delta_n)], \tag{2.21}$$

implying that each column of eq. (2.21) is a solution of the eq. (2.16). Thus, the whole matrix $\mathscr{U}(t,t_0)$ solves the matrix valued initial value problem

$$\left\{\dot{\mathscr{U}}(t,t_0) = A(t)\mathscr{U}(t,t_0), \mathscr{U}(t_0,t_0) = \mathbb{I} \right. \tag{2.22}$$

where we called $\mathscr{U}(t,t_0)$ as **principal matrix solution** (at t_0). By the fact of the eq. (2.17), we can see that $\mathscr{U}(t+T,t_0+T)$ also solves eq. (2.22), consequently, by the uniqueness

$$\mathscr{U}(t+T,t_0+T) = \mathscr{U}(t,t_0).$$

If we consider an initial condition on γ, it is possible to investigate what happens if the orbit move on by one period. Then, we use the well-known matrix, called monodromy matrix, given by

$$M(t_0) = \mathscr{U}(t_0+T,t_0). \tag{2.23}$$

Note that, $M(t_0)$ is also periodic, i.e.,

$$M(t_0+T) = M(t_0). \tag{2.24}$$

2.2.1 Asymptotic stability of periodic orbits

Studying the eigenvalues of the monodromy matrix is possible to know about the stability of periodic orbits, in special when the orbit is asymptotically stable. The following result shows that a monodromy matrix has at least one unit eigenvalue.

Theorem 2.2.1 (Theorem 4.50 in Meiss (2017), p. 146)**.** *The monodromy matrix $M(t_0)$ for the linearization of the system eq. (2.1), around the periodic orbit γ, always has at least one eigenvalue with value* 1.

For the next results about the stability of the periodic orbit γ, consequently, the eigenvalues of the monodromy matrix, it is necessary to introduce what is a submanifold and define a Poincaré map.

Definition 2.2.1 (Submanifold)**.** A $(n-1)-$dimensional surface Σ is called of a submanifold if it can be written as

$$\Sigma = \{x \in V : S(x) = 0\} \tag{2.25}$$

where $V \subset \mathbb{R}^n$ is open, $S \in C^k(V)$, and $\frac{\partial S}{\partial x} \neq 0$ for all $x \in \Sigma$.

The submanifold is transversal to the vector field f if

$$\left(\frac{\partial S}{\partial x}\right) \cdot f(x) \neq 0 \tag{2.26}$$

for all $x \in \Sigma$ and it will be named as a cross-section of the vector field f.

Take $x \in U$ and consider $t' \in J_x$. Let Σ be a submanifold as defined in eq. (2.2.1), and transversal to the vector field in eq. (2.1), such that $\mathscr{T}(t',x) \in \Sigma$. Then (see Lemma 6.9 in Teschl (2012), p. 197 for more information) there is a neighborhood V around x and $\tau \in C^k(V,\mathbb{R})$ with $\tau(x) = t'$, such that

$$\mathscr{T}(\tau(y),y) \in \Sigma \tag{2.27}$$

for all $y \in V$. This is important because as γ is periodic, and considering the cross-section Σ we can define the Poincaré map as

$$P_\Sigma : \Sigma \to \Sigma, \tag{2.28}$$

such that

$$P_\Sigma(y) = \mathscr{T}(\tau(y),y), \tag{2.29}$$

for all $y \in V$. Note that this replaces the flow of the $n-$dimensional continuous vector field for an $(n-1)-$dimensional map. This P_Σ maps Σ to itself and for every fixed point of the map, this corresponds to a point along the periodic orbit γ. Then, we have the following results

Theorem 2.2.2. *[Theorem 12.4 in Teschl (2012), p. 319] If $M(t_0)$ is a monodromy matrix of the periodic orbit γ, for some initial $t_0 \in \mathbb{R}$ and $x_0 \in \gamma$. Then, the eigenvalues of the $DP_\Sigma(x_0)$ plus the single value 1 coincide with the eigenvalues of the monodromy matrix $M_{x_0}(t_0)$. In particular, the eigenvalues are independent of the base point x_0 and the transversal section Σ.*

Lemma 2.2.3. *[Lemma 12.2 in Teschl (2012), p. 319] The periodic orbit γ of the eq. (2.1) is asymptotically stable if and only if $x_0 \in \gamma$ is an asymptotically stable fixed point of P_Σ (the eigenvalues of $DP_\Sigma(x_0)$ are inside the unit circle).*

Since all the eigenvalues of the Poincaré map are inside the unit circle. We specify the decay rate (see Teschl (2012), p. 71 for more details) of the orbits in a neighborhood around γ, i.e., there are positive constants C, α such that for every y around γ

$$d(\mathscr{T}(t,y),\gamma) \leq Ce^{-t\alpha}, \quad \text{for} \quad t \geq 0, \tag{2.30}$$

where

$$d(\mathscr{T}(t,y),\gamma) = \inf\{|\mathscr{T}(t,y) - x_0| : x_0 \in \gamma\} \tag{2.31}$$

is the point-set distance between the flow and the periodic orbit γ. Thus, in the rest of this chapter, we will consider that the eq. (2.1) will have an exponentially stable periodic orbit, called an exponentially stable limit cycle.

2.3 Phase oscillators

Recall eq. (2.1), since it has a periodic orbit assumed to be an exponentially stable limit cycle, we parametrize

$$\gamma : \mathbb{S}^1 \to \mathbb{R}^n \tag{2.32}$$

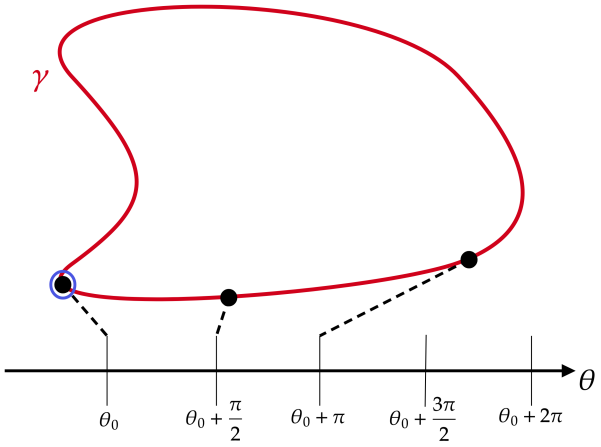

Figure 3 – The straight line represents the periodic phase θ. It parameterizes the motion of the point along the γ. The initial phase θ_0 (shown by a blue circle) can be chosen arbitrarily.

for new variable $\theta \in \mathbb{S}^1$, called phase. Thus, for every phase on $\mathbb{S}^1$ we identify to a unique point on the curve γ, such that,

$$\gamma(\theta) = \text{ point on the curve } \gamma, \tag{2.33}$$

as shown in eq. (3). By invariance of γ under the flow, i.e., if $x_0 \in \gamma$ implies that $\mathscr{T}(t,x_0) \in \gamma$ for all time, and the additive property, together with its parametrization. We have for a $\gamma(\theta_0) \in \gamma$ that $\gamma(t+\theta_0)$ also belongs to γ. Implying that the evolution of a point on γ is simply a phase shift for every $\theta_0 \in \mathbb{S}^1$.

Assuming that the θ are not static, i.e, it is moving on in respect time on $\mathbb{S}^1$. We choose a monotonic function $g : \mathbb{S}^1 \to \mathbb{R}$ such that

$$\dot{\theta} = g(\theta), \tag{2.34}$$

and introduce a new time τ, where

$$t \mapsto \tau = g(\theta)t, \tag{2.35}$$

implying that

$$\frac{d\theta(t)}{dt} = \frac{d\theta(\tau)}{d\tau}\frac{d\tau}{dt} \tag{2.36}$$

and using eq. (2.35) to obtain

$$\begin{aligned} \frac{d\theta(\tau)}{d\tau} g(\theta) &= g(\theta), \\ \frac{d\theta(\tau)}{d\tau} &= 1, \end{aligned} \tag{2.37}$$

where by this choices of parametrization and new time, we have that the flow evolves uniformly in time on the curve.

The key is to extend θ to a neighborhood of γ, such that if we introduce a weak perturbation in the ordinary differential equation it will be possible to study the system based on the information about the isolated system (the orbit γ).

We know that for every point around γ, the orbit will converge exponentially fast to γ. The neighborhood where it happens is

$$B(\gamma) := \{x \in U : \lim_{t\to\infty} d(\mathscr{T}(t,x),\gamma) = 0\} \tag{2.38}$$

where $U \subset \mathbb{R}^n$,

$$d(\mathscr{T}(t,x),\gamma) = \inf\{|\mathscr{T}(t,x) - \gamma(t)| : \gamma(t) \in \gamma\} \tag{2.39}$$

is the point-set distance similar to eq. (2.31), and the set $B(\gamma)$ it is called of basin of attraction of γ (GUCKENHEIMER; HOLMES, 1983). Furthermore, by construction, for each point $z_0 \in B(\gamma)$ we can assign a unique point $\theta_0 \in \mathbb{S}^1$ as

$$\begin{aligned} \Theta : B(\gamma) &\to \mathbb{S}^1 \\ z_0 &\mapsto \Theta(z_0) = \theta_0, \end{aligned} \tag{2.40}$$

such that

Definition 2.3.1 (Asymptotic phase value(WINFREE, 1967))**.** Consider a point $z_0 \in B(\gamma)$ and $\gamma(\theta_0) = x_0 \in \gamma$. If

$$\lim_{t\to\infty} |\mathscr{T}(t,z_0) - \gamma(t+\theta_0)| = 0, \tag{2.41}$$

we say that z_0 and x_0 has the same asymptotic phase θ_0. We denote the asymptotic phase of z_0 by $\Theta(z_0)$ as in eq. (2.40).

The next key concept is:

Definition 2.3.2 (Isochron)**.** Consider a set of points such that the asymptotic phase function is constant, i.e.,

$$I_{x_0} = \{z_0 \in B(\gamma) : \Theta(z_0) = x_0\} \tag{2.42}$$

where $x_0 \in \gamma$. This set is an isochron with base point x_0 (see fig. 4).

Isochrons are tools to help in the qualitative analysis of oscillators since the behavior of points on the same isochron looks almost the same. The following result tell us informations about these sets.

Theorem 2.3.1. *Consider the eq. (2.1), where the flow $\mathscr{T}$ is a function of class C^k, with $k \geq 1$. Assume the system has an exponentially limit cycle γ and for a small $\varepsilon > 0$, let $B_\varepsilon(\gamma) \subset B(\gamma)$ be a neighborhood of γ, such that for every inital condition $z_0 \in B(\gamma)$ it is attracted to γ when time goes to infinity. Then,*

1. *there is a unique function*

$$\alpha_x : M \to N,$$

with $M \subset \mathbb{R}$, $N \subset \mathbb{R}^{n-1}$, and $M \times N = B_\varepsilon(\gamma)$ such that I_x is an invariant graph of α under g. It means

$$g(graph(\alpha_x)) = graph(\alpha_x); \tag{2.43}$$

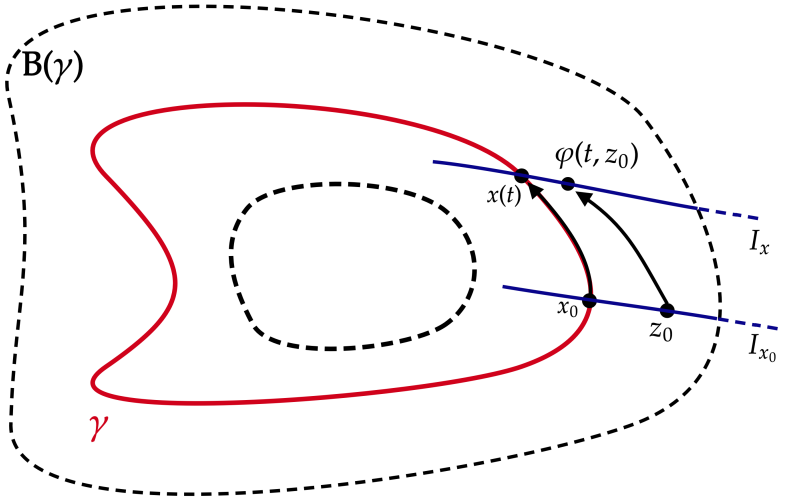

Figure 4 – Isochrons I_{x_0} and I_x inside the basin of attraction. The isochrons foliate the whole basin of attraction and the flow sends point on isochrons into isochrons. All the points on the same isochron have identical asymptotic phase values.

where

$$graph(\alpha_x) = I_x = \{(u,v) \in B_\varepsilon(\gamma) : \forall u \in M, \exists! v \in N, \text{ such that } v = \alpha_x(u)\}, \tag{2.44}$$

where g is a time one map of the flow.

2. *for every $x \neq y$ in γ, I_x is mapped to I_y under the time one map g;*

3. *the*

$$\bigcup_{x \in \gamma} I_x \tag{2.45}$$

covers the entire neighborhood $B_\varepsilon(\gamma)$ of γ, where for every $x, y \in \gamma$, $I_x \bigcap I_y = \emptyset$.

Proof. See A. □

Analytically is not always possible to compute isochrons and the techniques differs from different problems. Let us consider the simple planar example in polar coordinates

$$\begin{aligned} \dot{r} &= (1-r)r^2 \\ \dot{\theta} &= r. \end{aligned} \tag{2.46}$$

The system has an stable limit cycle when $r = 1$ and the basing of attraction is the whole plane, with the point at the origin removed. On the limit cycle the asymptotic phase is only θ and the

asymptotic phase function around the limit cycle could be defined as

$$\Theta(r,\theta) = \theta - f(r) \tag{2.47}$$

for some function f, such that $f(1) = 0$. The isochrons will be the level curves of eq. (2.47) for different values of $\Theta \in [0, 2\pi)$, i.e,

$$\Theta(r,\theta) = C, \tag{2.48}$$

where C is scalar. After some computations we can find explicitly an equation of the asymptotic phase depending on (r,θ), given by

$$\Theta(r,\theta) = \theta + 1 - \frac{1}{r}, \tag{2.49}$$

where the isochrons are draw in figure 5.

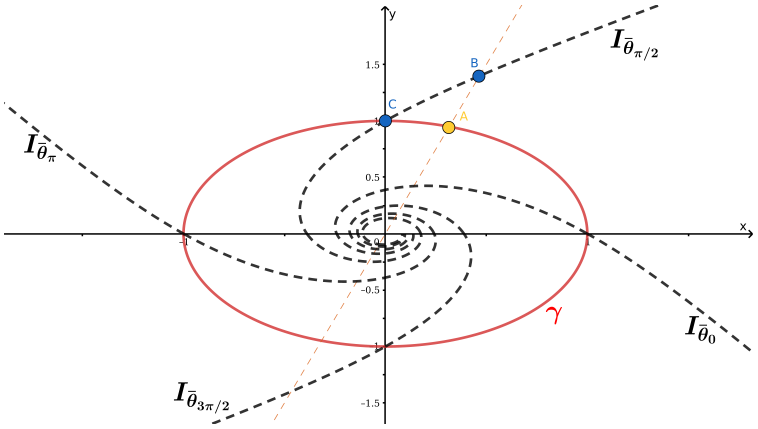

Figure 5 – Illustration of the isochrons (dashed lines) of the system (2.46). Points on the same isochron have identical asymptotic phase values, e. g., B and C. The point B outside the limit cycle γ has asymptotic value (equals to C) greater than A, even A and B sharing the same θ value between the x-axis and the dashed yellow curve.

2.4 Perturbed phase system

The fact of considering local behaviors near asymptotically stable limit cycles allow us to introduce some mathematical foundations about normally hyperbolic invariant manifolds (HOPPENSTEADT; IZHIKEVICH, 1997; ELDERING, 2013) and results about the persistence of this subject under weak perturbations (FENICHEL; MOSER, 1971; HIRSCH; PUGH; SHUB, 1977).

Let M be an invariant manifold[2], it is defined to be a Normally Hyperbolic Invariant Manifold if in the transversal directions to M, the linearization of the flow has spectrum values separate of the imaginary axis and the rate of the contraction in the transversal directions are greater than the horizontal ones along to the manifold (see eq. (6)). Then, by the previous section, γ is a normally hyperbolic invariant manifold.

[2] Briefly, a manifold is a topological space that locally resembles Euclidean space near each point (GUILLEMIN; POLLACK, 2011).

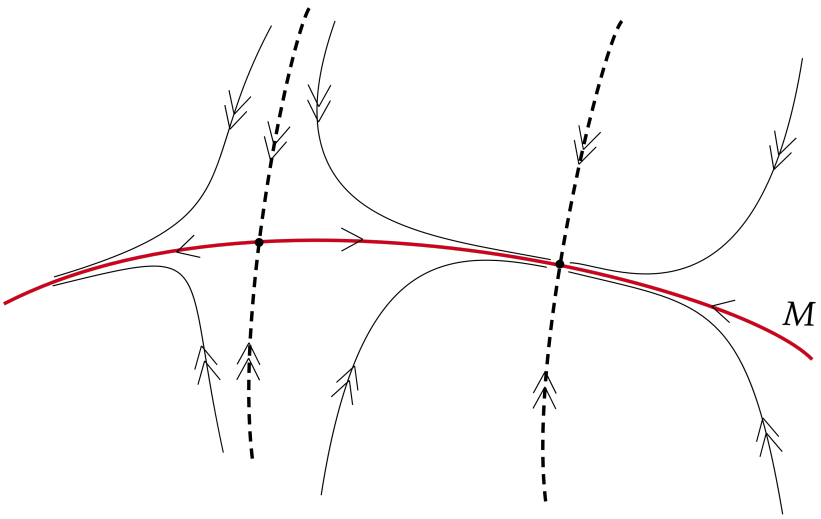

Figure 6 – Adapted from (ELDERING, 2013) where we show the transversal directions to the normally hyperbolic invariant manifold M, where the double arrows indicate a convergence rate greater than the single ones.

An important result related to normally hyperbolic invariant manifold is the persistence ((FENICHEL; MOSER, 1971; HIRSCH; PUGH; SHUB, 1977), because if a system has a normally hyperbolic invariant manifold M and it is perturbed by a weak perturbation, the new one still has the object, called M_ε, which is $\varepsilon-$close to M.

Let us recall eq. (2.1) having an asymptotically stable limit cycle γ being perturbed as follows

$$\dot{x} = f(x) + \varepsilon p(x,t), \tag{2.50}$$

where $x \in \mathbb{R}^n$, $p(x,t+T) = p(x,t)$ for all $t \geq 0$ and smooth with respect to its arguments, and $\varepsilon \ll 1$ is a small parameter indicating the intensity of the perturbation. Using the result about the persistence of normally hyperbolic invariant manifold we have that the eq. (2.50) will have a stable limit cycle $\tilde{\gamma}$ of order $\varepsilon-$close to γ.

If $\varepsilon = 0$, and $x_0 \in B(\gamma)$ such that $\mathscr{T}(t,x_0) \in B(\gamma)$. By eq. (2.40) and applying the chain rule we have

$$\begin{aligned} \frac{d\theta(t)}{dt} &= \frac{d[\Theta \circ \mathscr{T}_t](x_0)}{dt} \\ &= D\Theta(\mathscr{T}_t(x_0)) \cdot f(\mathscr{T}_t(x_0)), \end{aligned} \tag{2.51}$$

where $D\Theta(\mathscr{T}_t(x_0))$ is the jacobian of Θ at $\mathscr{T}_t(x_0)$. Thus, by eq. (2.37) the phase function should satisfies

$$D\Theta(\mathscr{T}_t(x_0)) \cdot f(\mathscr{T}_t(x_0)) = 1 \tag{2.52}$$

in the basin of attraction of γ.

If $\varepsilon \neq 0$, using the theorem 2.3.2, furnished by Hagos (2019) p. 32. We can compute the evolution of the phase function Θ in respect the time, applied at the point $\tilde{\gamma}$ as

$$\begin{aligned} \frac{d\theta(t)}{dt} &= \frac{d[\Theta \circ \tilde{\gamma}](t)}{dt} \\ &= D\Theta(\tilde{\gamma}(t)) \cdot [f(\tilde{\gamma}(t)) + \varepsilon p(\tilde{\gamma}(t), t)]. \end{aligned} \tag{2.53}$$

Since $\tilde{\gamma(t)}$ is $\varepsilon-$close to $\gamma(t)$, we set

$$\tilde{\gamma}(t) = \gamma(t) + \mathscr{O}(\varepsilon). \tag{2.54}$$

By the fact the vector field, f, the phase function Θ, and p are smooths. Considering a neighborhood of γ, we can expand them in Taylor series around $\varepsilon = 0$ to obtain

$$D\Theta[\gamma(t)]f[\gamma(t)] + \varepsilon D\Theta[\gamma(t)]p[\gamma(t), t] + \mathscr{O}(\varepsilon^2). \tag{2.55}$$

Then, using the fact of eq. (2.52) holds in the basin of attraction of γ (including γ itself), and since $0 < \varepsilon \ll 1$, we have that eq. (2.53) becomes

$$\frac{d\theta(t)}{dt} = 1 + \varepsilon D\Theta[\gamma(t)]p[\gamma(t), t], \tag{2.56}$$

which is the evolution of the perturbed phase oscillator.

CHAPTER

3

COMPLEX NETWORK EXAMPLES

We aim to show in this chapter some examples of complex networks. The complex systems arise in a wide range of applications such as social relations, e.g., as collaboration and citation networks of scientists (NEWMAN, 2001), the World-Wide Web (BRODER *et al.*, 2000), power grids (PAGANI; AIELLO, 2013), and so on. Each structure of such systems affect their performance, e.g., the topology of social networks affects the spread of information or disease (STROGATZ, 2001).

For behind applications of the complex networks, the mathematical foundation is furnished by the theory of graphs. Then, in the first sections, we intend to present some basic ideas backward of graph theory before to go into some examples of complex networks.

3.1 Graphs

The graphs usually stem from arbitrary abstractions whereas networks are more often constructed from measured data (SMALL; HOU; ZHANG, 2014). They are usually denoted by $G = (\mathcal{N}, E)$, where $\mathcal{N} \subset \mathbb{N}$ is the set of the vertices of the graph, and $E \subset \mathcal{N} \times \mathcal{N}$ denotes the set of edges of the graph. Each edge is a connection between two of the $\mathcal{N}$ vertices. Usually, vertices and edges are translated as nodes and links in complex network analysis.

From now we consider two types of graphs (complex networks) in the text

Definition 3.1.1 (Directed)**.** A graph G is said to be a directed graph if

$$E = \{(i, j) : i \neq j \text{ for all } i, j \in \mathcal{N}\}, \tag{3.1}$$

where the condition $i \neq j$ implies that we are not considering self-loops in the graph.

and **undirected graph**, i.e., whenever $(i, j) \in E$, then also $(j, i) \in E$ for all $i, j \in \mathcal{N}$. We assume that $\mathcal{N} = [N] = \{1, 2, \ldots, N\}$ is the set of labeled nodes. Moreover, there is other way to describe

the graph $G = ([N], E)$, which is from the adjacency matrix, i.e., a $N \times N$ matrix $\mathbf{A} = (A_{ij})_{i,j\in[N]}$ satisfying

$$A_{ij} = \begin{cases} 1, \text{ if } (i,j) \in E, \\ 0, \text{ otherwise.} \end{cases} \tag{3.2}$$

whose their entries encode the topology of the graph. An observation is that the adjacency matrix of an undirected graph is symmetric, i.e.,

$$A_{ij} = A_{ji} \tag{3.3}$$

for all $i, j \in [N]$. In the fig. 7 we ilustrate the directed and undirected graphs with their respective adjacency matrices.

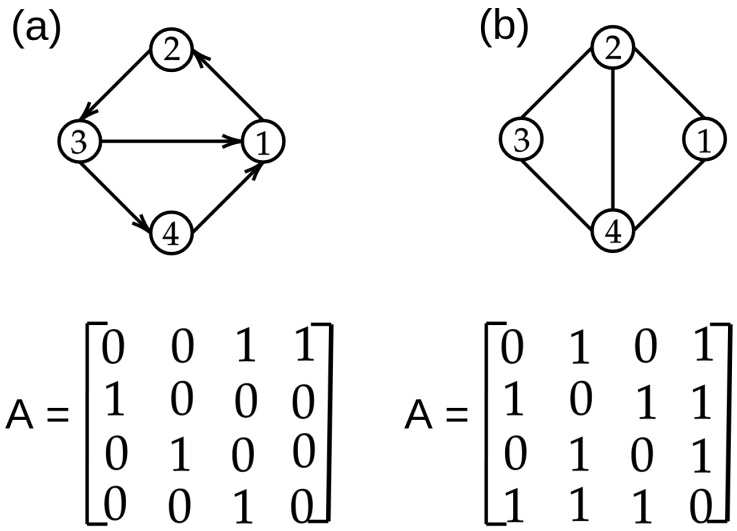

Figure 7 – (a) directed graph and its respective adjacency matrix A, and (b) a undirected graph.

From a directed graph, every vertex i has a respective in-degree (k_{in}) and out-degree (k_{out}), i.e., the numbers of incoming and outgoing edges represented as the head and nock of an arrow, respectively (see figure (colocar)). For all $i \in [N]$, they are obtained from the adjacency matrix as follow

$$k_{in,i} = \sum_{j=1}^{N} A_{ij} \quad \text{and} \quad k_{out,i} = \sum_{j=1}^{N} A_{ji}, \tag{3.4}$$

and if the graph is undirected, then $k_{in,i} = k_{out,i}$ and the degree of a vertex i is

$$k_i = \frac{k_{in,i} + k_{out,i}}{2}, \tag{3.5}$$

with $i \in [N]$, and

$$\langle k \rangle = \frac{1}{N} \sum_{i=1}^{N} k_i = \frac{2|E|}{N}, \tag{3.6}$$

where $|E|$ (or $\#E$) is the number of elements of the set of edges. Given a directed graph, the distribution of the sequence $\{k_{in,i}\}_{i=1}^{N}$ (or $\{k_{out,i}\}_{i=1}^{N}$) plays an important role in to classify between an homogenous or heterogeneous graph, i.e.,

Definition 3.1.2 (Homogeneous graph)**.** It is a graph such that all nodes have approximately the same degree, where the variance in respect to the distribution of the sequence $\{k_{in,i}\}_{i=1}^{N}$ (or $\{k_{out,i}\}_{i=1}^{N}$) is small, e.g., in the fig. 8(a) the all-to-all graph.

and

Definition 3.1.3 (Heterogeneous graph)**.** It is a graph where the variance in respect to the distribution of the sequence $\{k_{in,i}\}_{i=1}^{N}$ (or $\{k_{out,i}\}_{i=1}^{N}$) is **not** small, exhibiting a very different pattern of connectivity across the graph, e.g., in the fig. 8(b) the star graph, where there is a node (red) with high degree and the other ones with degree one.

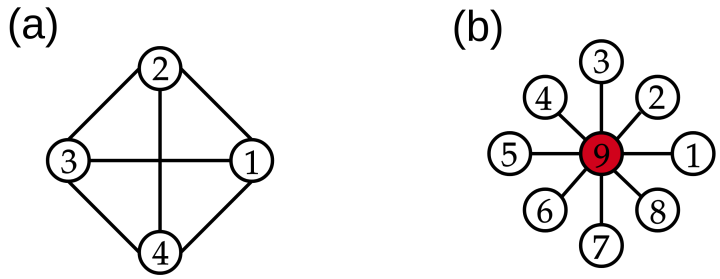

Figure 8 – (a) the all-to-all graph, where all the nodes have the same degree, and (b) the star graph, where the node 9 has the highest degree in comparison with the other ones.

Other remarkable feature of complex networks is the property of clustering, which denotes the propensity that neighbours of a given node are also neighbours of themselves. Since we could specify the graph by its adjacency matrix A this property, called local clustering coefficient, can be expressed in terms of A as

$$C_i = \frac{2}{k_i(k_i-1)} \sum_{j,k} A_{ij} A_{jk} A_{ki}, \tag{3.7}$$

for all $i \in [N]$, where k_i is given by eq. (3.5). Then, the average clustering coefficient is

$$\langle C \rangle = \frac{1}{N} \sum_{i}^{N} C_i \tag{3.8}$$

The last features of a network we intend to describe are:

- the shortest path length, i.e., the minimum number of traversed edges between the nodes i and j, given by

$$L_{i,j} = min\{d(i,j) : \text{there is a path between } i \text{ and } j\}, \tag{3.9}$$

where $d(i,j)$ is the number of edges which connects i and j (see fig. 9).

- the diameter of a graph, i.e.,

$$D = max(L_{i,j}) \tag{3.10}$$

and

- The average shortest path length

$$\langle L \rangle = \frac{1}{N(N-1)} \sum_{i,j} L_{i,j}. \tag{3.11}$$

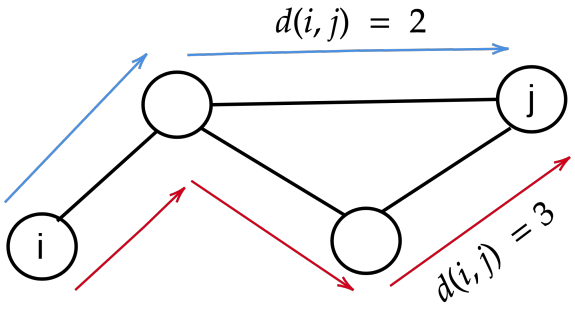

Figure 9 – Representation of the distance between two nodes in a graph. From this, we can conclude by eq. (3.9) that $L_{i,j} = 2$.

Therefore, after some basic properties of graphs we present in the next sections some models considering their structures.

3.2 Erdös-Rényi model

Consider a set of network parameters as the nodes N, and the probability p to rewire the links (or edges) fixed. Let the links be created by a random process. From this, we can try to analyze the effects of these parameters on the structure of the complex network. Erdös and Rényi (1959) started to study and describe some properties of these complex systems.

The Erdös-Rényi model is obtained as follows:

- Start with N isolated nodes (or vertices) (fig. 10(a));
- Fix some probability p. Then, for each pair of nodes, we can generate at randomly another number, called r, between 0 and 1 such that if $p > r$, you add a link between them (fig. 10(b));
- if $p = 1$ the graph is complete, it means that all possible pairs of nodes are connected by links. (fig. 10(c)).

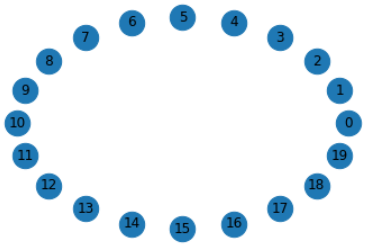

a) $p = 0$

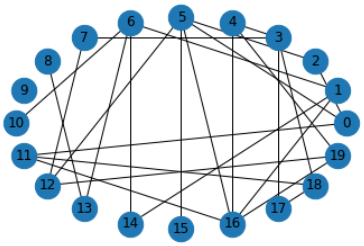

b) $p = 0.1$

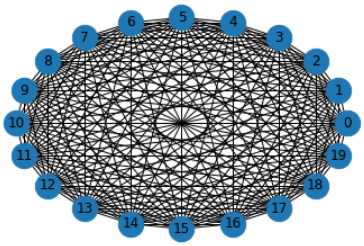

c) $p = 1$

Figure 10 – Different topologies of the Edös-Rényi model with fixed nodes $N = 20$ and considering different values of p.

The Edös-Rényi model has a characteristic concerning the degree of the nodes, because even the process is random, considering a large network, e.g., $N = 1000$ and increasing p a little, the distribution of the degrees is similar to a Poisson distribution given by

$$p(k) = \frac{e^{-\bar{k}}\bar{k}^k}{k!}, \tag{3.12}$$

where $\bar{k}$ is the average degree of the nodes in the complex network. In fig. 11, we presented an numerical simulation of a complex network considering $N = 1000$ nodes and $p = 0.05$ to see the degree distribution.

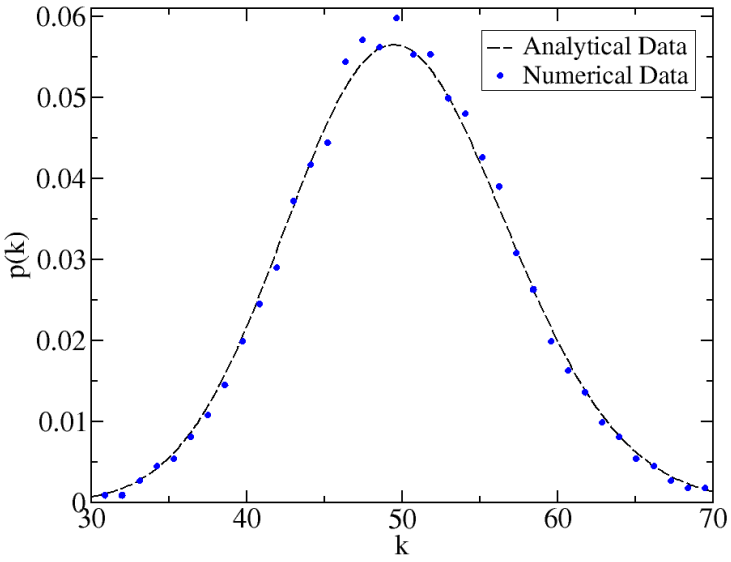

Figure 11 – The blue dots is the Edös-Rényi model considering an average of 100 realizations of $N = 1000$ nodes and probability $p = 0.05$. The dashed line is the expected distribution given by eq. (3.12)

3.3 Barabási–Albert model

As presented previously, the Edös-Rényi model has a Poisson degree distribution. However, it has been empirically observed that many networks in the real world as collaboration networks (NEWMAN, 2001), the World-Wide Web (BRODER *et al.*, 2000), and so on have a power-law distribution. The first model was introduced by Barabási–Albert (BARABáSI; ALBERT, 1999), and it will be the model described a bit below.

The idea of the construction is the following:

- Initialize with a network, it could be the Edös-Rényi model with N_0 fixed nodes;
- At each step we add a new node u to the network and connect it to $N \leq N_0$ of the existing nodes $v \in V$, where V is the set containing all the vertices of the system;
- The probability of connecting node u to v is proportional to the degree of v, i.e., we are more likely to connect new vertices to existing ones with a high degree.

From the last step, we can notice small inhomogeneities in the degree distribution during the process. In fig. 12, we simulated the Barabási–Albert model considering a network of $N = 20$ nodes. In fig. 13, we increased the number of nodes to 1000, where we can see the power-law distribution given by the blue dots and the fit is given by

$$p(k) \propto k^{-\alpha}, \tag{3.13}$$

where we obtain $\alpha \approx -3.012317$.

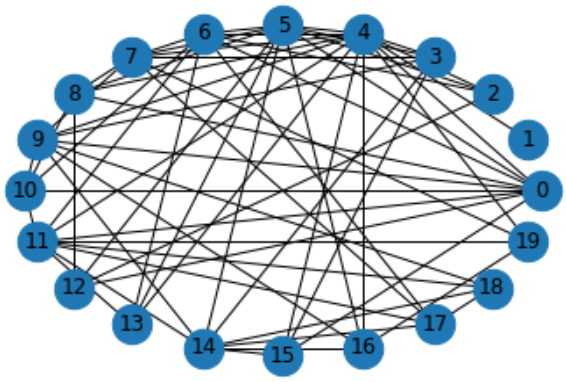

Figure 12 – Barabási–Albert model considering $N = 20$ nodes.

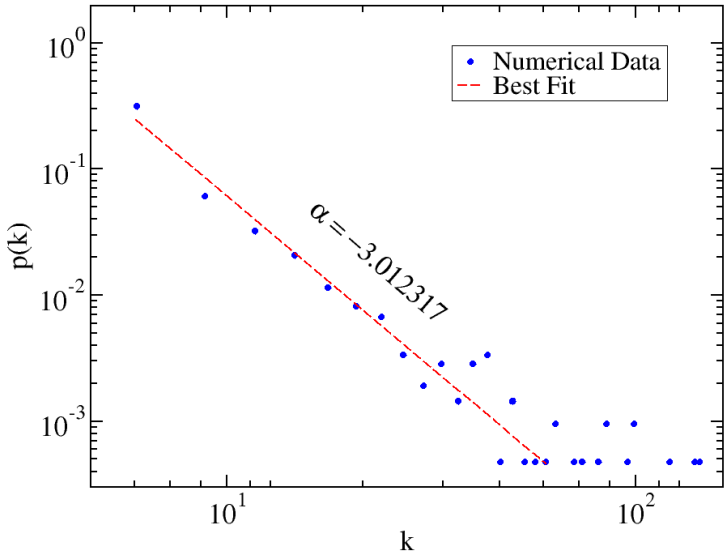

Figure 13 – The blue dots is the Barabási–Albert model considering the complex network with $N = 1000$ nodes. The red dashed line is the expected distribution given by eq. (3.13).

3.4 Watts–Strogatz model

The structure of connection in a complex system is ordinarily assumed to be either completely regular, or completely random, e.g., when you consider the Edös-Rényi model with high p. However, Watts and Strogatz (1998) created a complex network that lies somewhere between these two extremes, it is called a small-world network. The construction is the following:

- Start from a ring lattice with N vertices and k edges (or $k-$neighbors) per vertex;
- Then, we rewire each edge at random with probability p.

In fig. 14, we have the process between completely regular (fig. 14(a)) to a completely random network (fig. 14(c)), where in the middle (fig. 14(b)) we have the small-world network.

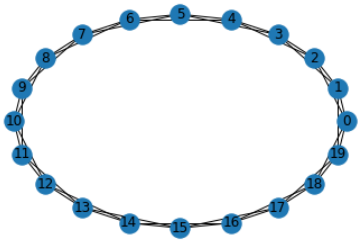

a) $N = 20$, $k = 4$, $p = 0$

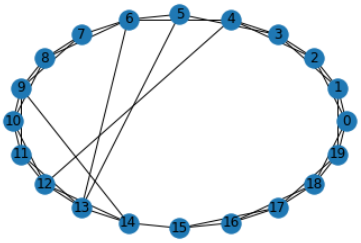

b) $N = 20$, $k = 4$, $p = 0.1$

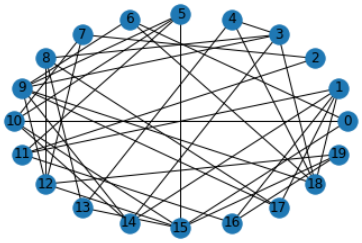

c) $N = 20$, $k = 4$, $p = 1$

Figure 14 – Different topologies of the Watts–Strogatz model with $N = 20$ fixed nodes, $k = 4$, and considering different values of p.

The structural property of small-worlds networks could be quantified consider two characteristics discussed in section 3.1

1. the average path length $L(p)$ that depends on the probability p to connect nodes and;
2. the average clustering coefficient $C(p)$ which also depends on the probability p.

The average path length $L(p)$ measures the typical separation between to vertices in the graph. Whereas the $C(p)$ processes the proportion of triangles in a network (each triangle is a sort of transitive relations between the nodes) and the potential number of triangles it can support given the degrees of its nodes (ESTRADA; KNIGHT, 2015). Thus, small-world networks are systems that can be highly clustered, like regular lattices, yet have small characteristic path lengths, like random graphs. It is seen in fig. 15, wherein the middle of the plot we have the behavior which describes exactly a small-world network.

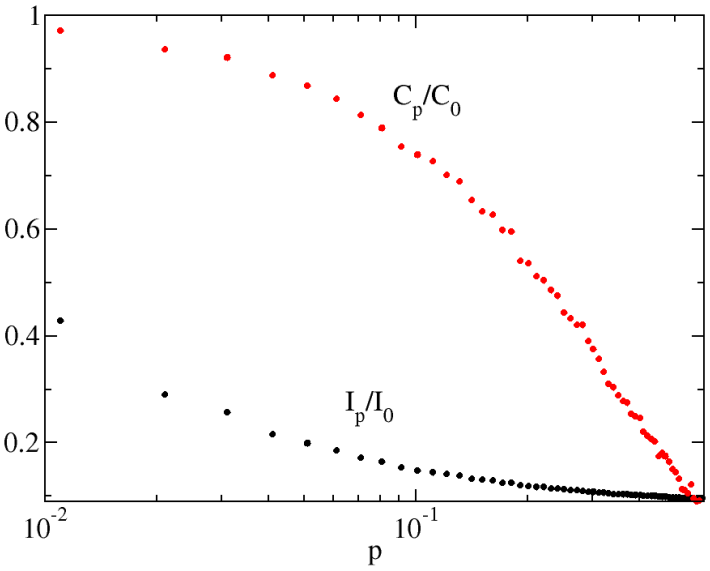

Figure 15 – $N = 500$, $k = 4$, $p = 0$ to 1

3.5 Sparse networks

The number of nodes and links of a complex network could vary widely, mainly when we consider real-networks, e.g., the world-wide-web network. However, it is always possible for every system with N nodes to verify the maximum number of connections by

$$E_{max} = \frac{N(N-1)}{2}, \tag{3.14}$$

where E_{max} represents the number all possible connections in the network, where we are not considering self-loops.

In real-networks, the number of connections is often much smaller than the maximum (MENCZER; FORTUNATO; DAVIS, 2020). Then, there is a way to quantify if the networks have or not many links, given by

$$d = \frac{|E|}{E_{max}}, \tag{3.15}$$

where d represents the density of the network, and $|E|$ (or $\#E$) is the number of elements of the set of edges. In complete graphs, the value of d is always one, and every system which has density closes to one is called a dense network.

According to Barabási and Pósfai (2016) real-networks are sparse. We define the sparsity of a complex network when

$$0 < d \ll 1, \tag{3.16}$$

even if the number of nodes N goes to infinity. Another way to check the sparsity of a complex network is analyzing if the links grow proportionally to the number of nodes, i.e.,

$$|E| \propto N, \tag{3.17}$$

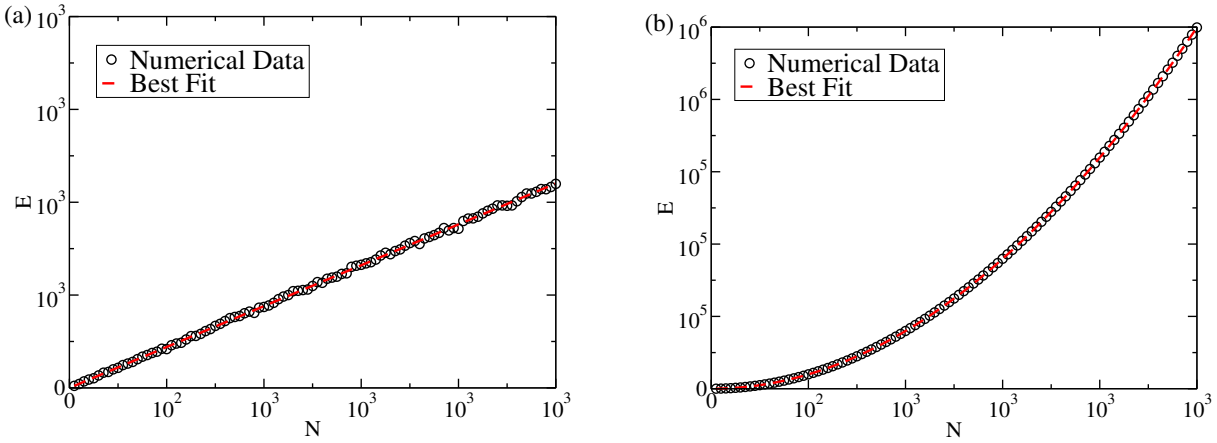

Figure 16 – (a) exhibits the growth of $|E|$ as function of N for the Newman-Watts-Strogatz model (NEWMAN; WATTS, 1999). The black circles are the simulation result, and the red dashed line is the linear fit with the coefficients $a \approx 1.1$ and $b \approx 0.18$. (b) is similar to (a), but represents the growth of a complete graph where the red dashed line is the quadratic fit with coefficients $a \approx 0.5$, $b \approx -0.5$, and $c \approx 0$.

or even slower (MENCZER; FORTUNATO; DAVIS, 2020). If instead, the number of links grow faster, for example, quadratically

$$|E| \propto N^2, \tag{3.18}$$

we say that the network is dense (MENCZER; FORTUNATO; DAVIS, 2020). In fig fig. 16(a), we represented the growth of $|E|$ as a function of N, where we considered a well-established modification of the Watts-Strogatz model (NEWMAN; WATTS, 1999). In fig. 16(b), we considered a complete complex network.

CHAPTER

4

SYNCHRONIZATION TRASITION IN COMPLEX NETWORKS

In this chapter, we define in the first section, the dynamical systems on complex networks, i.e., given a network G, for each node $i \in [N]$ we associate a coordinate θ_i, called phase variable, that describes the state of the unit on that node which evolves by time. Every node either could be or not interacting with adjacent nodes on the graph, and we will define precisely in the following. The last sections are about some important features on complex network dynamics.

4.1 Network dynamics

We define dynamics on complex networks as the triple (G, f, h), where

- G is the complex network;
- $f : \mathbb{T} \to \mathbb{T}$[1] represents the local dynamics for the isolated nodes in the network for all $i \in [N]$;
- $h : \mathbb{T} \times \mathbb{T} \to \mathbb{T}$ is the coupling function, which allows the interactions between the phase variables.

We assume that the local dynamics are periodic on $\mathbb{T}$, and putting all together, the general dynamics is a

$$\begin{cases} \dot{\theta}_i = f(\theta_i) + \sum_{j=1}^{N} h(\theta_j, \theta_i), \quad \text{for all } i \in [N], \\ \theta_i(0) = \theta_{0i}, \end{cases} \tag{4.1}$$

where the $\theta_i(0) = \theta_{0i}$ are the initial conditions.

[1] we define $\mathbb{T} = \frac{\mathbb{R}}{2\pi\mathbb{Z}}$

The eq. (4.1) is a very general approach, and at first, we are assuming the well-known Kuramoto model (KURAMOTO, 1984). The difference is that we are not considering the all-to-all configuration in the entries of the adjacency matrix A_{ij} and we consider the frustration parameter α. Thus, the model is

$$\begin{cases} \dot{\theta}_i = \omega_i + \dfrac{\varepsilon}{k_{in,i}} \displaystyle\sum_{j=1}^{N} A_{ij} \sin(\theta_j - \theta_i + \alpha), \quad \text{for all } i \in [N], \\ \theta_i(0) = \theta_{0i}, \end{cases} \tag{4.2}$$

where $N \in \mathbb{N}$ is the number of nodes in the network. For all $i \in [N]$, $\theta_i \in \mathbb{T}$ are the phase variables, $\theta_i(0) = \theta_{0i}$ are the initial conditions, $0 < \varepsilon \ll 1$ is the coupling strength, $\alpha \in [0, \frac{\pi}{2})$, and

$$k_{in,i} = \sum_{j=i}^{N} A_{ij} \tag{4.3}$$

is the in-degree of the node i. The $\omega_i \in \mathbb{R}$ are the natural frequencies of the phase variables. Usually, in the literature, they assume to be Gaussian or Cauchy distributed.

4.2 Phase synchronization phenomena

In nature, synchronization happens all the time, e.g., in an audience where the applauses start randomly, and they turn quite suddenly into synchronized clapping (NéDA *et al.*, 2000). Kuramoto (1984) observed this synchronization phenomenon considering large ensembles of oscillators, where each element interacted with all others in the all-to-all configuration.

There are two possible flavors of synchronization. The former is when a multi-oscillator system evolves into a system in which every unit θ_i does the same thing, i.e.,

$$\theta_i(t) = \theta_j(t), \tag{4.4}$$

for all $i, j = 1, \ldots, N$, implying that

$$\dot{\theta}_i = \dot{\theta}_j. \tag{4.5}$$

That means they are in the synchronous state, and the natural frequency is also identical. The last is the nodes in phase-locked, i.e. when their coordinates follow the same periodic orbit apart from a phase shift.

$$\theta_i - \theta_j = \alpha \tag{4.6}$$

where α is a constant.

Sometimes all the nodes could not be fully synchronized, i.e., when a portion of nodes are in phase-locked, and the other one is not. This sort of behavior means that the system is partially synchronized.

The last comment is that if the system does not present some of those characteristics, we say that the system is in incoherence state, i.e., when the phase oscillators are going around the unit circle at random for each unit time.

4.2.1 All-to-all Kuramoto model synchronization

Recalling all discussion in the introduction (see chapter 1), we again consider the order parameter

$$r : \mathbb{T}^N \to [0,1], \tag{4.7}$$

such that for every $t \in \mathbb{R}_+$, we have

$$r(\theta_1(t), \ldots, \theta_N(t)) = \frac{1}{N}\left\| \sum_{j=1}^{N} e^{i\theta_j(t)} \right\|, \tag{4.8}$$

where N is the number of oscillators, θ_j are the phases oscillators, and r is ranging from incoherence state ($r \approx 0$), where the system is not synchronized, to coherence state ($r \approx 1$), indicating that the system is synchronized. In fig. 17, considering K as the coupling strength, we have a simulation of the order parameter from eq. (4.8) considering an network with $N = 1000$ oscillators.

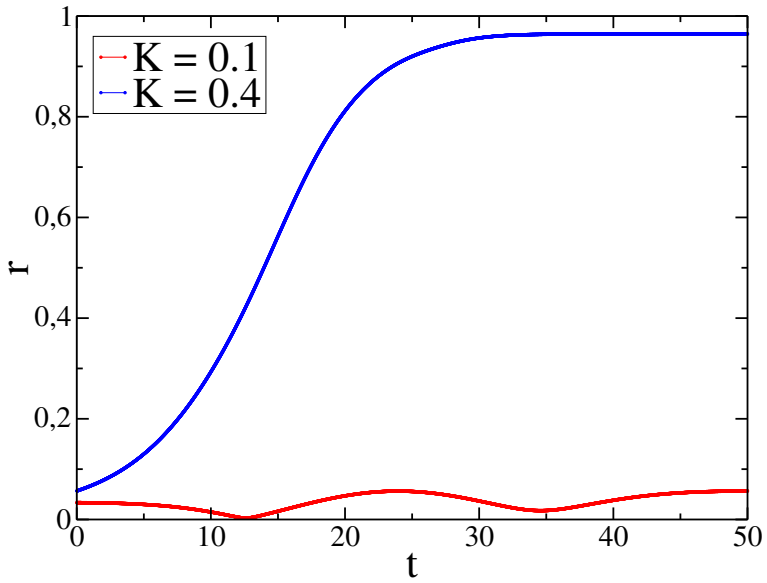

Figure 17 – The order parameter behavior as a function of time where we consider two distinct situations during the simulations of the model eq. (4.2) and eq. (4.8). In both, we consider $N = 1000$ oscillators, and the ω_i are normally distributed. We take K different values as labeled in the figure. The blue line shows that the system after some time synchronizes ($r \approx 1$), however the red one, the system stays on an incoherence regime ($r \approx 0$) without synchronizing.

From fig. 17, we can notice that for different values of K the behaviors to synchronization are different. Then, if we look at r as a function of the parameter K we can draw the bifurcation diagram and analyze precisely the influence of K in the synchronous states of the system. In fig. 18, we simulated this result and Kuramoto (1984) derived exact results for K_c and it was discussed by Strogatz (2000), where K_c is given by

$$K_c = \frac{2}{\pi g(\bar{\omega})}, \tag{4.9}$$

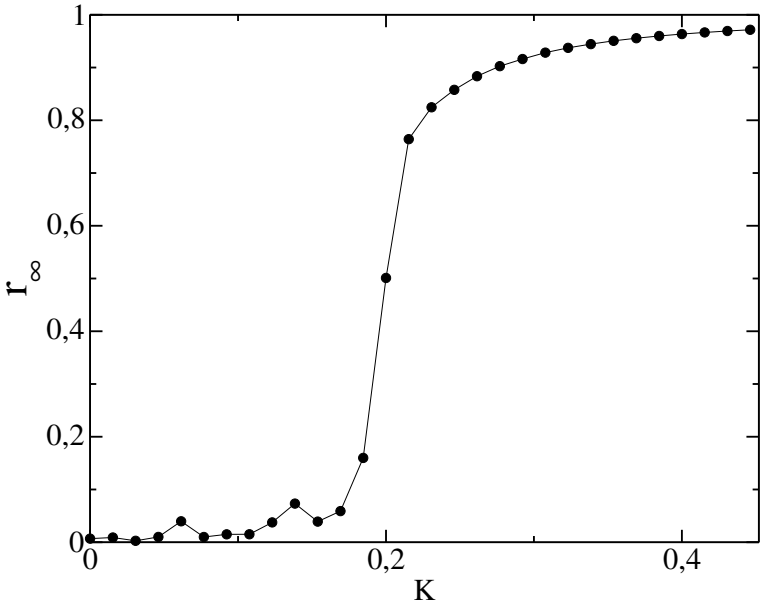

Figure 18 – Bifurcation diagram of the Kuramoto model, considering the normal distribution with $N = 5000$

where g is the distribution of the natural frequencies for a large $N-$oscillators. In fig. 18, we simulated using a normal distribution with $g(0) = 4$, hence we obtained $K_c \approx 0.16$.

In fig. 18, we can notice that the transition to synchronization is continuous and Strogatz (2000) found that after $K > K_c$, r, obeys the following growth

$$r \propto |K - K_c|^{1/2}. \tag{4.10}$$

4.3 Discontinuous transition

A discontinuous transition, also known as a first-order transition, refers to a qualitative change in the behavior of a system where there is an abrupt and discontinuous jump in a certain order parameter as a control parameter, such as coupling strength or network density, crosses a critical value.

In the context of complex networks, a discontinuous transition signifies a sudden and sharp change in the collective behavior of the networked oscillators. This phenomenon can be observed in synchronization transitions, where a network transitions from a desynchronized state to a synchronized state.

4.3.1 Phase model

Following the studies from Toenjes, Masuda and Kori (2010). For every node i of the complex network, we associate a phase $\theta_i \in \mathbb{T}$, such that the dynamics of the network is given by the the Kuramoto model from section (4.1), eq. (4.2)

Since $\varepsilon > 0$ we can re-scale time such that $t \mapsto t' = \frac{t}{\varepsilon}$, and in a co-rotating frame of reference where the natural frequencies ω_i of the oscillators are identical, we can rewrite the model in eq. (6.7) as follows

$$\begin{cases} \dot{\vartheta}_i(t) = \dfrac{1}{k_{in,i}} \displaystyle\sum_{j=1}^{N} A_{ij} \sin(\vartheta_j(t) - \vartheta_i(t) + \alpha), \quad \text{for all } i \in [N], \\ \vartheta_i(0) = \vartheta_{0i}. \end{cases} \tag{4.11}$$

The overall synchrony is described by the order parameter

$$r(t) = \frac{1}{N} \left\| \sum_{j=1}^{N} e^{i\vartheta_j(t)} \right\|, \tag{4.12}$$

where in the fig. 19 we see the global behavior of the system with respect to the asymptotic behavior of the order parameter, where see the discontinuous transition observed by Toenjes, Masuda and Kori (2010).

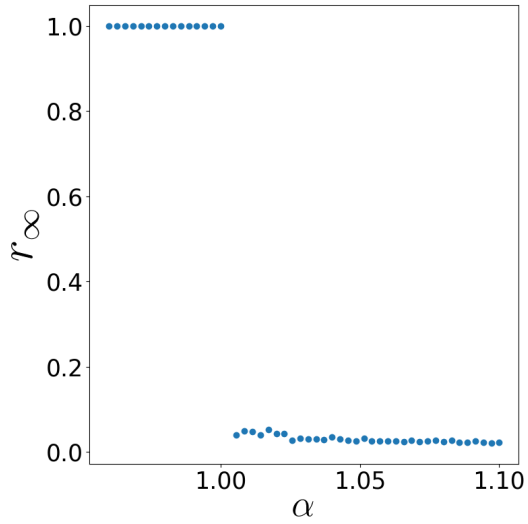

Figure 19 – Global transition for the phase model eq. (6.8), considering the asymptotic behavior of the order parameter eq. (6.9). For this simulation, we consider $N = 800$ interacting units uniformly distributed between 0 to 2π, $\sigma = 1$ and after $n = 10^4$ iterations, we took the ϑ_i for $i = 1, \ldots, N$ to compute one of the 50 values of r_∞. Note that for $\alpha < \alpha_c$, the value of the $r_\infty \approx 1$, implying that the system is completely synchronized. However, for $\alpha > \alpha_c$, we have a discontinuous transition between the synchronous to asynchronous state.

CHAPTER

5

STOCHASTIC PROCESS AND SOME FEATURES

In this chapter, we aim to define and describe some properties about stochastic process.

5.1 Some definitions of probability theory

In this section, we give some definitions of concepts of probability, but we do not get deep into it. For more details about it, look at James (2015).

We are going to study experiments or random process considering

Definition 5.1.1 (Probability space)**.** A probability space is a triple $(\Omega, \mathscr{F}, P)$, such that

1. Ω it is called of sample space that contains all possible outcomes for an experiment.

   Example 1. Toss a coin $n-$times, then

   $$\Omega = \{\omega = (\omega_1, \omega_2, \ldots, \omega_n) : \omega_i = H \text{ or } T, \forall i = 1, \ldots, n\}, \tag{5.1}$$

   where $H = Head$ and $T = Tail$.

2. $\mathscr{F}$ is a $\sigma-$algebra of Ω, i.e.,

   a) $\emptyset \in \mathscr{F}$ and $\Omega \in \mathscr{F}$;

   b) If $A \in \mathscr{F}$, then $A^c \in \mathscr{F}$;

   c) For all $A_1, A_2, \ldots \in \mathscr{F}$, the

   $$\bigcap_{i=1}^{\infty} A_i \text{ and } \bigcup_{i=1}^{\infty} A_i \in \mathscr{F}. \tag{5.2}$$

Remark. That means $\mathscr{F}$ is closed through the operations of countable unions, intersections, and relative complement.

3. $P : \mathscr{F} \to [0,1]$ is the probability function, such that

   a) For a nonempty set A, $P(A) > 0$, for all $A \in \mathscr{F}$;

   b) $P(\Omega) = 1$, $P(\emptyset) = 0$;

   c) $P(\bigcup_{i=1}^{\infty} A_i) \leq \sum_{i=1}^{\infty} P(A_i)$.

From some random experiments, we can analyze the numerical aspects of it. The way to extract such pieces of information is using random variables, defined as

Definition 5.1.2 (Random variable)**.** Let $(\Omega, \mathscr{F}, P)$ be a probability space. A function

$$X : \Omega \to R$$

is a random variable if the pre-image

$$X^{-1}(U) := \{\omega \in \Omega : Y(\omega) \in U\} \in \mathscr{F},$$

for all open subsets $U \subset R$.

Example 2. Let $(\Omega, \mathscr{F}, P)$ be a probability space. Taking a subset $E \subset \Omega$, the function defined as

$$1_E : \Omega \to R$$

such that

$$1_E(\omega) = \begin{cases} 1 \text{ ,If } \omega \in E, \\ 0 \text{ , If } \omega \notin E \end{cases} \tag{5.3}$$

is a random variable if $E \in \mathscr{F}$. This function is is called indicator function.

If $\Omega =$ "faces of a dice", $\mathscr{F} = \{\emptyset, \text{ even faces, odd faces, } \Omega\}$ and consider $E = \{2,4,6\}$. Then,

$$1_E(\omega) = \begin{cases} 0 \text{ ,If } \omega = 1, \\ 1 \text{ ,If } \omega = 2, \\ 0 \text{ ,If } \omega = 3, \\ 1 \text{ ,If } \omega = 4, \\ 0 \text{ ,If } \omega = 5, \\ 1 \text{ , If } \omega = 6 \end{cases} \tag{5.4}$$

is a random variable.

The random variable X could be

- **discrete**, i.e., there exists a finite or countable set $\{x_1, x_2, ...\} \subset R$, such that $X(\omega) \in \{x_1, x_2, ...\}$, for all $\omega \in \Omega$, or;

- **continous**, i.e., there is an uncountable set of possible outcomes, e.g., the possible values of the temperature outside on any given day.

Definition 5.1.3. The distribution function of random variable X, denoted as F_X or simply F is defined as

$$F_X(x) = P(X \leq x), \quad x \in \mathbb{R}, \tag{5.5}$$

satisfying the following properties:

1. If $x \leq y$, it implies that $F(x) \leq F(y)$, i.e., F is not a decreasing;
2. F is right-continuous, i.e.,
$$\lim_{x \to y^+} F(x_n) = F(y);$$
3. The
$$\lim_{x \to -\infty} F(x) = 0 \quad \textit{and} \quad \lim_{x \to +\infty} F(x) = 1,$$
i.e.,
$$F(x) \in [0, 1].$$

Remark. The distribution function is also often called the cumulative distribution function (CDF).

If X is a discrete random variable, the distribution function is

$$F_X(x) = \sum_{i: x_i \leq x} P(X = x) = \sum_{i: x_i \leq x} p(x_i), \tag{5.6}$$

otherwise, if X is a continuous random variable and there is a integrable function $f : \mathbb{R} \to \mathbb{R}_+$, such that

$$\int_{-\infty}^{+\infty} f(x)dx = 1. \tag{5.7}$$

The distribution function of X is

$$F_X(x) = \int_{-\infty}^{x} f(t)dt, \quad \forall x \in \mathbb{R}. \tag{5.8}$$

The function f is called probability density function of X.

The last three concepts will be useful later on to describe the characteristics of stochastic processes. They are

1. **expected value**: let X be a continuous random variable with distribution function F. The expected value of X is defined as
$$E[X] = \int_{-\infty}^{+\infty} xf(x)dx. \tag{5.9}$$
Remark. The expected value (or mean) could be denoted as μ_X as well.

2. **variance**: the variance of a continuous random variable X is

$$Var[X] = E[(X - E[X])^2] = \int_{-\infty}^{+\infty} (x - E[X])^2 f(x) dx. \tag{5.10}$$

Remark. The variance is also denoted as σ_X^2.

3. **covariance**: let X and Y be two random variables with the joint probability density function

$$F_{XY}(x,y) = \int_{-\infty}^{x} \int_{-\infty}^{y} f_{XY}(x',y') dy' dx', \quad \forall x', y' \in \mathbb{R}. \tag{5.11}$$

The covariance between X and Y is

$$Cov[X,Y] = E[(X - E[X])(Y - E[Y])] = \int_{-\infty}^{+\infty} \int_{-\infty}^{+\infty} (x - E[X])(y - E[Y]) f_{XY}(x,y) dy dx. \tag{5.12}$$

5.2 Stochastic Process and some examples

Stochastic (or random) processes are collections of measurements indexed either by time or outcomes from an experiment. It is defined as

Definition 5.2.1 (Stochastic Process)**.** Let $(\Omega, \mathscr{F}, P)$ be a probability space and (S, Σ) a measurable space[1]. A stochastic process is a function of two variables (t, ω), where t belongs to some nonempty index set I, and ω is an outcome of some sample space Ω. It could be represented in two manners, as

- the sequence $\{X(t,\cdot) : t \in I\}$ of random variables, where

$$X(t,\cdot) : \Omega \to S$$

represents a random variable indexed by $t \in I$. It is also denoted by $\{X_t\}_{t \in I}$ or $\{X_t\}$;

- the sequence $\{X(\cdot,\omega) : \omega \in \Omega\}$ of sample functions of time, where

$$X(\cdot,\omega) : I \to S$$

represents a sample function of the process indexed by the outcome $\omega \in \Omega$.

Remark.

- Even the definitions (1) and (2) in 5.2.1 looking be different, actually they produce the same stochastic process;
- X_t and X_ω are only a random variable and a sample function, respectively. They are not the whole stochastic process;

[1] A measurable space is tuple where S is the state space, e.g., $S = \mathbb{R}$ equipped with a sigma-algebra Σ, e.g., Σ is the Borel sigma-algebra of $\mathbb{R}$.

- As an abuse of notation, X_t will be to denote both, where we are specifying the difference using random variable or sample function.

The stochastic process could be discrete or continuous time, i.e.,

- **discrete**: consider the stochastic process $\{X_t : t \in I\}$. It is a discrete-time process if the index set I is finite or countable. In practice

$$I = \{0, 1, 2, \ldots\},$$

implying that

$$\{X_0, X_1, X_2, \ldots\}$$

is a collection of random variables which are associated with every time $t = 0, 1, 2, \ldots$

- **continuous**: consider the stochastic process $\{X_t : t \in I\}$. It is a continuous-time process if the index set I is not finite or countable. In practice

$$I \subseteq [0, \infty)$$

implying that

$$\{X_t : t \in I\}$$

is a collection of random variables X_t, which are associated with every instant of time $t \in I$.

Let us look at some examples of the stochastic process.

Example 3. Let the stochastic process be the sequence $\{X_k : k \in \mathbb{N}\}$ of random variables, where

$$X_k : \Omega \to \mathbb{R}$$

such that

$$X_k = X(k, \cdot) \sim \mathcal{N}(0, 1), \quad \forall k \in \mathbb{N}. \tag{5.13}$$

The simple representation of this process is in fig. 20

Example 4. Consider $\Omega = (0, 2\pi)$ as the sample space, and a random variable X with a uniform distribution on the interval $(0, 2\pi)$, such that

$$X : \Omega \to (0, 2\pi)$$

is the identity map

$$X(\omega) = \omega.$$

Let the stochastic process be the sequence $\{Y_\omega : \omega \in \Omega\}$ of sample functions, where

$$Y_\omega : \mathbb{R} \to \mathbb{R},$$

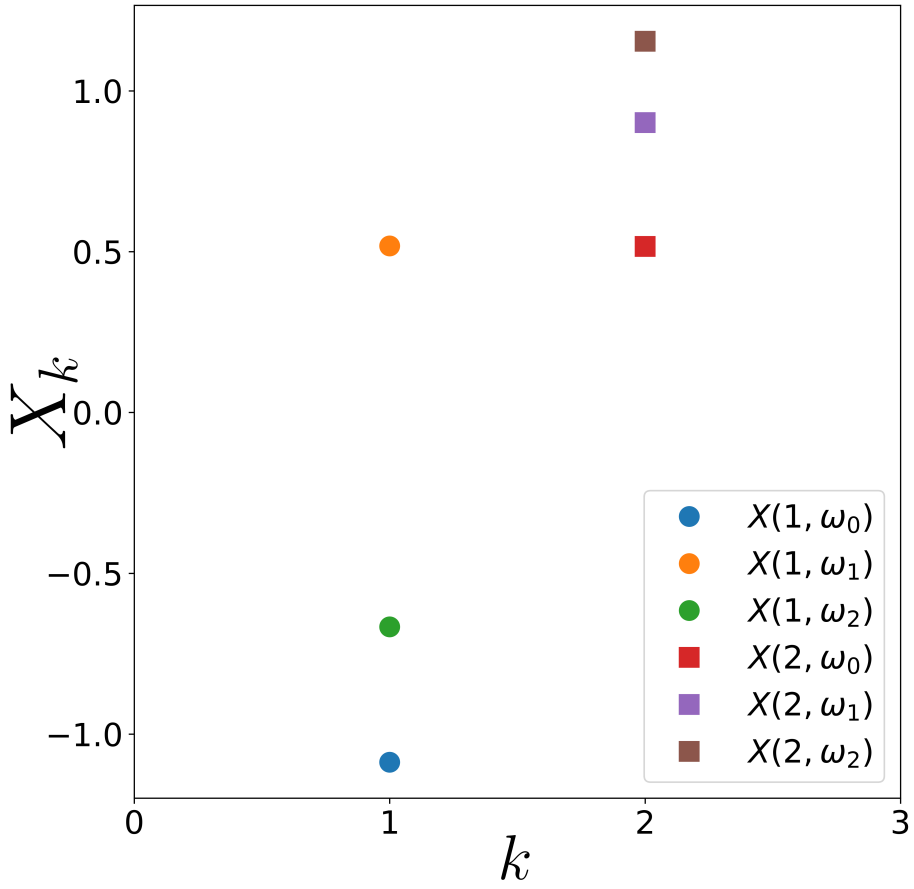

Figure 20 – Shows for $k = 1$ and $k = 2$ the realizations of the stochastic process given by eq. (5.13).

such that

$$Y_\omega = Y(\cdot,\omega) = \cos(t+\omega), \quad \forall \omega \in \Omega. \tag{5.14}$$

The simple representation of this process is in fig. 21, where for every value of ω, we have a sample function.

In the last example, we show the stochastic process considering the two topics in the definition 5.2.1.

Example 5. Let $\Omega_1 = [1,3]$ and $\Omega_2 = [-1,1]$ be sample spaces, and the random variables Y and W with uniform distributions on the intervals $[1,3]$ and $[-1,1]$ respectively, such that

$$\begin{aligned} Y &: \Omega_1 \to [1,3], \\ W &: \Omega_2 \to [-1,1] \end{aligned} \tag{5.15}$$

are the identity maps, i.e.,

$$\begin{aligned} Y(\omega_1) &= \omega_1, \\ W(\omega_2) &= \omega_2. \end{aligned} \tag{5.16}$$

Consider the following stochastic process

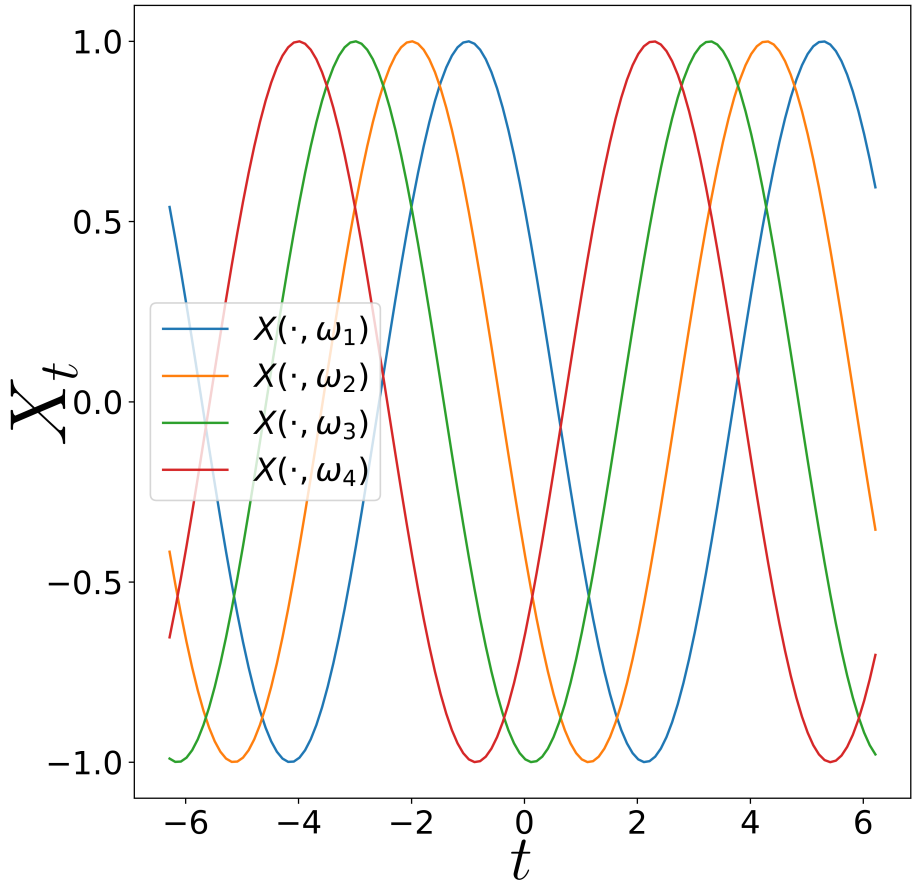

Figure 21 – Shows some sample functions for $\omega_1 = 1$, $\omega_2 = 2$, $\omega_3 = 3$, and $\omega_4 = 4$ for all $t \in [-2\pi, 2\pi]$.

- using the first definition

$$X_t : \Omega \to \mathbb{R},$$

where $\Omega = \Omega_1 \times \Omega_2$, such that

$$X_t = X(t,\cdot) = \omega_1 t + \omega_2 \cos(\pi t), \tag{5.17}$$

for every $t \in \mathbb{R}$.

- and the second definition

$$X_\omega : \mathbb{R} \to \mathbb{R},$$

such that

$$X_t = X(\cdot,\omega) = \omega_1 t + \omega_2 \cos(\pi t), \tag{5.18}$$

for every $\omega = (\omega_1, \omega_2) \in \Omega$.

Then, the fig. 22(a) and fig. 22(b) show the representation of the stochastic process following these two definitions for some values of t and ω.

There are ways to characterize stochastic process, e.g.,

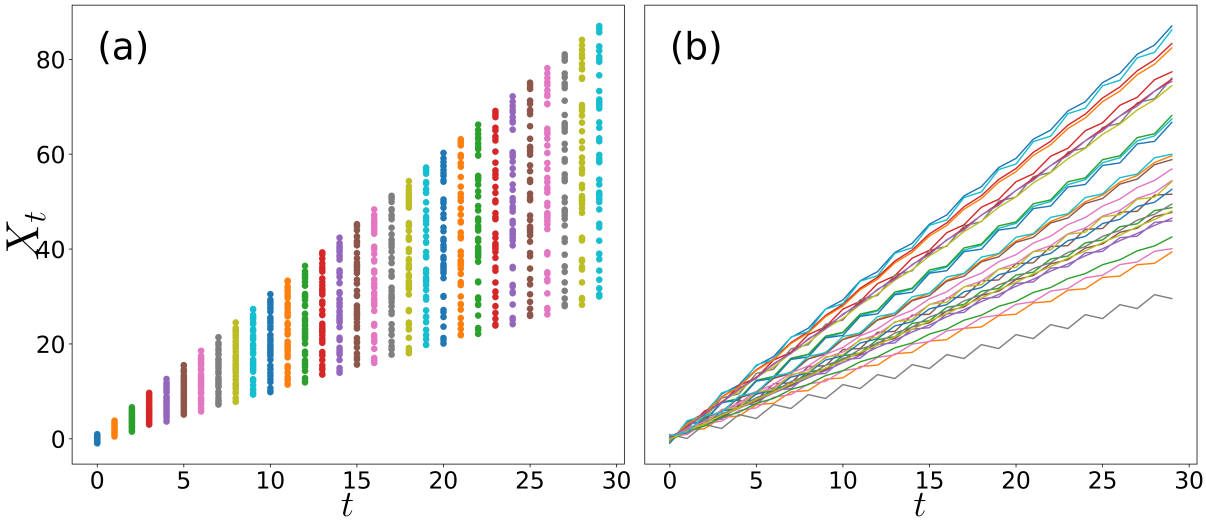

Figure 22 – (a) shows the stochastic process given by eq. (5.17) for some fixed values of t, and (b) shows the same stochastic process, but following eq. (5.18) for some fixed values of ω.

Definition 5.2.2 (I.I.D. Stochastic Process)**.** Let $\{X_k : k \in \mathbb{N}\}$ be a stochastic process, this random process is independent identically distributed (i.i.d) process if for all $k \in \mathbb{N}$ the random variables X_k are idenpendent and identically distributed, i.e.,

$$\begin{aligned} F_{X_1}(x) &= F_{X_k}(x), \quad \forall k \in \mathbb{N} \quad \textit{and} \quad x \in \mathbb{R}, \\ F_{X_1,\ldots,X_k}(x_1,\ldots,x_k) &= F_{X_1}(x_1)\cdot\ldots\cdot F_{X_k}(x_k), \quad \forall x_1,\ldots,x_k \in \mathbb{R}. \end{aligned} \tag{5.19}$$

The example example 3 is a i.i.d random process.

Definition 5.2.3 (S.S.S. random process)**.** Let $\{X_t : t \in \mathbb{R}\}$ be a stochastic process, it is a strict-sense stationary (SSS) random process if, for all $t_1,\ldots,t_r \in \mathbb{R}$, $\tau \in \mathbb{R}$, and the real numbers $x_1,\ldots,x_r$, we have

$$F_{X_{t_1},\ldots,X_{t_r}}(x_1,\ldots,x_r) = F_{X_{(t_1+\tau)},\ldots,X_{(t_r+\tau)}}(x_1,\ldots,x_r). \tag{5.20}$$

The examples 3 and 4 are SSS random process.

Since SSS stochastic processes require access to the full characterization ($r-$point CDF's), they are hard to show. Hence using partial features of a stochastic process such as expected value, variance, and covariance, we can define

Definition 5.2.4 (W.S.S stochastic process)**.** Let $\{X_t : t \in \mathbb{R}\}$ be a stochastic process. It is a wide (or weak) sense stationary (WSS) process if it has expected value independent of time, finite variance, and the (auto)covariance depends only on the time difference $t_2 - t_1$, i.e.,

$$\begin{cases} \mu_X(t_1) = \mu_X(t_2) \quad \forall t_1,t_2 \in \mathbb{R}, \\ Cov[X_{t_1},X_{t_2}] = Cov[X_{t_1-t_2},X_0], \quad \forall t_1,t_2 \in \mathbb{R}, \\ Var[X_t] < \infty, \quad \forall t \in \mathbb{R}. \end{cases} \tag{5.21}$$

Remark. If we have a SSS process, it implies that we have a WSS process as well, but the converse is not always true.

Example 6. Consider the following discrete time stochastic process

$$X_k : \Omega \to \mathbb{R},$$

such that

$$\forall k \in \mathbb{Z} \quad X_k \sim \begin{cases} \mathscr{U}(-\sqrt{3},\sqrt{3}),\ if\ k\ is\ odd, \\ \mathscr{N}(0,1),\ if\ k\ is\ even, \end{cases} \tag{5.22}$$

It implies that

$$\begin{cases} \mu_X(k) = 0, \quad \forall k \in \mathbb{Z}, \\ \sigma_X^2(k) = 1, \quad \forall k \in \mathbb{Z}, \\ Cov[X_{k_1}, X_{k_2}] = \begin{cases} 1,\ if\ k_1 = k_2, \\ 0,\ if\ k_1 \neq k_2 \end{cases} = \delta(k_1 - k_2). \end{cases} \tag{5.23}$$

Then, this process is a WSS process because it fits in every condition from definition definition 5.2.4. However, it breaks in to be a SSS process because

$$F_{X_{2k_1},\ldots,X_{2k_r}}(x_1,\ldots,x_r) \neq F_{X_{(2k_1+1)},\ldots,X_{(2k_r+1)}}(x_1,\ldots,x_r). \tag{5.24}$$

for all $k_1, k_2, \ldots, k_r \in \mathbb{Z}$.

5.3 Autocovariance function, Fourier Transform and Power spectral density

5.3.1 Autocovariance function

From the above definitions, since we have the covariance depending only on the time difference, if we define $\tau = t_2 - t_1$, we can analyze what happened with a signal when we shift the process by this time lag. Thus, considering a wide-sense stationary process, we define

Definition 5.3.1 (Autocovariance function)**.** Let $\{X_t : t \in R\}$ be a WSS stochastic process, the autocovariance function is

$$\begin{aligned} K_X(\tau) = Cov[X_{t+\tau}, X_t] &= E[(X_{t+\tau} - \mu_{t+\tau})(X_t - \mu_t)], \\ &= E[X_{t+\tau}X_t] - \mu^2. \end{aligned} \tag{5.25}$$

If $\sigma^2 \neq 0$, the normalized autocovariance function is

$$\rho_{XX}(\tau) = \frac{Cov[X_{t+\tau}, X_t]}{\sigma^2} = \frac{E[X_{t+\tau}X_t] - \mu^2}{\sigma^2}, \tag{5.26}$$

such that if $\tau = 0$

$$Cov[X_{t+0}, X_t] = E[(X_{t+0} - \mu_{t+0})(X_t - \mu_t)] = E[(X_t - \mu_t)^2] = \sigma^2 \tag{5.27}$$

hence

$$\rho_{XX}(0) = 1. \tag{5.28}$$

Some properties of the autocovariance function, considering a W.S.S stochastic process, are

1. If $\tau = 0$ from eq. (5.27) we have

$$\begin{aligned} K_X(0) &= E[(X_t - \mu_t)^2], \\ &= Var[X_t] < \infty; \end{aligned} \tag{5.29}$$

2. the autocovariance function is symmetric, i.e.,

$$\begin{aligned} K_X(-\tau) &= E[(X_t - \mu_t)(X_{(t-\tau)} - \mu_{(t-\tau)})], \\ &= E[(X_{s+\tau} - \mu_{s+\tau})(X_s - \mu_s)], \\ &= K_X(\tau) \end{aligned} \tag{5.30}$$

   where $s = t - \tau$, such that $s \in \mathbb{R}$.

3. The autocovariance function is bounded, indeed, by $K_X(0)$, i.e.,

$$|K_X(\tau)| \leq K_X(0), \quad \forall \tau in \mathbb{R}. \tag{5.31}$$

   This follows by the Cauchy-Schwarz inequality (see Lapidoth (2017), p. 23 for more details).

5.3.2 Fourier transform

Physical signals can be decomposed into several discrete frequencies or a spectrum of frequencies over a continuous range. The Fourier transform is the mathematical operation for it. This also changes the domain ($x-$axis) of a signal from time to frequency.

Moreover, the Fourier transform tells you what frequencies make up your signal and how strong they are. Even if your data contains noise, the Fourier transform allows us to look at through the noise and see which frequencies matter. The definition is the following

Definition 5.3.2 (Fourier transform)**.** It is an integral transform that decomposes an integrable function

$$f : \mathbb{R} \to \mathbb{C} \quad (or\ \mathbb{R})$$

into its constituent frequencies ξ, such that

$$\hat{f}(\xi) = \int_{-\infty}^{+\infty} f(x) e^{-2\pi i x \xi} dx, \quad \forall \xi \in \mathbb{R}, \tag{5.32}$$

where the inverse transform is

$$f(x) = \int_{-\infty}^{+\infty} f(\xi) e^{2\pi i x \xi} d\xi, \quad \forall x \in \mathbb{R}, \tag{5.33}$$

Example 7. Consider the function $f : R \to R$ such that

$$f(t) = \cos(\omega_0 t), \tag{5.34}$$

where $\omega_0 = 2\pi\xi_0$. Then, the Fourier transform of f is

$$\begin{aligned} \hat{f}(\xi) &= \int_{-\infty}^{\infty} \cos(\omega_0 t) \cdot \mathrm{e}^{-2\pi i \xi t} \mathrm{d}t \\ &= \frac{1}{2} \int_{-\infty}^{\infty} \left(\mathrm{e}^{i(\omega_0 - \omega)t} + \mathrm{e}^{-(\omega_0 + \omega)t} \right) \mathrm{d}t \\ &= \frac{1}{2} \left[\delta(\omega - \omega_0) + \delta(\omega + \omega_0) \right], \end{aligned} \tag{5.35}$$

where $\omega = 2\pi\xi$. In fig. 23 we show this example for $\omega_0 = 1$, considering just the positive part $\delta(\omega - \omega_0)$ of eq. (5.35).

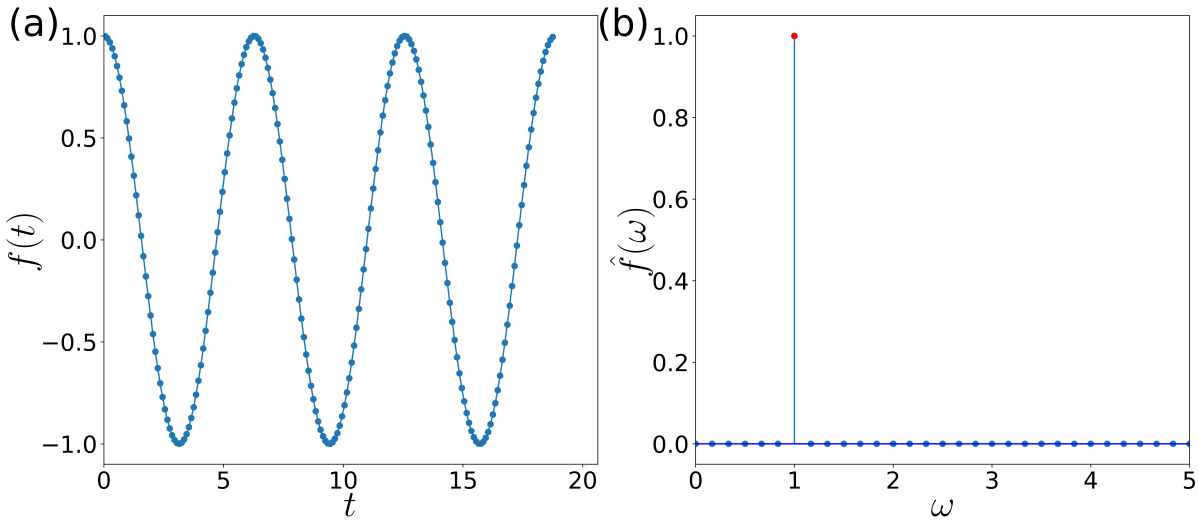

Figure 23 – (a) shows the eq. (5.34) for $\omega_0 = 1$ as function of time and (b) represents its respective Fourier transform considering just the positive part $\delta(\omega - \omega_0)$ of eq. (5.35) as a function of the natural frequency ω.

5.3.3 Power spectrum density

An important result relating autocovariance function and the Fourier transform is the following

Theorem 5.3.1 (See Lapidoth (2017), p. 571)**.** *If the autocovariance function* K_X *is continuous at the origin and integrable, then its Fourier Transform* $\hat{\mathrm{K}}_X$ *is nonnegative*

$$\hat{\mathrm{K}}_X(\xi) \geq 0, \quad \xi \in \mathbb{R} \tag{5.36}$$

and symmetric

$$\hat{\mathrm{K}}_X(-\xi) = \hat{\mathrm{K}}_X(\xi), \quad \xi \in \mathbb{R} \tag{5.37}$$

Moreover, the Inverse Fourier Transform recovers K_X *in the sense that*

$$\mathrm{K}_X(\tau) = \int_{-\infty}^{\infty} \hat{\mathrm{K}}_X(\xi) e^{i2\pi\xi\tau} \mathrm{d}\xi, \quad \tau \in \mathbb{R} \tag{5.38}$$

The Fourier transform $\hat{K}_X$ is usually denoted as S_X, and it is called power spectral density. Thus, eq. (5.38) becomes

$$\mathrm{K}_X(\tau) = \int_{-\infty}^{\infty} S_X(\xi) e^{i2\pi\xi\tau} \mathrm{d}\xi, \quad \tau \in \mathbb{R} \tag{5.39}$$

and, we have

$$\mathrm{S}_X(\xi) = \int_{-\infty}^{\infty} K_X(\tau) e^{-i2\pi\xi\tau} \mathrm{d}\tau, \quad \xi \in \mathbb{R}. \tag{5.40}$$

Let us look at some examples.

Example 8. Let the random variable X be uniform distributed, i.e.,

$$X \sim \mathscr{U}(0, 2\pi)$$

and consider the following stochastic process

$$X_t = sin(t + X), \tag{5.41}$$

for all $t \in \mathbb{R}$. We have that

- $E[X_t] = 0, \quad \forall t \in \mathbb{R}$;
- $K_X(t_1, t_2) = \frac{1}{2\pi}\cos(t_1 - t_2)$, and;
- $Var[X_t] < \infty$.

Thus, it is a wide-sense stationary stochastic process. Defining the time lag $\tau = t_1 - t_2$, we have that the normalized autocovariance function is

$$\rho_X(\tau) = \cos(\tau). \tag{5.42}$$

This eq. (5.42) is represented in example 7, where we consider $\omega_0 = 1$. Thus, in the fig. 23(a) we have the autocovariance function, and in fig. 23(b), we have the the power spectral density S_X which is the Fourier transform of the autocovariance function, such that satisfies all properties of the theorem 5.3.1.

Example 9. Consider the example 3, fixing ω and getting one sample function for t, such that $t \in R$. The autocovariance function is

$$\rho_X(\tau) = \delta(\tau), \tag{5.43}$$

where the power spectral density is constant equals to 1. The fig. 24 we show more details of it.

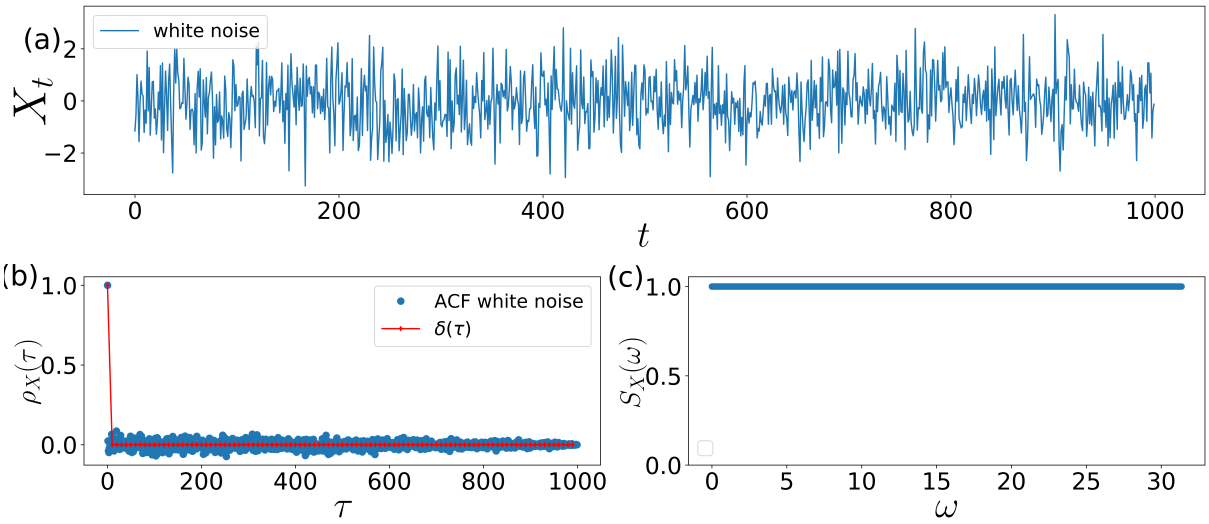

Figure 24 – (a) shows a sample function of the stochastic process given by eq. (5.13), (b) shows the autocovariance function of the process, where the blue points represent the "ACF white noise" and the red line fitting it is the Dirac delta represented by "$\delta(\tau)$". In (c), we have the power spectrum density, which is constant for this sort of stochastic process.

CHAPTER

6

INTERNAL FLUCTUATIONS

In this chapter, we aim at studying the behavior of the internal fluctuations caused by the effect of a small number of connections between neighbors of a large, sparse, homogeneous, and directed complex network.

6.1 Problem description

6.1.1 Network

We follow the same network structure from Toenjes, Masuda and Kori (2010), i.e., we consider a ring of N unidirectionally coupled nodes, i.e., for all $i \in [N]$ the node i is connected to the $i-1$ node (black arrows in fig. 25). So, we add N_{sc} unidirectional shortcuts with random origin j and destination i represented as the brown arrows in fig. 25. The parameter

$$\sigma = \frac{N_{sc}}{N} \tag{6.1}$$

is the density of the cross-connections in the network. Note that the number of edges in the network is given by

$$|E| = N + N_{sc}, \tag{6.2}$$

where

$$0 \leq N_{sc} \leq \frac{N^2 - 3N}{2}, \tag{6.3}$$

and

$$\langle k_{in,i} \rangle = 1 + \sigma. \tag{6.4}$$

The density of the network is

$$d = \frac{(1+\sigma)}{(N-1)}. \tag{6.5}$$

Then, for large number N such that $N_{sc} \ll N$ the network is sparse, i.e.,

$$0 < d \ll 1, \tag{6.6}$$

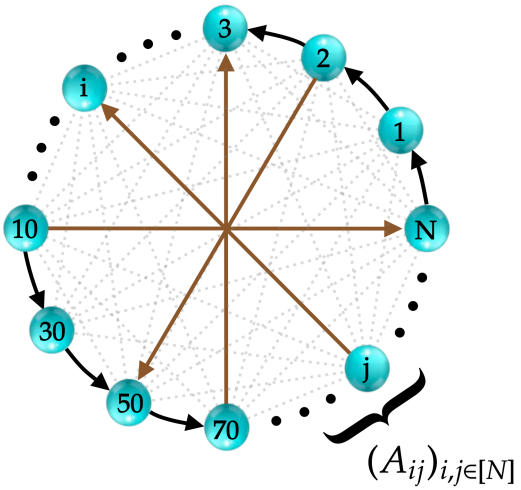

Figure 25 – Complex network structure where the black arrows are the connections of the ring, which has N fixed links and the brown ones are the shortcuts N_{sc}. The topology of the network could be encoded by the adjacency matrix A.

and the network becomes more sparse as $N \to \infty$.

6.1.2 Phase model

We consider the same phase model previously discussed in the subsection (4.3.1) of section (4.3):

$$\begin{cases} \dot{\theta}_i(t) = \omega_i + \dfrac{\varepsilon}{k_{in,i}} \displaystyle\sum_{j=1}^{N} A_{ij} \sin(\theta_j(t) - \theta_i(t) + \alpha), \quad \text{for all } i \in [N], \\ \theta_i(0) = \theta_{0i}, \end{cases} \tag{6.7}$$

where $N \in \mathbb{N}$ is the number of nodes in the network, $\theta_i \in \mathbb{T}$ are the phase variables, $\theta_i(0) = \theta_{0i}$ are the initial conditions, $0 < \varepsilon \ll 1$ is the coupling strength, $\alpha \in [0, \frac{\pi}{2})$ is the frustration parameter, and $k_{in,i}$ is the in-degree of the node i.

As metioned the rewrite the model is

$$\begin{cases} \dot{\vartheta}_i(t) = \dfrac{1}{k_{in,i}} \displaystyle\sum_{j=1}^{N} A_{ij} \sin(\vartheta_j(t) - \vartheta_i(t) + \alpha), \quad \text{for all } i \in [N], \\ \vartheta_i(0) = \vartheta_{0i}, \end{cases} \tag{6.8}$$

where overall synchrony is described by the order parameter

$$r(t) = \frac{1}{N} \left\| \sum_{j=1}^{N} e^{i\vartheta_j(t)} \right\|, \tag{6.9}$$

and in the fig. 19 of subsection (4.3.1) we saw the global behavior of the system with respect to the asymptotic behavior of the order parameter, observing the discontinuous transition.

6.1.3 Mean-field approach

Looking at fig. 25, the dynamics for each node i is influenced by the other ones. Then, it is reasonable to analyze the average contribution this node receives in its dynamics from all the rest. Thus, we introduce the macroscopic average G, such that for N large, this could be approximated to the spatial average, i.e.,

$$\begin{aligned} G(\vartheta_i(t),t,\alpha) &= \frac{1}{N}\sum_{i=1}^{N}\sin(\vartheta_j(t)-\vartheta_i(t)+\alpha), \\ &\approx \int_{-\pi}^{\pi}\sin(\vartheta'-\vartheta_i(t)+\alpha)\rho(\vartheta',t)d\vartheta', \end{aligned} \tag{6.10}$$

where ρ is probability density function and the last term denotes the mean-field approach. Another approach is with respect to the empirical distribution of the ϑ_i for $i = 1,2,\ldots,N$, such that considering a large number N it approximates to (e.g., see fig. 26)

$$\frac{1}{N}\sum_{i=1}^{N}\delta(\vartheta_i(t)-\vartheta) \approx \int_{-\pi}^{\vartheta}\rho(\vartheta',t)d\vartheta', \tag{6.11}$$

with

$$\int_{-\pi}^{+\pi}\rho(\vartheta',t)d\vartheta' = 1. \tag{6.12}$$

6.1.4 Fluctuation approach

We define fluctuations for each node i as

$$\eta_i^N(G,t,\alpha) = \sqrt{k_{in,i}}\left[\frac{1}{k_{in,i}}\sum_{j=1}^{N}A_{ij}\sin(\vartheta_j(t)-\vartheta_i(t)+\alpha) \;-\; G(\vartheta_i,t,\alpha)\right]. \tag{6.13}$$

in the next sections will be devoted to describe the behavior of such fluctuations.

6.1.5 Numerical observations about α

Recalling eq. (6.8), we know that

1. for $\alpha = \alpha' > \alpha_c$:

$$r(t) = \frac{1}{N}\left\|\sum_{j=1}^{N}te^{i\vartheta_j(t)}\right\| = 0, \tag{6.14}$$

after some transient time. Moreover, in the fig. 26, we note that empirical distributions for the set $\{\vartheta_1(t),\ldots,\vartheta_N(t)\}$ of solutions, for some time unities, seemed to converge to a uniform distribution.

This apparently implies that the probability density function seems to be stationary, where it is confirmed from computations in Strogatz (2000). Thus, when $r = 0$ the phase oscillators are uniformed distributed in the unit circle with

$$\rho(\vartheta) = \frac{1}{2\pi}, \tag{6.15}$$

implying that

$$G\left(\vartheta_i,t,\alpha'\right) \approx \frac{1}{2\pi}\int_{-\pi}^{+\pi} \sin\left(\vartheta'(t)-\vartheta_i(t)+\alpha'\right) d\vartheta' = 0 \tag{6.16}$$

and

$$\eta_i^N\left(0,t,\alpha'\right) = \sqrt{k_{in,i}}\left[\frac{1}{k_{in,i}}\sum_{j=1}^{N} A_{ij}\sin\left(\vartheta_j(t)-\vartheta_i(t)+\alpha'\right)\right]; \tag{6.17}$$

2. for $\alpha = \alpha' < \alpha_c$ and $t \to \infty$:

$$r_\infty = 1. \tag{6.18}$$

Thereby, there is a $\vartheta \in \mathbb{T}$, such that as $t \to \infty$, $\vartheta_i(t) = \vartheta(t), \forall i \in [N]$ and it makes sense to think that the probability density function ρ is a delta, i.e.,

$$G\left(\vartheta,t\to\infty,\alpha'\right) \approx \int_{-\pi}^{+\pi} \sin\left(\vartheta'(t)-\vartheta(t)+\alpha'\right)\delta(\vartheta'(t)-\vartheta(t)) = \sin\left(\alpha'\right). \tag{6.19}$$

Then

$$\eta_i^N\left(G,t_\infty,\alpha'\right) = 0. \tag{6.20}$$

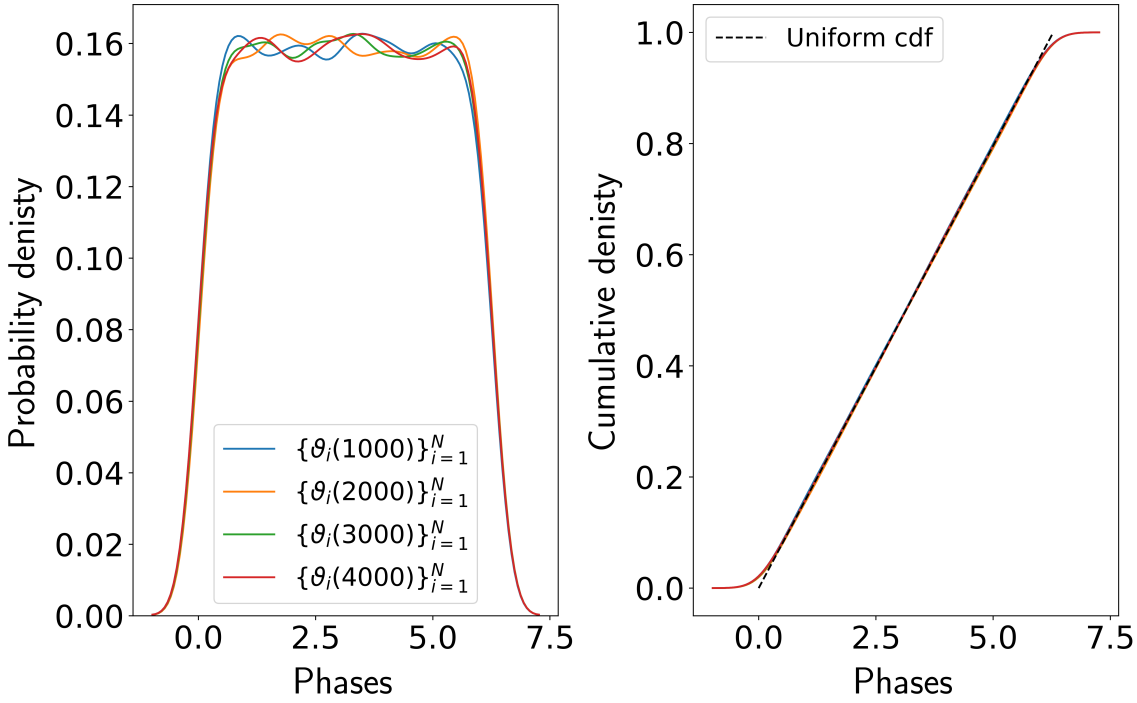

Figure 26 – Histogram for the set $\{\vartheta_i(t)\}_{i=1}^N$ of phases in different times together with the cumulative histogram in the right-hand-side. For this simulation we consider $N = 7000$, $\sigma = 200$, and $\alpha = 1.57$. For each time unity labeled in the figure, we plot the histogram of the phases. Note that the cumulative histogram of the phases seems to converge to the uniform cdf represented by the dashed black line.

In the figure fig. 27, we simulate the fluctuations for $\alpha > \alpha_c$. For that, we integrate the system considering n time-steps, such that for every step, the system is integrated 10 times before

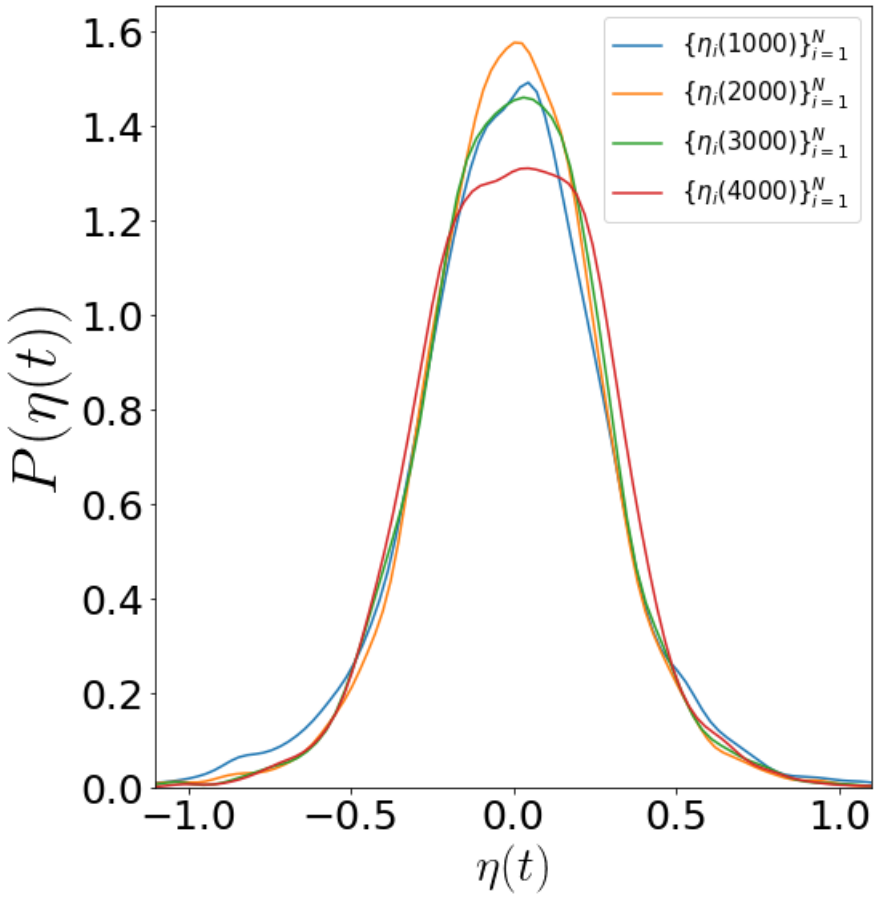

Figure 27 – Histogram for the set $\{\eta_i^N(0,t,\alpha')\}_{i=1}^N$ with $N = 7000$, $\sigma = 200$, and $\alpha = 1.57$. The phases started uniformly distributed in $(0,2\pi)$ and for different time unities labeled in the figure we compute the fluctuations from eq. (6.17).

to go to the next one. Then, the total integration steps is $n*10$ and the size of the time-step is $dt = 0.01$. Note that fluctuations seem to be normally distributed with the same mean and variance.

6.1.6 Autocovariance function of the fluctuations for $\alpha > \alpha_c$

Numerically, we have already analyzed the autocovariance function of the fluctuations with respect to the time in the fig. 28(b). For that, we consider a partition of the time, such that for the process $\{\eta_i(t_j)\}_{j=1}^n$ we define the autocovariance function as

$$\rho_i(\tau) = \frac{E\left[\left(\eta_i(t_{j+\tau}) - \mu_i'(t_{j+\tau})\right)\left(\eta_i(t_j) - \mu_i'(t_j)\right)\right]}{\sigma_i'^2}, \tag{6.21}$$

where we use the results from chapter 5 to plot the power spectral density S of the autocovariance function in the fig. 28(c).

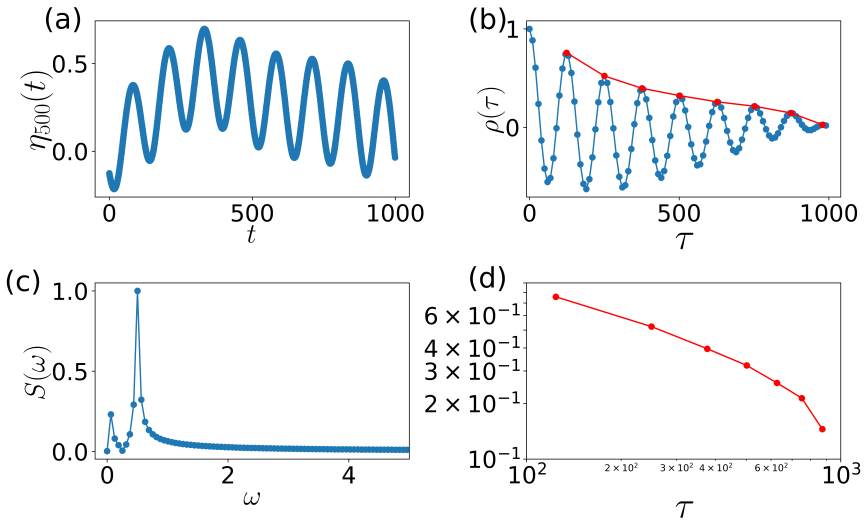

Figure 28 – Panel (a) shows a sample function of the process $\{\eta_i(t_j)\}_{j=1}^{n}$ for $i = 500$, in the panel (b) we have the autocovariance function of (a) running overtime τ, the panel (c) is the power spectrum density considering the autocovariance function in (b), and in the last panel (d), we plot the log-log scale of the red curve outlining the extremes of the autocovariance function. For all simulations of this figure, we consider $N = 7000$, $\sigma = 200$, $\alpha = 1.57$, and we take just the last 1000 units of time of the simulation.

CHAPTER

7

SYNCHRONIZATION OF COUPLED CHAOTIC CIRCLE MAPS

This chapter focuses on studying synchronization in dense random networks using mean-field equations. The research reveals the presence of chaotic transients before synchronization, with the incoherent state persisting for extended periods. The study explores the statistics and scaling behavior of transient times and uncovers a dependence on the link probability. The delayed transition to synchrony challenges mean field theory and raises questions about the dynamics of similar systems.

7.1 Model

The local phase dynamics within each node of the network are described by a Bernoulli map of the circle, where the time steps $t \in \mathbb{Z}$ are governed by the equation:

$$\varphi(t+1) = f(\varphi(t)) = 2\varphi(t) \mod 2\pi, \tag{7.1}$$

Alternatively, we can express this dynamics on the complex unit circle using the notation $z = \exp(i\varphi)$, resulting in the equation $z(t+1) = f(z(t)) = z(t)^2$. This Bernoulli map is known for its chaotic behavior and structural stability, as observed in previous studies (TANZI; PEREIRA; STRIEN, 2019). Structural stability implies that the statistical properties of the map persist even under small perturbations. Consequently, when the coupling between nodes is weak, the individual maps behave nearly independently, leading to the absence of collective dynamics in the network.

Due to the structural stability of the Bernoulli map, for small coupling strengths, the individual maps in the network behave almost independently. In other words, the interaction between oscillators is weak, and there is limited influence of neighboring oscillators on each other. Consequently, the system does not exhibit significant collective dynamics under small

coupling. The lack of synchronization in this regime can be attributed to the near-independence of the individual phase dynamics, which prevents any coherent alignment or coordination of the oscillators. It is only when the coupling strength exceeds a certain threshold that the system transitions to a synchronized state, where the individual oscillators become more strongly coupled, and their collective dynamics start to emerge.

The behavior of the Bernoulli maps as nearly independent entities for small coupling serves as a foundation for understanding the absence of collective behavior in this regime, providing insight into the onset of synchronization when the coupling strength surpasses a critical value. This understanding is crucial for studying synchronization transitions in complex networks and elucidating the conditions under which synchronization emerges in the networked system. By exploring the interplay between the chaotic dynamics of individual oscillators and their collective behavior, researchers can gain valuable insights into the mechanisms driving synchronization transitions and the role of network topology, coupling strength, and other factors in shaping the emergent dynamics of complex systems.

7.2 Moebius map

In the study conducted by Gong et al. (GONG; TOENJES; PIKOVSKY,), the global coupling of the phase dynamics is realized using a Moebius map on the complex unit circle. The Moebius map has been proven to provide exact solutions for sinusoidally forced phase dynamics (Marvel; Mirollo; Strogatz,), including models such as the Kuramoto model, Winfree-type phase equations, and even the dynamics of theta neurons through a nonlinear transformation (MONTBRIÓ; PAZÓ; ROXIN,). Thus, it serves as a meaningful alternative to the sine coupling commonly used in the standard circle map. In this work, we adopt a composition of Equation 7.1 and a Moebius map, as illustrated in Figure 29:

$$z(t+1) = M\left(f(z(t)), \Phi(t), \tau(t)\right), \tag{7.2}$$

where

$$M(w, \Phi, \tau) = \frac{e^{i\Phi}\tau + w}{1 + e^{-i\Phi}\tau w}, \tag{7.3}$$

with a coupling intensity $-1 < \tau < 1$, an angle of contraction $\Phi \in \mathbb{S}^1$, and a point $w \in \mathbb{D} = \{z \in \mathbb{C} : |z| < 1\}$ within the open complex unit disk. The family of Moebius maps represents a group of biholomorphic automorphisms of $\mathbb{D}$, and through analytic continuation, these transformations bijectively map the boundary of $\mathbb{D}$ onto itself. The effect of Equation 7.3 on the unit disk is a contraction of almost all points towards $\exp(i\Phi)$ on the boundary. Specifically, as τ approaches ± 1, we have $\lim_{\tau \to \pm 1} M(w, \Phi, \tau) = \pm \exp(i\Phi)$, and as τ approaches 0 we have $\lim_{\tau \to 0} M(w, \Phi, \tau) = w$. The parameter τ characterizes the strength of the contraction, and as τ tends to 0, the map described by Equation 7.2 approximates the uncoupled dynamics given by Equation 7.1.

This incorporation of the Moebius map in the model enriches our understanding of synchronization transitions in complex networks. By introducing a coupling mechanism that induces a contraction towards a specific point on the boundary of the unit disk, we can investigate how the strength of this contraction affects the emergence and properties of synchronization. Moreover, the ability of the Moebius map to accurately capture various types of forced phase dynamics makes it a versatile tool for studying synchronization in different systems. Therefore, the utilization of Equation 7.2 provides a valuable framework for exploring synchronization transitions and their underlying mechanisms in complex networks.

7.3 Mean-field as Moebius map dynamics

The family of wrapped Cauchy distributions given by

$$p(\varphi) = \frac{1}{2\pi} \frac{1 - R^2}{|1 - Re^{i(\varphi - \Theta)}|^2} \tag{7.4}$$

is a continuous phase measure that includes both incoherence as the uniform distribution when $R \to 0$ and a delta distribution at $\varphi = \Theta$ when $R \to 1$, is invariant under (7.2) and (7.3) (GONG; TOENJES; PIKOVSKY, ; Marvel; Mirollo; Strogatz, ; PIKOVSKY,). This family of continuous phase measures, in the context of phase synchronization, is known as the Ott-Antonsen manifold, and assuming this form of phase distribution is equivalent to the so called Ott-Antonsen ansatz (OTT; ANTONSEN, b; OTT; ANTONSEN, a). The Ott-Antonsen manifold is parameterized using the mean-field amplitude R and the mean-field angle Θ

$$Z = Re^{i\Theta} = \int_0^{2\pi} e^{i\varphi} p(\varphi)\, d\varphi. \tag{7.5}$$

The mean-field amplitude R is the Kuramoto order parameter (KURAMOTO,), which is zero for incoherence, i.e., a uniform phase distribution, and $R = 1$ for complete synchronization $\varphi_n = \Theta$ (a.s.). Furthermore, the higher circular moments Z_q on the Ott-Antonsen manifold with $q \in \mathbb{Z}$ are integer powers of the mean field

$$Z_q = \int_0^{2\pi} e^{iq\varphi} p(\varphi)\, d\varphi = Z^q. \tag{7.6}$$

As a consequence, phase doubling maps the circular moments as $f(Z_q(t)) = Z_{2q}(t) = Z_2^q(t) = f(Z_1(t))^q$, leaving the Ott-Antonsen manifold invariant and mapping the mean-field amplitude and phase as $R \to R^2$ and $\Theta \to 2\Theta$.

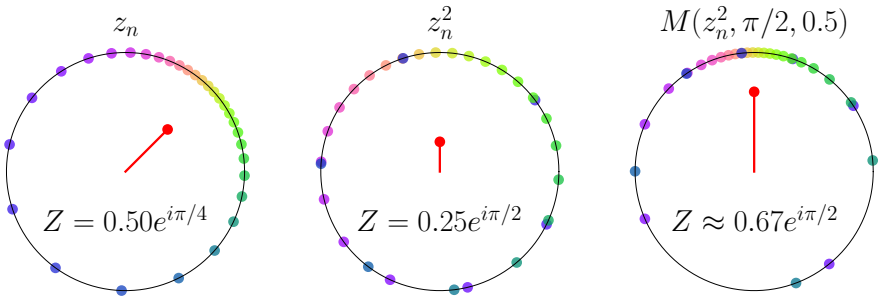

Figure 29 – Dynamics of phases. $N = 30$ points on the complex unit circle colored by phase, and corresponding mean field (red dot inside the unit circle). From left to right : initial phase configuration at the points z_n with mean-field amplitude $R = 0.5$ and mean-field phase $\Theta = \pi/4$, after chaotic phase doubling z_n^2 with $R^2 = 0.25$ and $2\Theta = \pi/2$, and after subsequent contraction toward the angle $\pi/2$ with intensity $\tau = 0.5$. Figure from: Mendonca, Tönjes and Pereira ()

In order to couple the dynamics of the Bernoulli maps given by Equation (7.2), we need to define the parameters $\Phi(t)$ and $\tau(t)$ in Equation (7.3) as functions of the ensemble mean field. Building upon the work of Gong et al. (GONG; TOENJES; PIKOVSKY,), we define the contraction angle $\Phi(t)$ and the coupling intensity $\tau(t)$ as follows:

$$Z(t) = \frac{1}{N}\sum_{n=1}^{N} z_n(t) = R(t)e^{i\Theta(t)} \tag{7.7}$$

$$\Phi(t) = 2\Theta(t) \tag{7.8}$$

$$\tau(t) = \tanh\left(\frac{\varepsilon}{2}R(t)\right). \tag{7.9}$$

Here, ε represents the coupling strength. When $\tau = 1$, corresponding to $\varepsilon R \to \infty$, the phases undergo contraction towards a single point $\exp(2i\Theta)$ on the unit circle. Conversely, for small values of εR, we can linearize Equation (7.2) and obtain the well-known form of mean-field coupled circle maps with phase doubling

$$\varphi_n(t+1) = 2\varphi_n(t) + \varepsilon R(t)\sin(2\Theta(t) - 2\varphi_n(t)) + O(\varepsilon^2 R^2(t)). \tag{7.10}$$

The crucial observation is that on the Ott-Antonsen manifold, the mean-field $Z = R\exp(i\Theta)$ transforms exactly the same way via (7.2),(7.3) as each element $z = \exp(i\varphi)$ on the unit circle (Marvel; Mirollo; Strogatz, ; GONG; TOENJES; PIKOVSKY,); that is,

$$Z(t+1) = M(Z^2(t), \Phi(t), \tau(t)). \tag{7.11}$$

The derivation of a closed analytic expression for the dynamics of the mean field in coupled nonlinear systems is highly unusual and provides valuable insights. This reduction from infinitely dimensional microscopic dynamics to low-dimensional mean-field dynamics has proven to be remarkably successful in analyzing synchronization phenomena over the last decade (OTT; ANTONSEN, b). However, understanding the effects of finite system size N remains

challenging (PETER; PIKOVSKY, ; PETER; GONG; PIKOVSKY,). It is important to note that while a finite ensemble of phases may not precisely lie on the Ott-Antonsen manifold, it can, in some sense, be arbitrarily close to the so-called thermodynamic limit, i.e., the limit of the infinite system size $N \to \infty$.

The application of the Ott-Antonsen ansatz to networks of phase oscillators is feasible when the network structure allows for the grouping of vertices into a few classes of equivalent nodes. By assuming that all vertices within a class are subject to the same sinusoidal forcing, the dynamics of the phase oscillators can be effectively reduced to coupled mean-field dynamics on the Ott-Antonsen manifold for each vertex class (SKARDAL; RESTREPO, ; MARTENS, ; OTTINO-LÖFFLER; STROGATZ, ; MARTENS; PANAGGIO; ABRAMS, ; TÖNJES; FIORE; PEREIRA,). Furthermore, incorporating oscillator heterogeneity and force fluctuations into the mean field dynamics is possible by considering Cauchy distributions (LAING, ; TÖNJES; PIKOVSKY, ; CLUSELLA; MONTBRIÓ,).

7.3.1 Mean-Field Analysis

The mean-field dynamics (7.11) can be expressed in polar form as

$$\Theta(t+1) = f(\Theta(t)) \quad \text{and} \quad R(t+1) = \frac{\tau(t) + R^2(t)}{1 + \tau(t) R^2(t)}. \tag{7.12}$$

This decouples the dynamics of the phase Θ, which evolves chaotically, from the dynamics of the amplitude R. By substituting equations (7.9) and (7.12), we obtain the exact evolution of the order parameter R in a closed form:

$$R(t+1) = \frac{\tanh\left(\frac{1}{2}\varepsilon R(t)\right) + R^2(t)}{1 + \tanh\left(\frac{1}{2}\varepsilon R(t)\right) R^2(t)}. \tag{7.13}$$

Equation (7.13) allows us to determine the fixed points of the mean-field amplitude $R(t)$ and analyze their linear stability. The system exhibits two fixed points: complete synchronization at $R = 1$ and complete desynchronization at $R = 0$. The stability of these fixed points changes at unique critical points: $\varepsilon_1 = \ln(2) \approx 0.69$ and $\varepsilon_0 = 2$. The stability is determined by the eigenvalues of the Jacobian of equation (7.13) evaluated at these fixed points. There exists an unstable fixed point branch $(\varepsilon(R_u), R_u)$ connecting these critical points, given by

$$\varepsilon(R_u) = \frac{1}{R_u} \log\left(\frac{(1+R_u)^2}{1+R_u^2}\right). \tag{7.14}$$

This expression is derived by setting $R(t+1) = R(t) = R_u$ in equation (7.13) and solving for ε. Consequently, the system of all-to-all coupled, identical chaotic phase maps will evolve towards either complete synchronization or complete desynchronization, with a small region of bistability $\ln(2) < \varepsilon < 2$ (Figure 30a).

7.4 Extension to Networks

In the next phase of our research, we delve into the dynamics of phase synchronization on a random network composed of N maps, with each map connected to precisely k random neighbors. The local mean field, denoted by $Q_n = R_n e^{i\Theta_n}$, is defined as the average coupling effect of neighboring maps on map n. We employ an adjacency matrix to determine the connections between nodes in the network. The phase dynamics on the network are then governed by a mathematical expression involving the local mean field and the maps' phases.

To classify networks as dense, we examine the ratio of the average node degree $\langle k \rangle$ to the system size N, denoted as p. In the context of finite networks, we consider a network to be dense when, on average, nodes have more than one neighbor. For large dense networks, the local mean fields of oscillators in each node's neighborhood closely resemble the global mean field, with a deviation proportional to $1/\sqrt{k}$. Consequently, mean-field theory is a reliable framework for describing dense networks in the thermodynamic limit.

For our simulations, we adopt a random network model where each node is connected to exactly k random neighbors. Although this model assumes a uniform in-degree of k for each node, it slightly differs from the Erdős-Rényi model with a Poissonian in-degree distribution. Nevertheless, for large values of k, the simulation results obtained using our random network model align closely with those of other random networks, exhibiting uncorrelated node degrees and a negligible degree distribution width.

By utilizing this network model, we can directly compare the simulation outcomes with our mean-field analysis, thereby gaining valuable insights into the dynamics of synchronization in dense networks.

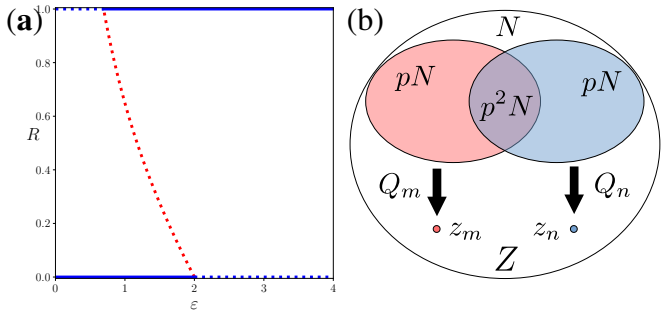

Figure 30 – Bifurcation diagram of the mean-field amplitude and a representation of the network interaction. In (**a**), the bifurcation diagram of the all-to-all coupling mean-field dynamics (7.12), i.e., on the Ott-Antonsen manifold. Dotted lines show linearly unstable fixed points and solid lines show linearly stable fixed points in the thermodynamic limit. (**b**) Venn diagram of a dense network with N vertices and connection probability p. The sets of neighbors of nodes m and n are of size pN and their overlap is of size p^2N, resulting in correlated local mean fields $Q_m = R_m \exp(i\Theta_m)$ and $Q_n = R_n \exp(i\Theta_n)$ acting on the states z_m and z_n. The ratio of the amplitudes of the local mean fields and the global mean field are independent of the network size N. Figure from: Mendonca, Tönjes and Pereira ()

7.5 Results and Conclusions

7.5.1 Distributions of Transient Times

We perform a large number M of simulations $m = 1 \ldots M$ from independent, uniformly distributed random initial phases over a maximum of T steps and record in each simulation the first time step t_m when $R \geq 0.5$, i.e., the transition time from an incoherent state to complete synchronization. Finite-size scaling for such a discontinuous transition is challenging (OLIVEIRA; LUZ; FIORE,). The exponential distribution of the times t_m, according to some characteristic transition rate, can be checked in a rank plot of time points t_m, which gives the sample complementary cumulative distribution $C(t) = \text{prob}(t \geq t_m) = \text{rank}(t_m)/M$ (Figure 32a,d).

An exponential tail distribution $C(t)$ up to observation time T indicates an exponential distribution of transient times. Since the simulation time is finite, transition times $t_m \geq T$ are not observed, which represents a problem when we are interested in the average time to synchronization. However, assuming a discrete exponential, i.e., geometric distribution, a maximum likelihood estimation of the average transition time is possible up to values considerably exceeding the observation time T (see Appendix **??**).

Denoting the number of simulations that synchronize at times $t_m < T$ as M_T, and defining the observable values $l_m = \min(t_m, T)$, the maximum likelihood estimation of the expected value $T_{esc} = \text{E}[t_m]$ for the geometric distribution is

$$T_{esc} = \frac{\langle l_m \rangle M}{M_T}. \tag{7.15}$$

with the sample mean $\langle l_m \rangle$. If the transition to synchronization is observed in all simulations, i.e., $M_T = M$, the estimator is simply the sample mean of t_m, which is an estimator of T_{esc} for arbitrary transient time distributions. However, when most runs do not synchronize within the finite simulation time T, the ratio M/M_T contains additional information, and the estimated mean escape time can be much larger than the observation time.

7.5.2 During Coexistence: Escape over the Unstable Branch

In (LUCCIOLI *et al.*,), it was reported that the transition from incoherence to collective dynamics in sparse networks of coupled logistic maps is of the mean-field type. The analysis in (RESTREPO; OTT; HUNT,) predicts a shift in the critical coupling strength in random networks of Kuramoto phase oscillators of the order $\langle k \rangle^2 / \langle k^2 \rangle$ due to degree inhomogeneity, and $1/\langle k \rangle$ due to finite size fluctuations of the local mean fields. That is, in dense, homogeneous networks with $\langle k \rangle^2 / \langle k^2 \rangle \to 1$ and $\langle k \rangle \to \infty$, the critical coupling strength does not change. We expected to find similar behaviors for network-coupled Bernoulli maps. In complete or almost complete networks $k/N = p \approx 1$ for $\varepsilon < 2$, there is a small probability that finite size fluctuations bring the order parameter R above the unstable branch, leading to a spontaneous transition to

complete synchronization, as shown in Figure 31a. We first observe the scaling of the transient time in fully connected networks with $p = 1$. For values of $\varepsilon < \varepsilon_0 = 2.0$, the transition rate to synchronization scales strongly with the size N of the system (Figure 32b,c). However, for values $\varepsilon > \varepsilon_0$, the average transition time depends very weakly on N, as the system grows exponentially fast from a state of incoherence, with $R \approx 1/\sqrt{N}$. We estimate a finite size scaling exponent β that is below the transition threshold by collapsing the curves $T_{esc}(\varepsilon, N)$ using the ansatz $T_{esc}(\varepsilon, N) = T_{esc}\left((\varepsilon - \varepsilon_0)N^{\beta}\right)$. The data are consistent with an ad hoc exponent of $\beta = 1/3$ (Figure 32c).

7.5.3 Above the Critical Coupling Strength: Long Chaotic Transient

Above the critical coupling strength $\varepsilon > \varepsilon_0 = 2$, we expected finite size fluctuations to grow exponentially fast and independently of N, as predicted by linear stability analysis of the mean-field equations (7.13). Instead, for small connection probabilities $0 < p < 1$, we have observed a chaotic transient with seemingly stationary finite size fluctuations $O(1/\sqrt{N})$ of the mean field (Figure 31). In the large N limit, the distribution of the transient times depends on the link density p with increasingly long transients as p is decreased, but it is otherwise independent of N.

A coupling strength for which a transition to complete synchronization could still be observed within the simulation time was considerably larger than the mean-field critical coupling $\varepsilon_0 = 2$. That is, even in dense networks and above the mean-field critical coupling, finite size fluctuations will not necessarily result in the nucleation and exponential growth of a collective mode. Such a delayed transition to synchronization (BAER; ERNEUX; RINZEL,) has so far not been described in systems of coupled phase oscillators (ICHINOMIYA, ; RESTREPO; OTT; HUNT, ; KO; ERMENTROUT,) or coupled logistic maps (LUCCIOLI *et al.*,).

In Figure 32f, we plot T_{esc} over $(\varepsilon - \varepsilon_0)p$ to demonstrate that the average transition time is roughly scaling as $1/p$. We do not look for higher-order corrections such as a weak dependence of ε_0 on p, although the curves do not collapse perfectly. Note that the escape time is largely independent of the network size (Figure 32e,f). For $p = 0.1$, 0.05, and 0.025 we have performed simulations with $N = 10^4$ (circles) and with $N = 5 \times 10^4$ (crosses) for comparison. For $p = 0.01$, we compare network sizes $N = 10^4$ (circles) with very time-consuming simulations in networks with $N = 10^5$ (crosses).

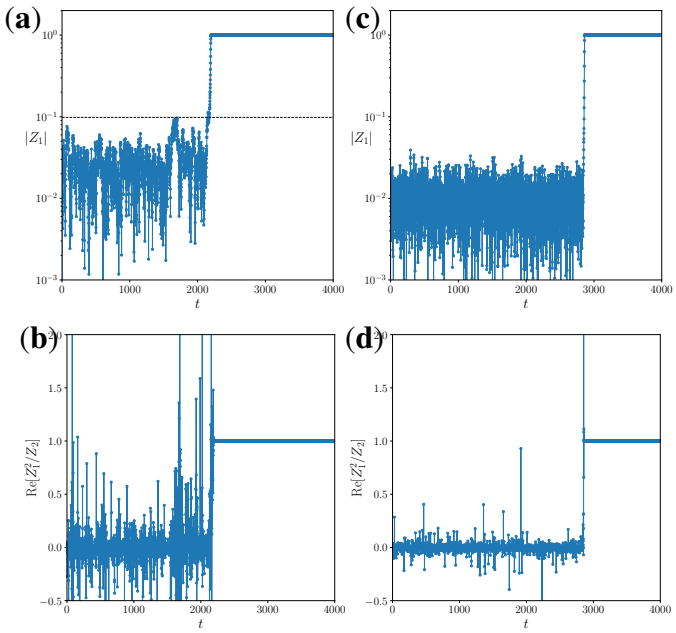

Figure 31 – Transient to synchronization for $N = 10{,}000$ coupled maps in (**a**,**b**), a fully connected network with coupling strength $\varepsilon = 1.81$ below the critical coupling $\varepsilon_0 = 2$, and (**c**,**d**), in a random network with connection probability $p = 0.1$ for a coupling strength of $\varepsilon = 2.3$ above the critical coupling. The upper panels (**a**,**c**) show the order parameter $R(t)$, and the lower panels (**b**,**d**), the real part of the ratio of the first two circular moments $\mathrm{Re}[Z_1^2/Z_2]$. This serves as a visual measure of the alignment of the system state with the Ott-Antonsen manifold, where the ratio is exactly equal to one. The dashed line in (**a**) marks the value of the unstable fixed point of the mean-field dynamics, $R_u = 0.098$. Above that value, the state of complete synchronization is attractive on the Ott-Antonsen manifold. In (**b**,**d**), the incoherent state $R = 0$ is unstable; however, finite size fluctuations do not grow exponentially. Instead, we observe a long chaotic transient. Figure from: Mendonca, Tönjes and Pereira ()

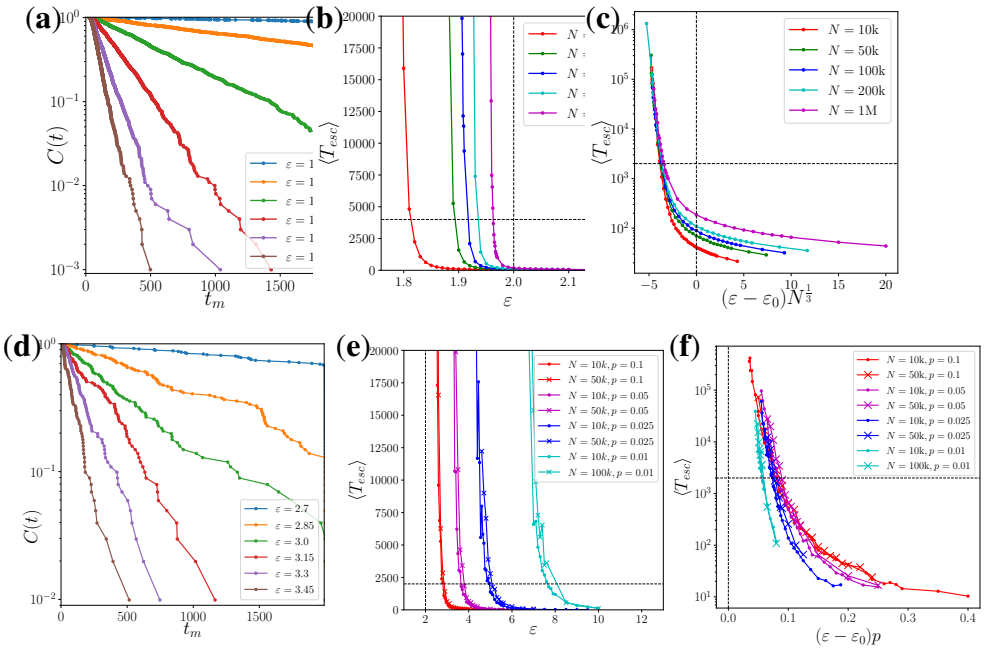

Figure 32 – Statistics of transient times t_m to synchronization. (**a**–**c**) In the fully connected network; (**d**–**f**) in random networks of various link densities $p = k/N$. The upper panels show straight lines in semi-logarithmic plots of cumulative tail distributions of the transient times, demonstrating the rate character of the transition process. The middle panels show the estimated average transient times for various combinations of system sizes N, coupling strengths ε, and link densities p. The mean field critical coupling strength $\varepsilon_0 = 2.0$ and the maximum observation time T are marked by dashed lines. In the globally coupled system on the left-hand side, the transient time depends strongly on the system size N, whereas in dense networks and above ε_0, the transient time depends strongly on the link density $p = k/N$, but not on the system size. We demonstrate the scaling of the transition times in the lower panels. In the globally coupled system, the exponential divergence of the transient times below ε_0 appears to be a function of $(\varepsilon - \varepsilon_0)N^{\frac{1}{3}}$. In dense networks, the exponential divergence is roughly a function of $(\varepsilon - \varepsilon_0)p$. Figure from: Mendonca, Tönjes and Pereira ()

7.5.4 Discussion of Finite Size Scaling

Mean field theory assumes a phase distribution on the Ott-Antonsen manifold. The characteristic function of a wrapped Cauchy distribution is the geometric sequence $Z_q = Z^q$ of circular moments (7.6). However, in the incoherent state with N independent uniformly distributed phases φ_n the circular moments of an ensemble

$$Z_q = \frac{1}{N} \sum_{n=1}^{N} e^{iq\varphi_n} \tag{7.16}$$

are almost independent complex numbers with a Gaussian distribution of mean zero and a variance of $1/N$ by virtue of the central limit theorem. The action of the Bernoulli map on the circular moments is the shift

$$Z_q \to Z_{2q}, \tag{7.17}$$

that is, it is achieved by discarding all odd circular moments. The exponential growth of the order parameter in accordance to mean field theory is expected after the distribution comes close to the

Ott-Antonsen manifold, i.e., when the first few circular moments align by chance sufficiently under the mapping (7.17); in particular, $Z_2(t) \approx Z_1^2(t)$. Unless the directions of Z_2 and Z_1^2 align by chance, as they would on the Ott-Antonsen manifold, the subsequent contraction of strength εR in the direction of Z_1^2 after the phase doubling may even decrease the amplitude of the order parameter. In addition, for coupling strengths ε below the critical value, $R = |Z_1|$ must be above the unstable branch $R > R_u(\varepsilon) \sim (\varepsilon_0 - \varepsilon)$.

The rate of such a random event should depend on the ratio between $R_u(\varepsilon)$ and the standard deviation $1/\sqrt{N}$ of the Gaussian distribution of the complex mean field. Based on this scaling argument, the expected time to synchronize should scale as $T_{esc} = T_{esc}((\varepsilon - \varepsilon_0)\sqrt{N})$ below the critical coupling. The best collapse of the estimated escape times in fully connected networks of coupled Bernoulli maps was observed by scaling the distance to ε_0 with $N^{1/3}$ (Figure 31c), i.e., the exponential divergence of the escape time approaches ε_0 slower than $1/\sqrt{N}$ in the thermodynamic limit. One possibility for this discrepancy is that the scaling argument only considers the chance of $R > R_u$ and not the alignment process of the higher-order circular moments.

Above the critical coupling strength, there is only the condition of the alignment of circular moments with the Ott-Antonsen manifold for the initiation of exponential growth. Since in the incoherent state, all circular moments are random Gaussian with identical variance, the alignment process (7.17) is strictly independent of the system size N. Once exponential growth in the direction of the Ott-Antonsen manifold occurs, the time to synchronization is logarithmic, that is, it is weakly dependent on N. However, it appears that the alignment with the Ott-Antonsen manifold needs to be stronger for networks with link densities of $p < 1$. For small link densities, the divergence of the escape time occurs at larger values $\varepsilon > \varepsilon_0$. This is reminiscent of stabilization by noise (KHASMINSKII,), where a system is driven away from a low-dimensional unstable manifold of a fixed point into stronger attracting stable directions.

In simulations of dense random networks of coupled Bernoulli maps, we could see the independence of the mean escape time from the network size and the scaling of the escape time with roughly $\sim 1/p$. To explain this scaling, we argue that mean field theory might be extended to dense networks, where each node couples to a finite neighborhood of pN nodes in the network, and for every two nodes, these neighborhoods overlap on a set of size p^2N (Figure 30b). The local mean fields are Gaussian random forces of mean value Z, variance $1/k = 1/pN$, and the pairwise correlation of p, which is the relative size of the overlap. The decrease in correlation between the local mean fields in networks with link densities $p < 1$ can be interpreted as individual, finite size noise on the maps, which couples to the global mean field, plus some uncorrelated random deviation. Therefore, the contractions of the phases do not occur in the same direction for different nodes in the network. The strength of the contraction in the direction

of the mean field is effectively reduced by the factor p, i.e.,

$$\tau = \tanh\left(\frac{1}{2}\varepsilon R\right) p \approx \frac{1}{2}\varepsilon p R \tag{7.18}$$

shifting the coupling strength dependence of the transition time (above ε_0) by a factor of $1/p$.

7.5.5 Conclusions

We have investigated the synchronization of coupled chaotic maps in dense random networks, utilizing mean-field equations and examining network configurations with different link probabilities. Firstly, we noticed the existence of chaotic transients to synchronization within these networks. This means that the incoherent state can persist for extended periods before transitioning into synchronization. This finding led us to study the statistics of transient times and their scaling behaviors in the process of synchronization. The transition times follow exponential distributions, indicating spontaneous transitions at a constant rate. It is noteworthy that the transition from incoherence to complete synchronization only occurs spontaneously in networks of finite size. Additionally, we have observed a remarkable dependence of the transient times to synchronization on the link probability p, represented by the ratio of the in-degree to the total number of nodes, at coupling strengths where an immediate transition to synchrony would be expected from mean field theory. Whether such a delayed transition is due to the specifics of our model or is typical for a more general class of dynamics remains an open question.

BIBLIOGRAPHY

BAER, S. M.; ERNEUX, T.; RINZEL, J. The slow passage through a hopf bifurcation: Delay, memory effects, and resonance. v. 49, n. 1, p. 55–71. Available: <https://doi.org/10.1137/0149003>. Citation on page 76.

BARABáSI, A.-L.; ALBERT, R. Emergence of scaling in random networks. **Science**, v. 286, n. 5439, p. 509–, Oct. 1999. Available: <http://science.sciencemag.org/content/286/5439/509.abstract>. Citation on page 38.

BARABáSI, A.-L.; PóSFAI, M. **Network science**. Cambridge: Cambridge University Press, 2016. Citation on page 41.

BRODER, A.; KUMAR, R.; MAGHOUL, F.; RAGHAVAN, P.; RAJAGOPALAN, S.; STATA, R.; TOMKINS, A.; WIENER, J. Graph structure in the web. **Computer Networks**, v. 33, n. 1, p. 309 – 320, 2000. ISSN 1389-1286. Available: <http://www.sciencedirect.com/science/article/pii/S1389128600000839>. Citations on pages 33 and 38.

CLUSELLA, P.; MONTBRIÓ, E. Regular and sparse neuronal synchronization are described by identical mean field dynamics. Citation on page 73.

ELDERING, J. **Normally Hyperbolic Invariant Manifolds: The Noncompact Case**. [S.l.]: Atlantis Press, 2013. Citations on pages 9, 29, and 30.

ERDöS, P.; RéNYI, A. On random graphs i. **Publicationes Mathematicae Debrecen**, v. 6, p. 290, 1959. Citation on page 36.

ESTRADA, E.; KNIGHT, P. A. **A First Course in Network Theory**. [S.l.]: Oxford university press, 2015. Citation on page 40.

FENICHEL, N.; MOSER, J. K. Persistence and smoothness of invariant manifolds for flows. **Indiana University Mathematics Journal**, Indiana University Mathematics Department, v. 21, n. 3, p. 193–226, 1971. ISSN 00222518, 19435258. Citations on pages 29 and 30.

GONG, C. C.; TOENJES, R.; PIKOVSKY, A. Coupled Möbius maps as a tool to model Kuramoto phase synchronization. APS, v. 102, n. 2, p. 022206. Citations on pages 18, 70, 71, and 72.

GUCKENHEIMER, J.; HOLMES, P. J. **Nonlinear Oscillations, Dynamical Systems, and Bifurcations of Vector Fields**. New York: Springer-Verlag, 1983. Citation on page 27.

GUILLEMIN, V.; POLLACK, A. **Differential Topology**. [S.l.]: American Mathematical Society, 2011. Citation on page 29.

HAGOS, Z. G. **Reconstruction of phase dynamics from data**. Bachelor's Thesis (Doutorado) — Instituto de Ciências Matemáticas e de Computação, São Carlos, 2019. Citation on page 31.

HIRSCH, M. W.; PUGH, C. C.; SHUB, M. **Invariant Manifolds**. Berlin: Springer-Verlag, 1977. Citations on pages 29 and 30.

HOPPENSTEADT, F. C.; IZHIKEVICH, E. M. **Weakly Connected Neural Networks**. New York: Springer-Verlag, 1997. Citation on page 29.

ICHINOMIYA, T. Frequency synchronization in a random oscillator network. APS, v. 70, n. 2, p. 026116. Citation on page 76.

JAMES, B. R. **Probabilidade: um curso em nível intermediário**. [S.l.]: IMPA, 2015. Citation on page 49.

KHASMINSKII, R. **Stochastic Stability of Differential Equations**. 2. ed. [S.l.]: Springer Berlin, Heidelberg. 342 p. Citation on page 79.

KO, T.-W.; ERMENTROUT, G. B. Partially locked states in coupled oscillators due to inhomogeneous coupling. APS, v. 78, n. 1, p. 016203. Citation on page 76.

KURAMOTO, Y. Self-entrainment of a population of coupled non-linear oscillators. In: SPRINGER. **International symposium on mathematical problems in theoretical physics**. [S.l.]. p. 420–422. Citation on page 71.

____. Self-entrainment of a population of coupled non-linear oscillators. In: **International Symposium on Mathematical Problems in Theoretical Physics**. Berlin, Heidelberg: Springer Berlin Heidelberg, 1975. p. 420–422. Citation on page 17.

____. **Chemical Oscillations, Waves, and Turbulence**. Berlin: Springer, 1984. Citations on pages 17, 18, 44, and 45.

LAING, C. R. Chimera states in heterogeneous networks. American Institute of Physics, v. 19, n. 1, p. 013113. Citation on page 73.

LAPIDOTH, A. **A Foundation in Digital Communication**. [S.l.]: Cambridge University Press, 2017. Citations on pages 58 and 59.

LUCCIOLI, S.; OLMI, S.; POLITI, A.; TORCINI, A. Collective dynamics in sparse networks. APS, v. 109, n. 13, p. 138103. Citations on pages 75 and 76.

MARTENS, E. A. Chimeras in a network of three oscillator populations with varying network topology. American Institute of Physics, v. 20, n. 4, p. 043122. Citation on page 73.

MARTENS, E. A.; PANAGGIO, M. J.; ABRAMS, D. M. Basins of attraction for chimera states. IOP Publishing, v. 18, n. 2, p. 022002. Citation on page 73.

Marvel, S. A.; Mirollo, R. E.; Strogatz, S. H. Identical phase oscillators with global sinusoidal coupling evolve by Möbius group action. v. 19, n. 4, p. 043104. Citations on pages 70, 71, and 72.

MEISS, J. D. **Differential dynamical systems**. [S.l.]: Society for Industrial and Applied Mathematics, 2017. Citation on page 24.

MENCZER, F.; FORTUNATO, S.; DAVIS, C. A. **A First Course in Network Science**. [S.l.]: Cambridge University Press, 2020. Citations on pages 41 and 42.

MENDONCA, H. M.; TöNJES, R.; PEREIRA, T. Exponentially long transient time to synchronization of coupled chaotic circle maps in dense random networks. v. 25, n. 7. ISSN 1099-4300. Available: <https://www.mdpi.com/1099-4300/25/7/983>. Citations on pages 11, 12, 13, 72, 74, 77, and 78.

MONTBRIÓ, E.; PAZÓ, D.; ROXIN, A. Macroscopic description for networks of spiking neurons. American Physical Society, v. 5, p. 021028. Available: <https://link.aps.org/doi/10.1103/PhysRevX.5.021028>. Citation on page 70.

NEWMAN, M.; WATTS, D. Renormalization group analysis of the small-world network model. **Physics Letters A**, v. 263, n. 4, p. 341 – 346, 1999. Citations on pages 10 and 42.

NEWMAN, M. E. J. The structure of scientific collaboration networks. **Proceedings of the National Academy of Sciences**, National Academy of Sciences, v. 98, n. 2, p. 404–409, 2001. ISSN 0027-8424. Available: <https://www.pnas.org/content/98/2/404>. Citations on pages 33 and 38.

NéDA, Z.; RAVASZ, E.; BRECHET, Y.; VICSEK, T.; BARABáSI, A.-L. The sound of many hands clapping. **Nature**, v. 403, n. 6772, p. 849–850, 2000. Citation on page 44.

OLIVEIRA, M. de; LUZ, M. da; FIORE, C. Generic finite size scaling for discontinuous nonequilibrium phase transitions into absorbing states. APS, v. 92, n. 6, p. 062126. Citation on page 75.

OTT, E.; ANTONSEN, T. M. Long time evolution of phase oscillator systems. v. 19, n. 2. ISSN 1054-1500. 023117. Available: <https://doi.org/10.1063/1.3136851>. Citation on page 71.

____. Low dimensional behavior of large systems of globally coupled oscillators. American Institute of Physics, v. 18, n. 3, p. 037113. Citations on pages 71 and 72.

OTTINO-LÖFFLER, B.; STROGATZ, S. H. Volcano transition in a solvable model of frustrated oscillators. American Physical Society, v. 120, p. 264102. Available: <https://link.aps.org/doi/10.1103/PhysRevLett.120.264102>. Citation on page 73.

PAGANI, G. A.; AIELLO, M. The power grid as a complex network: A survey. **Physica A: Statistical Mechanics and its Applications**, v. 392, n. 11, p. 2688 – 2700, 2013. ISSN 0378-4371. Available: <http://www.sciencedirect.com/science/article/pii/S0378437113000575>. Citation on page 33.

PETER, F.; GONG, C. C.; PIKOVSKY, A. Microscopic correlations in the finite-size kuramoto model of coupled oscillators. American Physical Society, v. 100, p. 032210. Available: <https://link.aps.org/doi/10.1103/PhysRevE.100.032210>. Citation on page 73.

PETER, F.; PIKOVSKY, A. Transition to collective oscillations in finite kuramoto ensembles. American Physical Society, v. 97, p. 032310. Available: <https://link.aps.org/doi/10.1103/PhysRevE.97.032310>. Citation on page 73.

PIKOVSKY, A.; ROSENBLUM, M.; KURTHS, J. **Synchronization: A Universal Concept in Nonlinear Sciences**. [S.l.]: Cambridge University Press, 2003. Citation on page 17.

PIKOVSKY, A. S. Synchronization of oscillators with hyperbolic chaotic phases. v. 29, n. 1, p. 78–87. Citation on page 71.

RESTREPO, J. G.; OTT, E.; HUNT, B. R. Onset of synchronization in large networks of coupled oscillators. APS, v. 71, n. 3, p. 036151. Citations on pages 75 and 76.

SKARDAL, P. S.; RESTREPO, J. G. Hierarchical synchrony of phase oscillators in modular networks. APS, v. 85, n. 1, p. 016208. Citation on page 73.

SMALL, M.; HOU, L.; ZHANG, L. Random complex networks. **National Science Review**, v. 1, n. 3, p. 357–367, 2014. Citation on page 33.

STROGATZ, S. **Sync: The Emerging Science of Spontaneous Order**. New York: Hyperion, 2003. Citation on page 17.

STROGATZ, S. H. From kuramoto to crawford: exploring the onset of synchronization in populations of coupled oscillators. **Physica D: Nonlinear Phenomena**, v. 143, n. 1, p. 1 – 20, 2000. Citations on pages 17, 45, 46, and 65.

____. Exploring complex networks. **Nature**, v. 410, n. 6825, p. 268–276, 2001. ISSN 1476-4687. Available: <https://doi.org/10.1038/35065725>. Citation on page 33.

TANZI, M.; PEREIRA, T.; STRIEN, S. V. Robustness of ergodic properties of non-autonomous piecewise expanding maps. **Ergodic Theory and Dynamical Systems**, Cambridge University Press, v. 39, n. 4, p. 1121–1152, 2019. Citation on page 69.

TESCHL, G. **Ordinary Differential Equations and Dynamical Systems**. [S.l.]: American Mathematical Society, 2012. (Graduate studies in mathematics). Citations on pages 21, 22, and 25.

TOENJES, R.; MASUDA, N.; KORI, H. Synchronization transition of identical phase oscillators in a directed small-world network. **Chaos**, v. 20, 2010. Citations on pages 46, 47, and 63.

TÖNJES, R.; FIORE, C. E.; PEREIRA, T. Coherence resonance in influencer networks. Nature Publishing Group UK London, v. 12, n. 1, p. 72. Citation on page 73.

TÖNJES, R.; PIKOVSKY, A. Low-dimensional description for ensembles of identical phase oscillators subject to cauchy noise. APS, v. 102, n. 5, p. 052315. Citation on page 73.

WATTS, D. J.; STROGATZ, S. H. Collective dynamics of 'small-world' networks. **Nature**, v. 393, n. 6684, p. 440–442, 1998. ISSN 1476-4687. Available: <https://doi.org/10.1038/30918>. Citation on page 39.

WINFREE, A. T. Biological rhythms and the behavior of populations of coupled oscillators. **Journal of Theoretical Biology**, v. 16, n. 1, p. 15 – 42, 1967. ISSN 0022-5193. Citation on page 27.

____. **The geometry of biological time**. New York: Springer, 2001. Citation on page 17.

APPENDIX

A

PROOF OF THE THEOREM 2.3.1

Theorem 2.3.1. *Consider the eq. (2.1), where the flow φ is a function of class C^k, with $k \geq 1$. Assume the system has an asymptotically stable limit cycle γ and for a small $\varepsilon > 0$, let $B_\varepsilon(\gamma) \subset B(\gamma)$ be a neighborhood of γ, such that for every inital condition $z_0 \in B(\gamma)$ it is attracted to γ when time goes to infinity. Then,*

1. *there is a unique function $\alpha_x : \mathbb{R} \to \mathbb{R}^{n-1}$, such that I_x is an invariant graph of α under g. It means*

$$g(graph(\alpha_x)) = graph(\alpha_x); \tag{A.1}$$

with

$$graph(\alpha_x) = I_x = \{(u,v) \in B_\varepsilon(\gamma) : \forall u \in \mathbb{R}, \exists! v \in \mathbb{R}^{n-1}, \text{ such that } v = \alpha_x(u)\}, \tag{A.2}$$

where $B_\varepsilon(\gamma) \subset \mathbb{R} \times \mathbb{R}^{n-1}$, g is a time one map of the flow.

2. *for every $x \neq y$ in γ, I_x is mapped to I_y;*

3. *the*

$$\bigcup_{x \in \gamma} I_x \tag{A.3}$$

foliates the entire neighborhood $B_\varepsilon(\gamma)$ of γ, where for every $x, y \in \gamma$, $I_x \bigcap I_y = \emptyset$.

Proof. We define g in the same way of eq. (2.29), letting $\tau(x) = 1$ be the period of the orbit hits the cross-section $\Sigma \subset \mathbb{R}^n$ again, such that

$$g_\Sigma := \varphi(1, \cdot) : \Sigma \to \Sigma \tag{A.4}$$

is called of time-1 map. Since the flow is invariant on the limit cycle, after one period, implies that

$$g_\Sigma(x_0) = \varphi(1, x_0) = x_0. \tag{A.5}$$

for every $x_0 \in \gamma$. Then, x_0 is a fixed point of the map g and we can follow to prove the part (1) of the theorem.

Let $\gamma(0) = x_0$ be a point on γ, since it is an asymptotically stable limit cycle, by the theorem 2.2.2 and lemma 2.2.3 the monodromy matrix at $M_{x_0}(0)$ has one eigenvalue $\mu_1 = 1$ and $(n-1)$ eigenvalues $0 < \mu_k < 1$, with $k = 1, ..., n-1$. Then, it is possible decompose my space into two subspaces: tangent along γ at x_0 , and transversal to γ also at x_0.

Given this decomposition and considering the small neighborhood of x_0 and γ defined as

$$B_\varepsilon(\gamma)(x_0) = \{z \in \mathbb{R} \times \mathbb{R}^{n-1} : d(z, x_0) < \varepsilon\}, \tag{A.6}$$

for a small $\varepsilon > 0$, we can introduce a suitable local coordinate system without loss of generality, considering $x_0 = (0,0)$ as the origin, and for every point $z_0 = (u,v) \in B_\varepsilon(\gamma)(x_0)$

$$u \in \mathbb{R} \text{ and } v \in \mathbb{R}^{n-1}.$$

Then, we define the map g as follows

$$\begin{pmatrix} u \\ v \end{pmatrix} \mapsto \begin{pmatrix} H(u,v) \\ Av + R(u,v) \end{pmatrix}, \tag{A.7}$$

where A is a $(n-1) \times (n-1)$ matrix that contains all the u_k eigenvalues of the monodromy matrix, and $H : \mathbb{R} \times \mathbb{R}^{n-1} \to \mathbb{R}$, $R : \mathbb{R} \times \mathbb{R}^{n-1} \to \mathbb{R}^{n-1}$ are at least C^1 functions with

$$A(0) = 0,\ H(0,0) = 0 \text{ and } R(0,0) = 0. \tag{A.8}$$

Since R is differentiable and defined in the convex set $B_\varepsilon(x_0)$, it means that for $a, b \in B_\varepsilon(x_0)$, $a + \lambda(b-a) \in B_\varepsilon(x_0)$ for $0 \leq \lambda \leq 1$. Let $0 < \delta \ll 1$, such that

$$\sup_{0 \leq \lambda \leq 1} \|DR(a + \lambda(b-a))\| \leq \delta, \tag{A.9}$$

then by the mean value theorem, follows that

$$|R(a) - R(b)| \leq \delta |a - b|. \tag{A.10}$$

Consider $b = (0,0)$ and $a = (u,v) \in B_\varepsilon(x_0)$, by eq. (A.10) we have

$$|R(u,v)| \leq \delta |(u,v)|, \tag{A.11}$$

where

$$lip(R) < \delta \tag{A.12}$$

and similarly it is possible to show that $lip(H) < \mu$, where $\mu \ll 1$.

Since A has no zero eigenvalues it is invertible, then bijective and we also assume that

$$lip(A^{-1}) lip(H) < 1. \tag{A.13}$$

Then, at this stage and by eqs. (A.8), (A.12) and (A.13), all the hypothesis of the graph transform theorem given by Hadamard are satisfied. Hence, we draw the conclusions of this theorem, which is precisely the part (1). Therefore, part (1) holds using this theorem.

Let

$$g_{\Sigma_0} := \varphi(1,\cdot) : \Sigma_0 \to \Sigma_0 \tag{A.14}$$

be the time-1 map and $\Sigma_0 \subset B(\gamma)$ be a cross-section of γ, where B_ε is a neighborhood of γ. Since $\Sigma_0 \bigcap \gamma = \{x_0\}$ is the fixed point of g_{Σ_0} and γ is asymptotically stable, we have that

$$g_{\Sigma_0}^{m+1}(z_0) \to x_0 \text{ as } m \to \infty. \tag{A.15}$$

for every $z_0 \in \Sigma_0$, where by definition

$$\begin{aligned} g_{\Sigma_0}^{m+1}(z_0) &= \varphi(m+1, z_0), \\ &= \varphi(1, \varphi(m, z_0)), \\ &= \varphi(1, g_{\Sigma_0}^{m}(z_0)). \end{aligned} \tag{A.16}$$

Similarly, letting $s \in \mathbb{R}^+$ be fixed, consider

$$g_{\Sigma_1} := \varphi(1+s,\cdot) : \Sigma_1 \to \Sigma_1, \tag{A.17}$$

where $\Sigma_1 \subset B_\varepsilon$ is also a cross-section and $\Sigma_1 \bigcap \gamma = \{x_1\}$ is the fixed point of g_{Σ_1}. Then,

$$g_{\Sigma_1}^{n+1}(z_1) \to x_1 \text{ as } n \to \infty. \tag{A.18}$$

for every $z_1 \in \Sigma_1$, where using the same process as in eq. (A.16)

$$g_{\Sigma_1}^{n+1}(z_1) = \varphi(1+s, g_{\Sigma_1}^{n}(z_1)). \tag{A.19}$$

Therefore, by the following diagram

$$\begin{array}{ccccc} z_0 = \varphi(1,z_0) & \xrightarrow{g^{m+1}} & \varphi(1, g_{\Sigma_0}^m(z_0)) & \xrightarrow{m\to\infty} & x_0 \\ \Big\downarrow \varphi & & & & \Big\downarrow \varphi \\ z_1 = \varphi(1+s,z_0) & \xrightarrow{g^{n+1}} & \varphi(1+s, g_{\Sigma_1}^n(z_1)) & \xrightarrow{n\to\infty} & x_1 \end{array}$$

implies that Σ_0 is mapped to Σ_1 under the flow, where the graph of α_x is precisely $I_x = \Sigma_x$ given previously in the part (1). Then, the part (2) of the theorem holds.

Since two distinct nearby points on γ stay close for all time, and for each $x \in \gamma$ is an asymptotically stable fixed point of g_Σ^m we conclude that for every $x \neq y$ in γ the $I_x \bigcap I_y = \emptyset$. Thus, the last part of theorem holds and we complete the proof to the theorem. □

ANNEX

A

ARTICLE: EXPONENTIALLY LONG TRANSIENT TIME TO SYNCHRONIZATION OF COUPLED CHAOTIC CIRCLE MAPS IN DENSE RANDOM NETWORKS

entropy

MDPI

Article

Exponentially Long Transient Time to Synchronization of Coupled Chaotic Circle Maps in Dense Random Networks

Hans Muller Mendonca [1,†], Ralf Tönjes [2,*,†] and Tiago Pereira [1]

[1] Instituto de Ciências Matemáticas e Computação, Universidade de São Paulo, São Carlos 13566-590, SP, Brazil; hans.mendonca@usp.br (H.M.M.); tiago@icmc.usp.br (T.P.)
[2] Institute of Physics and Astronomy, Potsdam University, 14476 Potsdam-Golm, Germany
* Correspondence: toenjes@uni-potsdam.de
† These authors contributed equally to this work.

Abstract: We study the transition to synchronization in large, dense networks of chaotic circle maps, where an exact solution of the mean-field dynamics in the infinite network and all-to-all coupling limit is known. In dense networks of finite size and link probability of smaller than one, the incoherent state is meta-stable for coupling strengths that are larger than the mean-field critical coupling. We observe chaotic transients with exponentially distributed escape times and study the scaling behavior of the mean time to synchronization.

Keywords: synchronization; random networks; chaotic maps; mean-field analysis; finite size effects

Citation: Mendonca, H.M.; Tönjes, R.; Pereira, T. Exponentially Long Transient Time to Synchronization of Coupled Chaotic Circle Maps in Dense Random Networks. *Entropy* **2023**, *25*, 983. https://doi.org/10.3390/e25070983

Academic Editor: Andrea Rapisarda

Received: 24 April 2023
Revised: 16 June 2023
Accepted: 17 June 2023
Published: 27 June 2023

1. Introduction

Complex nonlinear systems often exhibit collective synchronization phenomena which can play an important role for the overall functioning of a system [1–3]. Phase oscillator models can elucidate key aspects of the mechanism that generates the collective motion [4]. The Kuramoto model, for instance, is particularly useful in describing groups of weakly coupled oscillators such as Josephson junctions, and they can be analyzed in almost full detail in the thermodynamic limit of infinitely many oscillators. Indeed, Kuramoto himself initially studied the fully connected networks of coupled oscillators with frequency heterogeneity, and obtained the critical value of the coupling strength for the transition from incoherence to synchronized collective oscillations [5].

While such predictions are obtained in the thermodynamic limit, they have been used as fruitful approaches to describe networks with finitely many oscillators [6,7]. However, recent work has shown that finite size fluctuations or sparse connections in the network can significantly impact on the overall dynamics. In fact, in certain models, synchronization cannot, even approximately, be predicted from the mean-field approximation in the thermodynamic limit [8]. That is, in these models, a transition to synchronization occurs or is inhibited because of finite size fluctuations [9,10]. The interplay between mean-field predictions and finite-size fluctuations for general models remains elusive and requires further investigation.

In this work, we study chaotic phase maps in dense networks where the mean-field dynamics can be analyzed exactly in the thermodynamic limit. For small coupling, due to the chaotic phase dynamics, only incoherence is stable. For a range of coupling strengths, mean-field analysis predicts coexistence between complete chaotic synchronization and incoherence, and for strong coupling, the incoherence becomes unstable. Then, complete synchronization is the globally attracting state in our model. Our results are two-fold:

(i) For coupling strengths with a stable coexistence of incoherence and synchronization, although incoherence is locally attracting, finite-size fluctuations can take the system into the basin of attraction of the absorbing state of complete synchronization. Starting near incoherence with uniformly distributed random oscillator phases, the distribution

of transient times towards synchronization is exponential and scales as a power of the system size.

(ii) Above the critical coupling strength, in dense but incomplete networks, although linear stability analysis of the mean-field equations suggests that any nonzero mean field, e.g., finite size fluctuations of the mean field, will grow exponentially fast, we observe an exponentially long chaotic transient in the incoherent state. Such a delayed transition to synchronization has so far not been described in dense networks of coupled phase oscillators or coupled chaotic maps.

2. Model of Coupled Chaotic Maps

The local phase dynamics in each node is modelled as a Bernoulli map of the circle with time steps $t \in \mathbb{Z}$

$$\varphi(t+1) = f(\varphi(t)) = 2\varphi(t) \mod 2\pi, \tag{1}$$

or via the abuse of notation on the complex unit circle $z = \exp(i\varphi)$, we write $z(t+1) = f(z(t)) = z(t)^2$. This map is chaotic and structurally stable [11]. That is, the statistical properties of the map persist under small perturbations. Therefore, for small coupling, the maps behave as nearly independent, and no collective dynamics is possible for small coupling. In [12], the global coupling of the phase dynamics is implemented as a Moebius map on the complex unit circle. The Moebius map has been shown to give exact solutions of sinusoidally forced phase dynamics [13], including the Kuramoto model, Winfree-type phase equations, and via a nonlinear transformation, the dynamics of theta neurons [14]. It is therefore a meaningful alternative to the sine coupling in the standard circle map. Here, we use a composition of (1) and a Moebius map (see Figure 1)

$$z(t+1) = M(f(z(t)), \Phi(t), \tau(t)), \tag{2}$$

where

$$M(w, \Phi, \tau) = \frac{e^{i\Phi}\tau + w}{1 + e^{-i\Phi}\tau w} \tag{3}$$

for a coupling intensity $-1 < \tau < 1$, an angle of contraction $\Phi \in \mathbb{S}^1$, and a point $w \in \mathbb{D} = \{z \in \mathbb{C} : |z| < 1\}$ on the open complex unit disc. The family of Moebius maps is a group of biholomorphic automorphisms of $\mathbb{D}$, and via analytic continuation, these transformations map the boundary of $\mathbb{D}$ bijectively onto itself. The effect of (3) on the unit disc is a contraction of almost all points towards $\exp(i\Phi)$ on the boundary where $\lim_{\tau\to\pm1} M(w, \Phi, \tau) = \pm\exp(i\Phi)$ and $\lim_{\tau\to0} M(w, \Phi, \tau) = w$. The parameter τ characterizes the strength of the contraction. For $\tau \to 0$, the map (2) approaches the uncoupled dynamics (1). Moreover, the family of wrapped Cauchy distributions

$$p(\varphi) = \frac{1}{2\pi}\frac{1 - R^2}{|1 - Re^{i(\varphi-\Theta)}|^2} \tag{4}$$

which includes incoherence as the uniform distribution when $R \to 0$ and a delta distribution at $\varphi = \Theta$ when $R \to 1$, is invariant under (2) and (3) [12,13,15]. This family of continuous phase measures, in the context of phase synchronization, is known as the Ott-Antonsen manifold, and assuming this form of phase distribution is equivalent to the so called Ott-Antonsen ansatz [16,17]. The Ott-Antonsen manifold is parameterized using the mean-field amplitude R and the mean-field angle Θ

$$Z = Re^{i\Theta} = \int_0^{2\pi} e^{i\varphi} p(\varphi)\, d\varphi. \tag{5}$$

The mean-field amplitude R is the Kuramoto order parameter [18], which is zero for incoherence, i.e., a uniform phase distribution, and $R = 1$ for complete synchronization

$\varphi_n = \Theta$ (a.s.). Furthermore, the higher circular moments Z_q on the Ott-Antonsen manifold with $q \in \mathbb{Z}$ are integer powers of the mean field

$$Z_q = \int_0^{2\pi} e^{iq\varphi} p(\varphi)\, d\varphi = Z^q. \tag{6}$$

As a consequence, phase doubling maps the circular moments as $f(Z_q(t)) = Z_{2q}(t) = Z_2^q(t) = f(Z_1(t))^q$, leaving the Ott-Antonsen manifold invariant and mapping the mean-field amplitude and phase as $R \to R^2$ and $\Theta \to 2\Theta$.

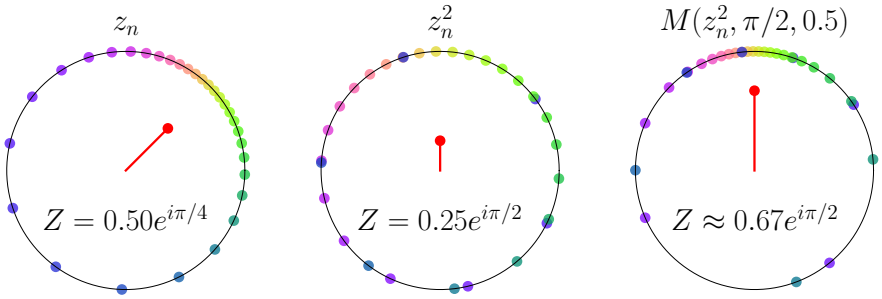

Figure 1. Dynamics of phases. $N = 30$ points on the complex unit circle colored by phase, and corresponding mean field (red dot inside the unit circle). From left to right: initial phase configuration at the points z_n with mean-field amplitude $R = 0.5$ and mean-field phase $\Theta = \pi/4$, after chaotic phase doubling z_n^2 with $R^2 = 0.25$ and $2\Theta = \pi/2$, and after subsequent contraction toward the angle $\pi/2$ with intensity $\tau = 0.5$.

To couple the dynamics of the Bernoulli maps (2), the parameters $\Phi(t)$ and $\tau(t)$ in (3) should be defined as functions of the ensemble mean field. Following [12], we define the contraction angle $\Phi(t)$ and the coupling intensity $\tau(t)$ as

$$Z(t) = \frac{1}{N}\sum_{n=1}^{N} z_n(t) = R(t)e^{i\Theta(t)} \tag{7}$$

$$\Phi(t) = 2\Theta(t) \tag{8}$$

$$\tau(t) = \tanh\Big(\frac{\varepsilon}{2}R(t)\Big), \tag{9}$$

where ε is a coupling strength. For $\tau = 1$, when $\varepsilon R \to \infty$, the phases are contracted to a single point $\exp(2i\Theta)$ on the unit circle. For small values of εR, we can expand (2) to the linear order and obtain the more familiar form of mean-field coupled circle maps with phase doubling

$$\varphi_n(t+1) = 2\varphi_n(t) + \varepsilon R(t)\sin(2\Theta(t) - 2\varphi_n(t)) + O(\varepsilon^2 R^2(t)). \tag{10}$$

The crucial observation is that on the Ott-Antonsen manifold, the mean-field $Z = R\exp(i\Theta)$ transforms exactly the same way via (2), (3) as each element $z = \exp(i\varphi)$ on the unit circle [12,13]; that is,

$$Z(t+1) = M(Z^2(t), \Phi(t), \tau(t)). \tag{11}$$

It is highly unusual that a closed analytic expression for the dynamics of the mean field can be derived and thus analyzed in coupled nonlinear dynamical systems. The reduction in infinitely dimensional microscopic dynamics to the low-dimensional dynamics of the mean-field [16] has been tremendously successful in the analysis of synchronization phenomena over the last decade, while the effects of the finite system size N remain difficult to analyze [19,20]. We note that the point measure of a finite ensemble of phases is never actually on the Ott-Antonsen manifold, but can, in some sense, be arbitrarily close to the so-called thermodynamic limit, i.e., the limit of the infinite system size $N \to \infty$.

Applying the Ott-Antonsen ansatz to networks of phase oscillators is possible if the network structure allows for the partitioning of the vertices into a few classes of equivalent vertices. Assuming that all vertices of a class are subjected to the same sinusoidal forcing, the dynamics of the phases in the network can be reduced to the dynamics of coupled mean fields on the Ott-Antonsen manifold for each vertex class [10,21–24]. Additionally, heterogeneity in the oscillators and fluctuations in the forces can be incorporated into the mean field dynamics if they follow Cauchy distributions [25–27].

2.1. Mean-Field Analysis

The mean-field dynamics (11) can be written in terms of the polar representation

$$\Theta(t+1) = f(\Theta(t)) \quad \text{and} \quad R(t+1) = \frac{\tau(t) + R^2(t)}{1 + \tau(t)R^2(t)}. \tag{12}$$

This means that the dynamics of the phase Θ decouples from the amplitude and will evolve chaotically. Using Equations (9) and (12), we obtain the amplitude dynamics

$$R(t+1) = \frac{\tanh\left(\frac{1}{2}\varepsilon R(t)\right) + R^2(t)}{1 + \tanh\left(\frac{1}{2}\varepsilon R(t)\right)R^2(t)} \tag{13}$$

which describes the exact evolution of the order parameter R in a closed form. We can readily determine the fixed points of the mean-field amplitude $R(t)$ and their linear stability. Both the complete synchronization $R = 1$ and the complete desynchronization $R = 0$ are fixed points of (13), and change stability at unique critical points $\varepsilon_1 = \ln(2) \approx 0.69$ and $\varepsilon_0 = 2$, respectively, as determined by the eigenvalues of Jacobian of Equation (13) at these fixed points. These critical points are connected by an unstable fixed point branch $(\varepsilon(R_u), R_u)$, where

$$\varepsilon(R_u) = \frac{1}{R_u} \log\left(\frac{(1+R_u)^2}{1+R_u^2}\right). \tag{14}$$

This expression is derived from (13) by setting $R(t+1) = R(t) = R_u$ and resolving the equation for ε.

This means that this system of all-to-all coupled, identical chaotic phase maps will always evolve to complete synchronization or complete desynchronization, with a small region $\ln(2) < \varepsilon < 2$ of bistability (Figure 2a).

2.2. Extension to Networks

Next, we have studied the same phase dynamics on a random network of N maps which are coupled to exactly k different, random neighbors. Here, each phase φ_n couples to a local mean field

$$Q_n = R_n e^{i\Theta_n} = \frac{1}{k}\sum_{n=1}^{N} A_{nm} z_m \tag{15}$$

where A_{nm} are the entries of the adjacency matrix, i.e., equal to one if there is a link from vertex m to vertex n, but zero otherwise, and $k = \sum_{m=1}^{N} A_{nm}$ is the in-degree of node n, which, for computational simplicity, we assume to be identical for all nodes. Thus, with $\tau_n = \tanh\left(\frac{\varepsilon}{2}R_n\right)$, the dynamics of the phases coupled through a network are

$$z_n(t+1) = \frac{e^{2i\Theta_n(t)}\tau_n(t) + z_n^2(t)}{1 + e^{-2i\Theta_n(t)}\tau_n(t)z_n^2(t)}. \tag{16}$$

A class of networks is dense if $\lim_{N\to\infty}\langle k\rangle/N = p > 0$, where $\langle k\rangle$ is the mean node degree. Therefore, p is the fraction of nodes, in relation to the system size N, that an oscillator is coupled to. Since dense networks are defined in the limit of $N \to \infty$, there is no sharp distinction between sparse and dense networks of finite size. We refer

to a finite network as dense if two nodes share more than one neighbor on average, i.e., $\langle k \rangle^2 / N = p^2 N > 1$. In large dense networks, the local mean fields of the oscillators in the neighborhood of each node (15) are equal to the global mean field, with a deviation of $O(1/\sqrt{k})$, where k is the size of the neighborhood, i.e., the in-degree of the node. Therefore, mean-field theory should be exact for dense networks in the thermodynamic limit where $\langle k \rangle \to \infty$.

The network model. First, we wish to compare the simulation results directly with our mean-field analysis. For large random networks with a link density $p = k/N$ and $0 < p < 1$, the numerical simulations are time-consuming since the N local mean fields at each node in the network need to be computed in each time step. To simplify these computations, we use a random network where each node couples to exactly k different random neighbors. This model with a unique in-degree of k for each node is slightly different from the Erdös Renyi model, with a Poissonian in-degree distribution of small relative width $\mathrm{std}(k)/\langle k \rangle \sim 1/\sqrt{k}$. For large k, the results of the simulations in our random network model and other random networks with uncorrelated node degrees and a vanishing relative width of the degree distribution are expected to be identical.

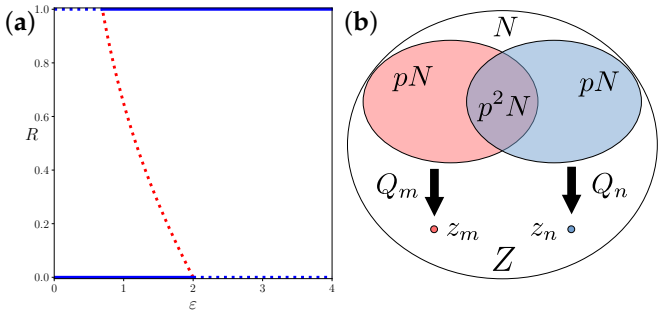

Figure 2. Bifurcation diagram of the mean-field amplitude and a representation of the network interaction. In (**a**), the bifurcation diagram of the all-to-all coupling mean-field dynamics (12), i.e., on the Ott-Antonsen manifold. Dotted lines show linearly unstable fixed points and solid lines show linearly stable fixed points in the thermodynamic limit. (**b**) Venn diagram of a dense network with N vertices and connection probability p. The sets of neighbors of nodes m and n are of size pN and their overlap is of size $p^2 N$, resulting in correlated local mean fields $Q_m = R_m \exp(i\Theta_m)$ and $Q_n = R_n \exp(i\Theta_n)$ acting on the states z_m and z_n. The ratio of the amplitudes of the local mean fields and the global mean field are independent of the network size N.

3. Results

3.1. Distributions of Transient Times

We perform a large number M of simulations $m = 1 \ldots M$ from independent, uniformly distributed random initial phases over a maximum of T steps and record in each simulation the first time step t_m when $R \geq 0.5$, i.e., the transition time from an incoherent state to complete synchronization. Finite-size scaling for such a discontinuous transition is challenging [28]. The exponential distribution of the times t_m, according to some characteristic transition rate, can be checked in a rank plot of time points t_m, which gives the sample complementary cumulative distribution $C(t) = \mathrm{prob}(t \geq t_m) = \mathrm{rank}(t_m)/M$ (Figure 3a,d).

An exponential tail distribution $C(t)$ up to observation time T indicates an exponential distribution of transient times. Since the simulation time is finite, transition times $t_m \geq T$ are not observed, which represents a problem when we are interested in the average time to synchronization. However, assuming a discrete exponential, i.e., geometric distribution, a maximum likelihood estimation of the average transition time is possible up to values considerably exceeding the observation time T (see Appendix A).

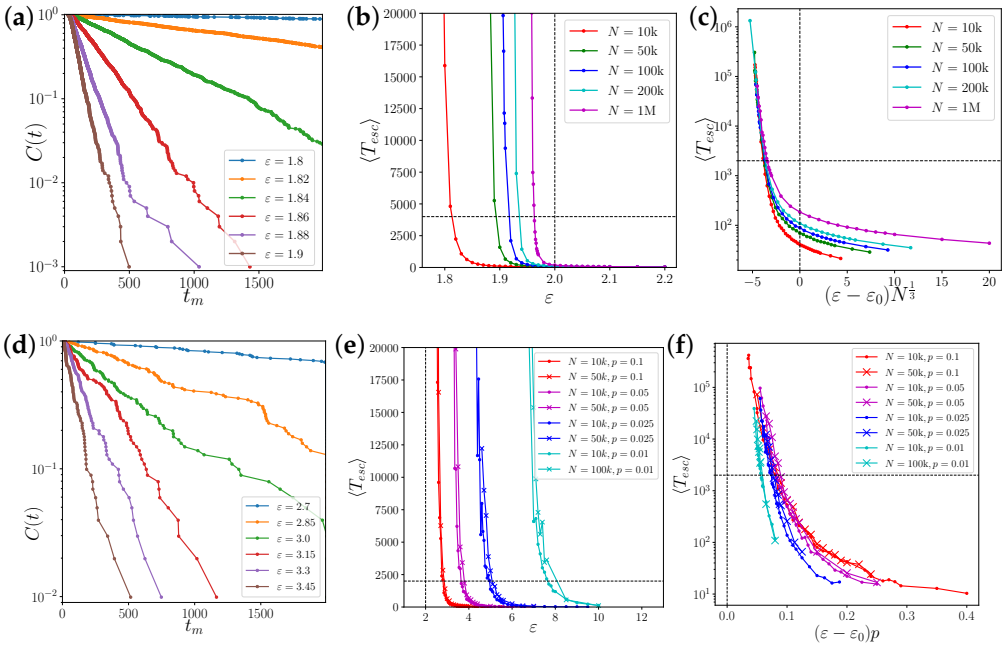

Figure 3. Statistics of transient times t_m to synchronization. (**a**–**c**) In the fully connected network; (**d**–**f**) in random networks of various link densities $p = k/N$. The left panels show straight lines in semi-logarithmic plots of cumulative tail distributions of the transient times, demonstrating the rate character of the transition process. The middle panels show the estimated average transient times for various combinations of system sizes N, coupling strengths ε, and link densities p. The mean field critical coupling strength $\varepsilon_0 = 2.0$ and the maximum observation time T are marked by dashed lines. In the globally coupled system in pannels (**a**–**c**), the transient time depends strongly on the system size N, whereas in dense networks and above ε_0 (**d**–**f**), the transient time depends strongly on the link density $p = k/N$, but not on the system size. We demonstrate the scaling of the transient times in panels (**c**) and (**f**) on the right. In the globally coupled system, the exponential divergence of the transient times below ε_0 appears to be a function of $(\varepsilon - \varepsilon_0)N^{\frac{1}{3}}$. In dense networks, the exponential divergence is roughly a function of $(\varepsilon - \varepsilon_0)p$.

Denoting the number of simulations that synchronize at times $t_m < T$ as M_T, and defining the observable values $l_m = \min(t_m, T)$, the maximum likelihood estimation of the expected value $T_{esc} = \mathrm{E}[t_m]$ for the geometric distribution is

$$T_{esc} = \frac{\langle l_m \rangle M}{M_T}. \tag{17}$$

with the sample mean $\langle l_m \rangle$. If the transition to synchronization is observed in all simulations, i.e., $M_T = M$, the estimator is simply the sample mean of t_m, which is an estimator of T_{esc} for arbitrary transient time distributions. However, when most runs do not synchronize within the finite simulation time T, the ratio M/M_T contains additional information, and the estimated mean escape time can be much larger than the observation time.

3.2. During Coexistence: Escape over the Unstable Branch

In [29], it was reported that the transition from incoherence to collective dynamics in sparse networks of coupled logistic maps is of the mean-field type. The analysis in [30] predicts a shift in the critical coupling strength in random networks of Kuramoto phase oscillators of the order $\langle k \rangle^2 / \langle k^2 \rangle$ due to degree inhomogeneity, and $1/\langle k \rangle$ due to finite size fluctuations of the local mean fields. That is, in dense, homogeneous networks with $\langle k \rangle^2 / \langle k^2 \rangle \to 1$ and $\langle k \rangle \to \infty$, the critical coupling strength does not change. We expected to find similar behaviors for network-coupled Bernoulli maps. In complete or almost complete networks $k/N = p \approx 1$ for $\varepsilon < 2$, there is a small probability that finite size fluctuations

bring the order parameter R above the unstable branch, leading to a spontaneous transition to complete synchronization, as shown in Figure 4a. We first observe the scaling of the transient time in fully connected networks with $p = 1$. For values of $\varepsilon < \varepsilon_0 = 2.0$, the transition rate to synchronization scales strongly with the size N of the system (Figure 3b,c). However, for values $\varepsilon > \varepsilon_0$, the average transition time depends very weakly on N, as the system grows exponentially fast from a state of incoherence, with $R \approx 1/\sqrt{N}$. We estimate a finite size scaling exponent β below the transition threshold by collapsing the curves $T_{esc}(\varepsilon, N)$ using the ansatz $T_{esc}(\varepsilon, N) = T_{esc}\left((\varepsilon - \varepsilon_0)N^{\beta}\right)$. The data are consistent with an ad hoc exponent of $\beta = 1/3$ (Figure 3c).

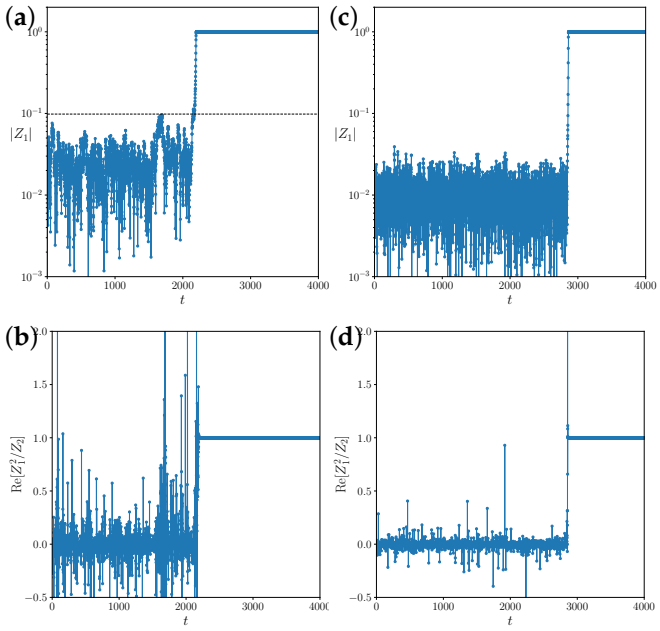

Figure 4. Transient to synchronization for $N = 10{,}000$ coupled maps in (**a**,**b**), a fully connected network with coupling strength $\varepsilon = 1.81$ below the critical coupling $\varepsilon_0 = 2$, and (**c**,**d**), in a random network with connection probability $p = 0.1$ for a coupling strength of $\varepsilon = 2.3$ above the critical coupling. The upper panels (**a**,**c**) show the order parameter $R(t)$, and the lower panels (**b**,**d**), the real part of the ratio of the first two circular moments $\mathrm{Re}[Z_1^2/Z_2]$. This serves as a visual measure of the alignment of the system state with the Ott-Antonsen manifold, where the ratio is exactly equal to one. The dashed line in (**a**) marks the value of the unstable fixed point of the mean-field dynamics, $R_u = 0.098$. Above that value, the state of complete synchronization is attractive on the Ott-Antonsen manifold. In (**b**,**d**), the incoherent state $R = 0$ is unstable; however, finite size fluctuations do not grow exponentially. Instead, we observe a long chaotic transient.

3.3. Above the Critical Coupling Strength: Long Chaotic Transient

Above the critical coupling strength $\varepsilon > \varepsilon_0 = 2$, we expected finite size fluctuations to grow exponentially fast and independently of N, as predicted by linear stability analysis of the mean-field Equations (13). Instead, for small connection probabilities $0 < p < 1$, we have observed a chaotic transient with seemingly stationary finite size fluctuations $O(1/\sqrt{N})$ of the mean field (Figure 4). In the large N limit, the distribution of the transient times depends on the link density p with increasingly long transients as p is decreased, but it is otherwise independent of N.

A coupling strength for which a transition to complete synchronization could still be observed within the simulation time was considerably larger than the mean-field critical coupling $\varepsilon_0 = 2$. That is, even in dense networks and above the mean-field critical coupling, finite size fluctuations will not necessarily result in the nucleation and exponential growth of a collective mode. Such a delayed transition to synchronization [31] has so far not been described in systems of coupled phase oscillators [30,32,33] or coupled logistic maps [29].

In Figure 3f, we plot T_{esc} over $(\varepsilon - \varepsilon_0)p$ to demonstrate that the average transition time is roughly scaling as $1/p$. We do not look for higher-order corrections such as a weak dependence of ε_0 on p, although the curves do not collapse perfectly. Note that the escape time is largely independent of the network size (Figure 3e,f). For $p = 0.1$, 0.05, and 0.025 we have performed simulations with $N = 10^4$ (circles) and with $N = 5 \times 10^4$ (crosses) for comparison. For $p = 0.01$, we compare network sizes $N = 10^4$ (circles) with very time-consuming simulations in networks with $N = 10^5$ (crosses).

3.4. Discussion of Finite Size Scaling

Mean field theory assumes a phase distribution on the Ott-Antonsen manifold. The characteristic function of a wrapped Cauchy distribution is the geometric sequence $Z_q = Z^q$ of circular moments (6). However, in the incoherent state with N independent uniformly distributed phases φ_n the circular moments of an ensemble

$$Z_q = \frac{1}{N} \sum_{n=1}^{N} e^{iq\varphi_n} \tag{18}$$

are almost independent complex numbers with a Gaussian distribution of mean zero and a variance of $1/N$ by virtue of the central limit theorem. The action of the Bernoulli map on the circular moments is the shift

$$Z_q \to Z_{2q}, \tag{19}$$

that is, it is achieved by discarding all odd circular moments. The exponential growth of the order parameter in accordance to mean field theory is expected after the distribution comes close to the Ott-Antonsen manifold, i.e., when the first few circular moments align by chance sufficiently under the mapping (19); in particular, $Z_2(t) \approx Z_1^2(t)$. Unless the directions of Z_2 and Z_1^2 align by chance, as they would on the Ott-Antonsen manifold, the subsequent contraction of strength εR in the direction of Z_1^2 after the phase doubling may even decrease the amplitude of the order parameter. In addition, for coupling strengths ε below the critical value, $R = |Z_1|$ must be above the unstable branch $R > R_u(\varepsilon) \sim (\varepsilon_0 - \varepsilon)$.

The rate of such a random event should depend on the ratio between $R_u(\varepsilon)$ and the standard deviation $1/\sqrt{N}$ of the Gaussian distribution of the complex mean field. Based on this scaling argument, the expected time to synchronize should scale as $T_{esc} = T_{esc}((\varepsilon - \varepsilon_0)\sqrt{N})$ below the critical coupling. The best collapse of the estimated escape times in fully connected networks of coupled Bernoulli maps was observed by scaling the distance to ε_0 with $N^{1/3}$ (Figure 4c), i.e., the exponential divergence of the escape time approaches ε_0 slower than $1/\sqrt{N}$ in the thermodynamic limit. One possibility for this discrepancy is that the scaling argument only considers the chance of $R > R_u$ and not the alignment process of the higher-order circular moments.

Above the critical coupling strength, there is only the condition of the alignment of circular moments with the Ott-Antonsen manifold for the initiation of exponential growth. Since in the incoherent state, all circular moments are random Gaussian with identical variance, the alignment process (19) is strictly independent of the system size N. Once exponential growth in the direction of the Ott-Antonsen manifold occurs, the time to synchronization is logarithmic, that is, it is weakly dependent on N. However, it appears that the alignment with the Ott-Antonsen manifold needs to be stronger for networks with link densities of $p < 1$. For small link densities, the divergence of the escape time occurs at larger values $\varepsilon > \varepsilon_0$. This is reminiscent of stabilization by noise [34], where a system is driven away from a low-dimensional unstable manifold of a fixed point into stronger attracting stable directions.

In simulations of dense random networks of coupled Bernoulli maps, we could see the independence of the mean escape time from the network size and the scaling of the escape time with roughly $\sim 1/p$ (Figure 3f). To explain this scaling, we argue that mean field theory might be extended to dense networks, where each node couples to a finite

neighborhood of pN nodes in the network, and for every two nodes, these neighborhoods overlap on a set of size p^2N (Figure 2b). The local mean fields are Gaussian random forces of mean value Z, variance $1/k = 1/pN$, and a pairwise correlation of p, which is the relative size of the overlap. The decrease in correlation between the local mean fields in networks with link densities $p < 1$ can be interpreted as individual, finite size noise on the maps, which couple to the global mean field, plus some uncorrelated random deviation. Therefore, the contractions of the phases do not occur in the same direction for different nodes in the network. The strength of the contraction in the direction of the mean field is effectively reduced by the factor p, i.e.,

$$\tau = \tanh\left(\frac{1}{2}\varepsilon R\right) p \approx \frac{1}{2}\varepsilon p R \tag{20}$$

shifting the coupling strength dependence of the transition time (above ε_0) by a factor of $1/p$.

4. Conclusions

We have investigated the synchronization of coupled chaotic maps in dense random networks, utilizing mean-field equations and examining network configurations with different link probabilities. Firstly, we noticed the existence of chaotic transients to synchronization within these networks. This means that the incoherent state can persist for extended periods before transitioning into synchronization. This finding led us to study the statistics of transient times and their scaling behaviors in the process of synchronization. The transition times follow exponential distributions, indicating spontaneous transitions at a constant rate. It is noteworthy that the transition from incoherence to complete synchronization only occurs spontaneously in networks of finite size. Additionally, we have observed a remarkable dependence of the transient times to synchronization on the link probability p, represented by the ratio of the in-degree to the total number of nodes, at coupling strengths where an immediate transition to synchrony would be expected from mean field theory. Whether such a delayed transition is due to the specifics of our model or is typical for a more general class of dynamics remains an open question.

Author Contributions: Conceptualization, H.M.M., R.T. and T.P.; numerical simulations, H.M.M. and R.T.; mean-field analysis, H.M.M. and R.T.; formal analysis, R.T.; writing, H.M.M., R.T. and T.P.; supervision, T.P. All authors have read and agreed to the published version of the manuscript.

Funding: This research was funded by the FAPESP CEMEAI 391, Grant No. 2013/07375-0, Serrapilheira Institute (Grant No. Serra-392 1709-16124), Newton Advanced Fellow of the Royal Society (393 NAF\R1\180236), CAPES and CNPq, Grant No 166191/2018-3.

Data Availability Statement: The Python code for the numerical simulations is available upon reasonable request from the corresponding author.

Conflicts of Interest: The authors declare no conflict of interest.

Appendix A

Here, we calculate the maximum likelihood estimation for the mean value of a geometric distribution $P(t;\alpha) = (1-\alpha)\alpha^t$ for discrete values $t = 0, 1, \ldots$ of time steps when only times $t < T$ can be observed. The expected value for the geometric distribution is

$$\mathrm{E}[t] = (1-\alpha)\sum_{t=0}^{\infty} t\alpha^t = \frac{\alpha}{1-\alpha}. \tag{A1}$$

Since the times t_m, $m = 1 \ldots M$ are only observable up to step $T-1$, we define $l_m = \min(t_m, T)$. The probabilities for the possible values of l_m are

$$P(l_m = T;\alpha) = 1-(1-\alpha)\sum_{t=0}^{T-1}\alpha^t = \alpha^T \tag{A2}$$

$$P(l_m = t < T;\alpha) = (1-\alpha)\alpha^t. \tag{A3}$$

The derivative of the log-likelihood of M independent observations l_m with respect to the parameter α is

$$\frac{\partial_\alpha P(l_1, l_2, \ldots, l_M;\alpha)}{P(l_1, l_2, \ldots, l_M;\alpha)} = \sum_{m=1}^{M}\frac{\partial_\alpha P(l_m;\alpha)}{P(l_m;\alpha)}. \tag{A4}$$

For the probabilities (A2) and (A3), the derivatives are

$$\frac{\partial_\alpha P(l_m = T,\alpha)}{P(l_m = T,\alpha)} = \frac{T}{\alpha} \tag{A5}$$

$$\frac{\partial_\alpha P(l_m = t < T,\alpha)}{P(l_m = t < T,\alpha)} = \frac{t}{\alpha} - \frac{1}{1-\alpha}. \tag{A6}$$

For a maximum of the log-likelihood for the observed values l_m, the sum in (A4) is required to be zero. Inserting $M - M_T$ times the term (A5) for all observations $l_m = T$ and M_T terms (A6), one for each observation $l_m = t < T$, we obtain

$$(M - M_T)\frac{T}{\alpha} + \sum_{l_m<T}\frac{l_m}{\alpha} - M_T\frac{1}{1-\alpha} = 0. \tag{A7}$$

With

$$\langle l_m\rangle = \frac{1}{M}\sum_{m=1}^{M} l_m = \frac{1}{M}\left((M - M_T)T + \sum_{l_m<T} l_m\right) \tag{A8}$$

we can divide (A7) by the number M of observations and re-order the equation to obtain

$$\frac{\langle l_m\rangle M}{M_T} = \frac{\alpha}{1-\alpha}. \tag{A9}$$

However, this is exactly the expected value $\mathrm{E}[t]$ of time steps for the full geometric distribution (A1).

References

1. Lehnertz, K.; Bialonski, S.; Horstmann, M.T.; Krug, D.; Rothkegel, A.; Staniek, M.; Wagner, T. Synchronization phenomena in human epileptic brain networks. *J. Neurosci. Methods* **2009**, *183*, 42–48. [CrossRef] [PubMed]
2. Schnitzler, A.; Gross, J. Normal and pathological oscillatory communication in the brain. *Nat. Rev. Neurosci.* **2005**, *6*, 285–296. [CrossRef] [PubMed]
3. Pikovsky, A.; Rosenblum, M.; Kurths, J. Synchronization, A universal concept in nonlinear sciences. *Self* **2001**, *2*, 3. [CrossRef]
4. Stankovski, T.; Pereira, T.; McClintock, P.V.E.; Stefanovska, A. Coupling functions: Universal insights into dynamical interaction mechanisms. *Rev. Mod. Phys.* **2017**, *89*, 045001. [CrossRef]
5. Kuramoto, Y. *Chemical Oscillations, Waves and Turbulence*; Springer: Berlin/Heidelberg, Germany, 1984; Volume 19.
6. Bick, C.; Goodfellow, M.; Laing, C.R.; Martens, E.A. Understanding the dynamics of biological and neural oscillator networks through exact mean-field reductions: A review. *J. Math. Neurosci.* **2020**, *10*, 9. [CrossRef] [PubMed]
7. Eldering, J.; Lamb, J.S.; Pereira, T.; dos Santos, E.R. Chimera states through invariant manifold theory. *Nonlinearity* **2021**, *34*, 5344. [CrossRef]
8. Tönjes, R.; Masuda, N.; Kori, H. Synchronization transition of identical phase oscillators in a directed small-world network. *Chaos Interdiscip. J. Nonlinear Sci.* **2010**, *20*, 033108. [CrossRef]
9. Komarov, M.; Pikovsky, A. Finite-size-induced transitions to synchrony in oscillator ensembles with nonlinear global coupling. *Phys. Rev. E* **2015**, *92*, 020901. [CrossRef]
10. Ottino-Löffler, B.; Strogatz, S.H. Volcano Transition in a Solvable Model of Frustrated Oscillators. *Phys. Rev. Lett.* **2018**, *120*, 264102. [CrossRef]
11. Tanzi, M.; Pereira, T.; van Strien, S. Robustness of ergodic properties of non-autonomous piecewise expanding maps. *Ergod. Theory Dyn. Syst.* **2019**, *39*, 1121–1152. [CrossRef]
12. Gong, C.C.; Toenjes, R.; Pikovsky, A. Coupled Möbius maps as a tool to model Kuramoto phase synchronization. *Phys. Rev. E* **2020**, *102*, 022206. [CrossRef] [PubMed]

13. Marvel, S.A.; Mirollo, R.E.; Strogatz, S.H. Identical phase oscillators with global sinusoidal coupling evolve by Möbius group action. *Chaos* **2009**, *19*, 043104. [CrossRef] [PubMed]
14. Montbrió, E.; Pazó, D.; Roxin, A. Macroscopic Description for Networks of Spiking Neurons. *Phys. Rev. X* **2015**, *5*, 021028. [CrossRef]
15. Pikovsky, A.S. Synchronization of oscillators with hyperbolic chaotic phases. *Appl. Nonlinear Dyn.* **2021**, *29*, 78–87.
16. Ott, E.; Antonsen, T.M. Low dimensional behavior of large systems of globally coupled oscillators. *Chaos Interdiscip. J. Nonlinear Sci.* **2008**, *18*, 037113. [CrossRef]
17. Ott, E.; Antonsen, T.M. Long time evolution of phase oscillator systems. *Chaos Interdiscip. J. Nonlinear Sci.* **2009**, *19*, 023117. [CrossRef]
18. Kuramoto, Y. Self-entrainment of a population of coupled non-linear oscillators. In Proceedings of the International Symposium on Mathematical Problems in Theoretical Physics, Kyoto, Japan, 23–29 January 1975; Springer: Berlin/Heidelberg, Germany, 1975; pp. 420–422.
19. Peter, F.; Pikovsky, A. Transition to collective oscillations in finite Kuramoto ensembles. *Phys. Rev. E* **2018**, *97*, 032310. [CrossRef]
20. Peter, F.; Gong, C.C.; Pikovsky, A. Microscopic correlations in the finite-size Kuramoto model of coupled oscillators. *Phys. Rev. E* **2019**, *100*, 032210. [CrossRef]
21. Skardal, P.S.; Restrepo, J.G. Hierarchical synchrony of phase oscillators in modular networks. *Phys. Rev. E* **2012**, *85*, 016208. [CrossRef]
22. Martens, E.A. Chimeras in a network of three oscillator populations with varying network topology. *Chaos Interdiscip. J. Nonlinear Sci.* **2010**, *20*, 043122. [CrossRef]
23. Martens, E.A.; Panaggio, M.J.; Abrams, D.M. Basins of attraction for chimera states. *New J. Phys.* **2016**, *18*, 022002. [CrossRef]
24. Tönjes, R.; Fiore, C.E.; Pereira, T. Coherence resonance in influencer networks. *Nat. Commun.* **2021**, *12*, 72. [CrossRef] [PubMed]
25. Laing, C.R. Chimera states in heterogeneous networks. *Chaos Interdiscip. J. Nonlinear Sci.* **2009**, *19*, 013113. [CrossRef] [PubMed]
26. Tönjes, R.; Pikovsky, A. Low-dimensional description for ensembles of identical phase oscillators subject to Cauchy noise. *Phys. Rev. E* **2020**, *102*, 052315. [CrossRef] [PubMed]
27. Clusella, P.; Montbrió, E. Regular and sparse neuronal synchronization are described by identical mean field dynamics. *arXiv* **2022**, arXiv:2208.05515.
28. de Oliveira, M.; da Luz, M.; Fiore, C. Generic finite size scaling for discontinuous nonequilibrium phase transitions into absorbing states. *Phys. Rev. E* **2015**, *92*, 062126. [CrossRef]
29. Luccioli, S.; Olmi, S.; Politi, A.; Torcini, A. Collective dynamics in sparse networks. *Phys. Rev. Lett.* **2012**, *109*, 138103. [CrossRef]
30. Restrepo, J.G.; Ott, E.; Hunt, B.R. Onset of synchronization in large networks of coupled oscillators. *Phys. Rev. E* **2005**, *71*, 036151. [CrossRef]
31. Baer, S.M.; Erneux, T.; Rinzel, J. The slow passage through a Hopf bifurcation: Delay, memory effects, and resonance. *SIAM J. Appl. Math.* **1989**, *49*, 55–71. [CrossRef]
32. Ichinomiya, T. Frequency synchronization in a random oscillator network. *Phys. Rev. E* **2004**, *70*, 026116. [CrossRef]
33. Ko, T.W.; Ermentrout, G.B. Partially locked states in coupled oscillators due to inhomogeneous coupling. *Phys. Rev. E* **2008**, *78*, 016203. [CrossRef] [PubMed]
34. Khasminskii, R. *Stochastic Stability of Differential Equations*; Springer Science & Business Media: Berlin/Heidelberg, Germany, 2011; Volume 66.


ICMC
USP
SÃO CARLOS